

# COULOMB EXCITATION OF $^{140}\text{Sm}$

by

Trond Wiggo Johansen

THESIS

for the degree of

MASTER OF SCIENCE



Faculty of Mathematics and Natural Sciences  
University of Oslo

September 2019



# **Abstract**



To my family, for all their support and encouragement!



# Acknowledgements

Supervisors Professor Andreas Görgen and Dr. Katarzyna Hadyńska-Klęk  
Nuclear Physics Group  
Computational Physics Group, Professor Morten Hjorth-Jensen  
CERN-ISOLDE, Dr. Liam Gaffney  
Ville Virtanen from University of Jyväskylä for tips on scripts.  
Lillefy, FFU, Fysikkforeningen  
My family  
Morten, Alex and Astrid.  
Ina, for pushing me towards excellence, I love you.

## Collaboration details

ENSAR2: European Nuclear Science and Applications Research - 2 <http://www.ensarfp7.eu>, UiO, ISOLDE, other contributors to the experiment?

*Trond Wiggo Johansen*

September, 2019





# Contents

<b>1</b>	<b>Introduction</b>	<b>11</b>
<b>2</b>	<b>Theory</b>	<b>13</b>
2.1	Coulomb excitation . . . . .	15
2.2	Oppgaveteksten (skal fjernes!) . . . . .	19
<b>3</b>	<b>Coulomb excitation experiment</b>	<b>23</b>
3.1	ISOLDE at CERN . . . . .	23
3.2	Experimental setup . . . . .	25
3.2.1	Beam production . . . . .	25
3.2.2	Sources of beam contaminants . . . . .	27
3.2.3	The secondary target . . . . .	27
3.2.4	Miniball spectrometer . . . . .	28
3.3	The data acquisition system . . . . .	31
3.4	The time structure . . . . .	33
<b>4</b>	<b>Data analysis</b>	<b>37</b>
4.1	Data handling . . . . .	37
4.1.1	Counting and naming convention . . . . .	39
4.2	Data conversion . . . . .	39
4.3	Detector calibration . . . . .	40
4.3.1	Simulation . . . . .	42
4.3.2	Online calibration of the particle detector . . . . .	43
4.3.3	User calibration of the particle detector . . . . .	45
4.3.4	Threshold . . . . .	49
4.3.5	Time calibration . . . . .	50
4.3.6	Calibration of the $\gamma$ detectors . . . . .	51
4.3.7	Doppler correction . . . . .	56
4.3.8	Broken detector segments . . . . .	57
<b>5</b>	<b>Experimental results and discussion</b>	<b>73</b>
<b>6</b>	<b>Summary and outlook</b>	<b>77</b>
<b>Appendices</b>		<b>79</b>
<b>Appendix A</b>	<b>Acronyms and abbreviations</b>	<b>81</b>
<b>Appendix B</b>	<b>Symbol list</b>	<b>83</b>
<b>Appendix C</b>	<b>Two-particle collision</b>	<b>85</b>

C.1	Laboratory (LAB) frame of reference . . . . .	85
C.2	Center of mass (CM) frame of reference . . . . .	88
C.3	Connection between the LAB frame and the CM frame . . . . .	90
<b>Appendix D</b>	<b>Computer setup and environment</b>	<b>95</b>
D.1	The computer . . . . .	95
D.2	The environment . . . . .	96
D.2.1	Relative path of programs and scripts . . . . .	96
D.3	Run time . . . . .	96
D.4	Script usage? . . . . .	96
D.5	Connecting MiniballCoulexSort with ROOT . . . . .	97
D.6	Running ROOT and MiniballCoulexSort from anywhere in the terminal . . . . .	98
<b>Appendix E</b>	<b>CD simulation</b>	<b>101</b>
<b>Bibliography</b>		<b>105</b>

# Chapter 1

## Introduction

*"If you are not confused by quantum physics then you haven't really understood it."*

– Niels Bohr

### + Motivation

$^{140}\text{Sm}$  ( $T_{1/2} = 14.82$  min)

experiment code: IS558, which was titled Shape Transition and Coexistence in Neutron-Deficient Rare Earth Isotopes

The experiment has been done before, with lower energy (and another target), Malin Klintefjord. <http://urn.nb.no/URN:NBN:no-56121>

Malin Klintefjord PhD thesis [1] with the three papers [2], [3] and [4] on  $^{140}\text{Sm}$ .

Experiment conducted 8th - 14th of August 2017.

Expect to measure transition probabilities  $B(E2)$  and quadrupole moment (nuclear deformation).

### Tilbakemelding:

old REX-ISOLDE post-accelerator limited to 2.8 MeV/u (low Coulomb excitation cross section, low probability for multi-step excitation). Mo target was chosen to maximize cross section at this energy, and to normalize  $B(E2; 0^+ \rightarrow 2^+)$  value in  $^{140}\text{Sm}$  to the well-known  $B(E2)$  value for the target.

New HIE-ISOLDE: energies up to 10 MeV/u  $\implies$  we can choose high-Z target (Pb)  $\implies$  high Coulex cross section, especially for multi-step. Also:  $B(E2)$  for  $^{140}\text{Sm}$  now known from previous experiment (and a lifetime measurement)  $\implies$  no need for normalization: we can use the known  $B(E2; 0^+ \rightarrow 2^+)$  to normalize

the transition probabilities for the higher-lying transitions. Chosen 4.7 MeV/u as the highest possible energy that is safe for Pb (distance of closest approach large enough to exclude nuclear interaction.)

All of my scripts are available in my GitHub repository found at  
<https://github.com/wiggoen/MasterThesis>.

**COULEX links:**

- [https://www.researchgate.net/profile/Jacek\\_Wojciechowski/publication/268366137\\_Application\\_of\\_Genetic\\_Algorithm\\_with\\_Real\\_Representation\\_to\\_COULEX\\_Data\\_Analysis/links/54b913850cf269d8cbf72ed4.pdf](https://www.researchgate.net/profile/Jacek_Wojciechowski/publication/268366137_Application_of_Genetic_Algorithm_with_Real_Representation_to_COULEX_Data_Analysis/links/54b913850cf269d8cbf72ed4.pdf)
- <https://core.ac.uk/download/pdf/76649116.pdf>
- <http://oregonstate.edu/instruct/ch374/ch418518/Chapter%2010%20NUCLEAR%20REACTIONS.pdf>

# Chapter 2

## Theory

*"I think I can safely say that nobody understands quantum mechanics."*

– Richard Feynman

Tilbakemelding:

shape coexistence often found near closed shells. Example: neutron deficient Hg nuclei ( $Z = 80$  just below 82 shell closure,  $N \sim 104$ : neutron mid-shell).

$^{140}\text{Sm}$ :  $N = 78$ , just below  $N = 82$  shell closure,  $Z = 62$ : mid-shell.

Typical indication for shape coexistence:  $0^+$  states (often at low energy).

$^{140}\text{Sm}$  was thought to have a low-lying  $0^+$  state [Firestone], but this state was shown to be  $2^+$  [Suoranczyk?]. Indication for  $0^+$  states around 1.5 MeV.

One of the objectives of this experiment: clarify the nature/structure of these  $0^+$  states.

Shape transition: Sm-144 ( $Z = 62$ ,  $N = 82$ ) spherical. Adding neutrons: transition of  $N = 90$  from spherical to prolate deformed → shape-phase transition, so called X(5) critical-point symmetry.

Taking out neutrons: very neutron-deficient Sm nuclei are also prolate deformed (e.g. Sm-132), but for  $^{140}\text{Sm}$ : indication for triaxiality/ $\gamma$ -softness [Klintefjord] → another form of shape-phase transition/critical point behavior  $\implies$  E(5) [Iachello?].  $^{140}\text{Sm}$  could be one of the best examples for E(5) symmetry  $\implies$  need transition probabilities from higher-lying states to confirm.

Some suggestions:

- general things about nuclei shapes
- multipole expansion, shape parameters (5 parameters, 3 for space, 2 for deformation  $\beta$ ,  $\gamma$ ), ...
- quadrupole moments: intrinsic (body-fixed frame), spectroscopic (lab frame)
- transition probabilities, el.magn. matrix elements
- rotations and vibrations → energy spectra,  $B(E2)$  values

- Casten triangle (spherical vibrator, deformed rotor,  $\gamma$ -soft + X(5), E(5)), expected spectrum for E(5) nuclei
- the basics of Coulomb excitation (COULEX)
  - Quadrupole deformation of nuclei.

Shape coexistence possible for certain regions of  $N$  and  $Z$ .

- triaxial shape / shape coexistence
- benchmark for theoretical models
- transition probabilities and quadrupole moments between several excited states are not known
- fundamental research

COULEX:

- nucleus excited by electromagnetic interaction.
- de-excitation  $\rightarrow$  gamma

Why CoulEx? [https://iks32.fys.kuleuven.be/wiki/brix/images/5/58/10\\_20151123\\_Illana\\_BriX15\\_web.pdf](https://iks32.fys.kuleuven.be/wiki/brix/images/5/58/10_20151123_Illana_BriX15_web.pdf)

## Magic numbers

The magic numbers in the nuclear shell model is

$$2, 8, 20, 28, 50, 82, 126 \quad (2.1)$$

Maria Goeppert Mayer "discovered" them around 1945. She gave W. M. Elsasser credits for being the first to remark that such numbers exists. [cite: The Shell Model, M. G. Mayer]

Magic numbers: 2, 8, 20, 28, 50, 82, 126

Maria Goeppert Mayer "discovered" them in  $\sim$ 1945. Observation of periodicity in binding energy  $\implies$  shell model for nuclei.

Eugene Wigner believed in liquid-drop model, did not trust new theory  $\implies$  called these numbers "magic".

Source: [https://ocw.mit.edu/courses/nuclear-engineering/22-02-introduction-to-applied-nuclear-lecture-notes/MIT22\\_02S12\\_lec01.pdf](https://ocw.mit.edu/courses/nuclear-engineering/22-02-introduction-to-applied-nuclear-lecture-notes/MIT22_02S12_lec01.pdf)

### Intro?

Nuclear physics is the study of atomic nuclei.

In the atomic shell model, the shells are filled with electrons in order of increasing energy. This model can explain the complicated details of atomic

structure. In nuclear physics, a similar approach was used to explain the nuclear structure. [5]

The Pauli exclusion principle declares that "two identical fermions cannot occupy the same state". [6]

Isotope notation:

$$_Z^A X_N^Q$$

where  $X$  is the chemical symbol of the element,  $A$  is the nucleon number (mass number,  $A = Z + N$ ),  $Z$  is the atomic number (proton number),  $N$  is the neutron number and  $Q$  is the charge ( $Q = Z$  protons –  $i$  electrons).

## 2.1 Coulomb excitation

table of nuclides (HFB-style): [http://www-phynu.cea.fr/science\\_en\\_ligne/carte\\_potentiels\\_microscopiques/carte\\_potentiel\\_nucleaire\\_eng.htm](http://www-phynu.cea.fr/science_en_ligne/carte_potentiels_microscopiques/carte_potentiel_nucleaire_eng.htm)

$\beta - \gamma$  triangle: [http://www-phynu.cea.fr/science\\_en\\_ligne/carte\\_potentiels\\_microscopiques/noyaux/zz62/zz62nn78all\\_eng.html](http://www-phynu.cea.fr/science_en_ligne/carte_potentiels_microscopiques/noyaux/zz62/zz62nn78all_eng.html)

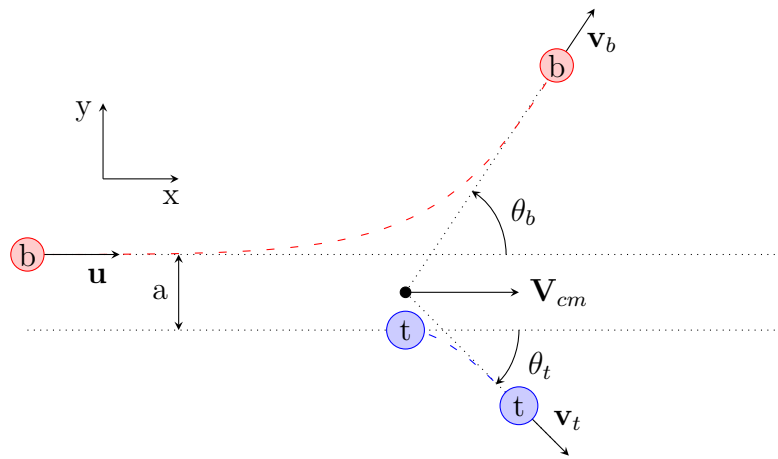
**Table 2.1:** Values of the fundamental physical constants from the National Institute of Standards and Technology (NIST) Physics Laboratory [7].

Quantity	Symbol	Numerical value	Unit
Speed of light in vacuum	$c$	299792458	m/s
Elementary charge	$e$	$1.602176634 \cdot 10^{-19}$	C
Electron volt	eV	$1.602176634 \cdot 10^{-19}$	J
Atomic mass unit	$u$	$1.66053906660(50) \cdot 10^{-27}$	kg

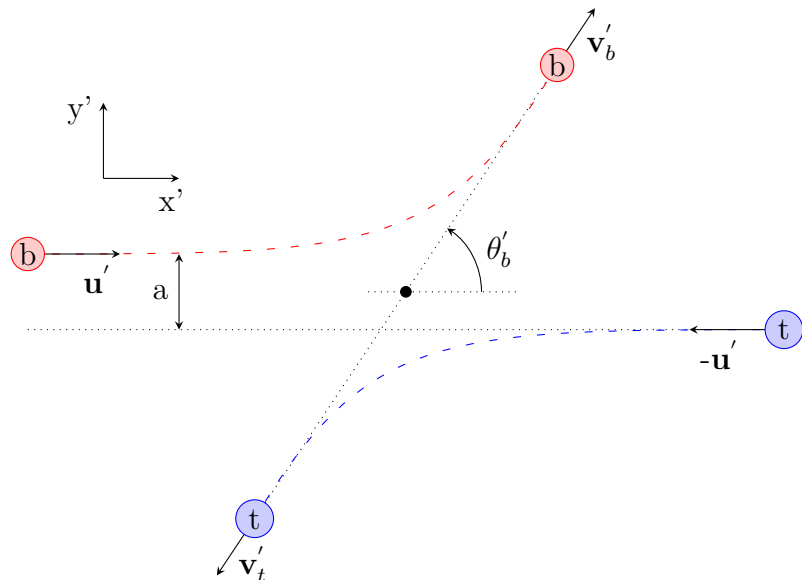
LISE++ [8]

**Table 2.2:** LAB vs. CM. Based on LAB input angles from  $\theta_b$  and  $\theta_t$ . From LISE++ kinematics calculator (reaction from the middle of the target).

(a) $\theta_b \in [22.0^\circ, 56.7^\circ]$ .			(b) $\theta_t \in [22.0^\circ, 56.7^\circ]$ .		
LAB		CM	LAB		CM
$\theta_b$ [°]	$\theta_t$ [°]	$\theta'_b$ [°]	$\theta_b$ [°]	$\theta_t$ [°]	$\theta'_b$ [°]
22.0	71.7	36.6	40.6	56.7	66.6
26.0	68.4	43.2	42.3	55.3	69.4
29.1	65.9	48.2	44.2	53.9	72.2
32.2	63.4	53.3	46.1	52.4	75.2
35.2	60.9	58.1	48.3	50.7	78.6
37.9	58.8	62.4	50.6	49.0	82.0
40.4	56.8	66.3	53.1	47.1	85.8
42.8	54.9	70.1	56.0	45.0	90.0
45.0	53.2	73.5	59.1	42.8	94.4
47.1	51.6	76.7	62.5	40.4	99.2
49.0	50.2	79.6	66.1	37.9	104.2
50.7	48.9	82.1	70.2	35.2	109.6
52.4	47.6	84.7	75.0	32.2	115.6
53.9	46.5	86.9	80.2	29.1	121.8
55.3	45.5	88.9	85.8	26.0	128.0
56.7	44.5	91.0	93.8	22.0	136.0



**(a)** Scattering in the laboratory (LAB) frame. A small angle  $\theta_b$  means forward scattering of the beam, a larger distance between the beam particle and the target particle, a weaker electromagnetic (EM) field and less excitation probability. A large angle  $\theta_b$  means backward scattering of the beam, a closer distance between the beam particle and the target particle, a stronger EM field and a higher excitation probability.



**(b)** Center of mass (CM) frame.

**Figure 2.1:** LAB vs. CM frame.



# NOTES TO BE REMOVED!!

## 2.2 Oppgaveteksten (skal fjernes!)

---

### Oppgavens mål:

The ISOLDE facility at CERN has been upgraded to provide higher energies and intensities for radioactive ion beams. A new experiment to study  $^{140}\text{Sm}$  was performed in the summer of 2017. The goal of the experiment was to measure electromagnetic transition probabilities and electric quadrupole moments for several excited states in  $^{140}\text{Sm}$  by measuring Coulomb excitation probabilities. A large data set was obtained using silicon detectors to determine the energies and angles of scattered particles, and germanium detectors to measure gamma rays from excited states in  $^{140}\text{Sm}$ .

The goal of the master thesis is to analyze the data from this experiment. The required tasks include development and improvement of data analysis software to determine Coulomb excitation yields. These yields will then, in a second step, be compared to theoretical calculations and transition probabilities and quadrupole moments will be extracted using chi-square minimization procedures.

### Prosjektbeskrivelse (omfang 60 studiepoeng):

The shape of an atomic nucleus is determined by a delicate interplay between macroscopic (liquid drop) properties and microscopic shell effects. Nuclei with filled proton or neutron shells (i.e. magic nuclei) are generally spherical in shape, whereas nuclei with open shells gain energy by assuming a deformed shape. Depending on the occupation of specific orbitals, the nuclear shape can change drastically by adding or removing protons or neutrons. Certain nuclei exhibit shape coexistence, i.e. the coexistence of quantum states that correspond to different shapes. Because the shape of a nucleus is so sensitive to the underlying nuclear structure and to changes of the proton and neutron numbers, the excitation energy, or the angular momentum, observables related to the nuclear shape are used as benchmarks for theoretical models.

Nuclei in the rare earth region, and in particular the chain of samarium isotopes, exhibit a variety of shape effects. The Sm isotope with closed neutron

shell at N=82,  $^{144}\text{Sm}$ , is spherical in shape. Adding neutrons to  $^{144}\text{Sm}$  changes the deformation to an elongated (prolate) quadrupole shape. The transition from spherical to prolate shape, which occurs for  $^{152}\text{Sm}$  at N=90, can be interpreted as a shape-phase transition. Flattened (oblate) quadrupole shapes are predicted by theory to occur below the N=82 shell closure. An earlier experiment studying  $^{140}\text{Sm}$  at CERN-ISOLDE found triaxial shape for this isotope, i.e. a shape where all three principal axes of the ellipsoid have different lengths.  $^{140}\text{Sm}$  can therefore be considered to lie at the critical point of a phase transition from spherical to deformed, and from prolate to oblate shape.

**Foreløpig tittel:**  
Coulomb excitation of  $^{140}\text{Sm}$

**Metoder som tenkes benyttet:**  
Multi-step Coulomb excitation with radioactive beam, isotope separation on-line technique, nuclear spectroscopy, particle-gamma and particle gamma-gamma coincidence analysis, advanced chi-square minimization procedures.

---

## Sjekk sensorveiledning!!

## Fjern blå linker in-text før innlevering!!

## Experimental setup - other info sources

- ISOL & Post acceleration: [https://www.euroschoolonexoticbeams.be/site/files/nlp/LNP700\\_contrib2.pdf](https://www.euroschoolonexoticbeams.be/site/files/nlp/LNP700_contrib2.pdf)
- ISOL RIB (2004): <http://accelconf.web.cern.ch/AccelConf/e04/PAPERS/TUXCH01.PDF>
- RIB (2017): <http://iopscience.iop.org/article/10.1088/1361-6471/aa990f/pdf>
- RIB: [http://publications.lib.chalmers.se/records/fulltext/175494/local\\_175494.pdf](http://publications.lib.chalmers.se/records/fulltext/175494/local_175494.pdf)
- RIB: <https://www.sciencedirect.com/science/article/pii/S0168583X02018864>
- Post-accelerated beams ISOLDE: <http://iopscience.iop.org/article/10.1088/1361-6471/aa78ca>

- PSB: <https://www.sciencedirect.com/science/article/pii/0168583X92959079>
- PSB: <https://home.cern/science/accelerators/proton-synchrotron-booster>
- RILIS ISOLDE: <https://www.sciencedirect.com/science/article/pii/S0168583X13008914>
- HIE-ISOLDE publications: <http://hie-isolde-project.web.cern.ch/hie-isolde-publications>
- Miniball pictures: <https://cds.cern.ch/record/844871?ln=en>
- The MINIBALL array [9]

DAQ:

- MAR<sub>a</sub>BQU web page: <https://www-old.mll-muenchen.de/marabou/htmldoc/>
- MAR<sub>a</sub>BQU file formatting: <https://www-old.mll-muenchen.de/marabou/htmldoc/marabou/IOSpec.html>



# Chapter 3

## Coulomb excitation experiment

*"If I could remember the names of all those particles, I'd be a botanist."*

– Enrico Fermi

### 3.1 ISOLDE at CERN

ISOLDE is a Radioactive Ion Beam (RIB) facility at CERN in Meyrin, Switzerland. Figure 3.1 shows the CERN accelerator complex, where ISOLDE is located beside the Proton Synchrotron Booster (PSB), in the lower right marked by a green box. The acronym ISOLDE stands for Isotope Separator On Line DEvice. The facility can produce over 1000 different radionuclides to be used in a wide variety of experiments in nuclear physics, atomic physics, solid state physics, life sciences and fundamental interactions. Experiments have been performed at ISOLDE since 1967 and since 2001 experiments with post-accelerated RIBs have been conducted. The High Intensity and Energy upgrade (HIE-ISOLDE) have made it possible to deliver energies up to 10 MeV/u in 2018 [10–12].

In general, it is very challenging to study radioactive, short lived nuclei. The newest edition of the Karlsruhe Nuclide Chart have nuclear data of over 4000 nuclides, and most of these are radioactive [13]. In many cases it is not possible to make radioactive nuclei targets and perform an experiment because of the short half-life of the nucleus of interest. To study these radioactive nuclei, RIBs are used on stable targets. One way of obtaining a RIB is to use the Isotope Separator On Line (ISOL) method. The three main reactions of producing radioactive atoms with the ISOL method are spallation, fragmentation and fission. Nuclear spallation is the process in which light fragments of the target are ejected due to the high-energy impact of the incoming beam. Fragmentation is the splitting of a compound into smaller particles or unstable ions. In fission an atomic nucleus is split into two or more nuclei. In the ISOL method, two accelerator systems

are needed. The first accelerator is used to produce the radioactive atoms in a primary target, and the second accelerator is used to accelerate these atoms into a secondary target [11, 14, 15]. In RIB facilities the intensity is generally a bit lower compared to stable beam facilities, which is a big challenge. ISOL facilities operate around the Coulomb barrier in terms of energy, making them suitable for Coulomb excitation and particle transfer reactions.

The beam at the RIB facilities consists of, as the name implies, radioactive isotopes. In contrast to conventional facilities where the target is made out of the isotope of interest, the investigated isotope is the beam accelerated into a target. The velocity of the beam is significant with  $v/c$  values of a few percent. In the electromagnetic (EM) interaction with the target, the beam gets excited into a higher energy state. When the beam isotopes de-excite, they emit  $\gamma$ -rays which can be observed to have large Doppler shifts. A sizable Doppler broadening can be observed in the  $\gamma$ -rays due to the finite solid angle of the detectors. When the detection system has high granularity, the Doppler shifts and broadening can be corrected for. If the angle between the recoiling nucleus and the  $\gamma$ -ray can be determined accurately, Doppler correction can be applied [16].

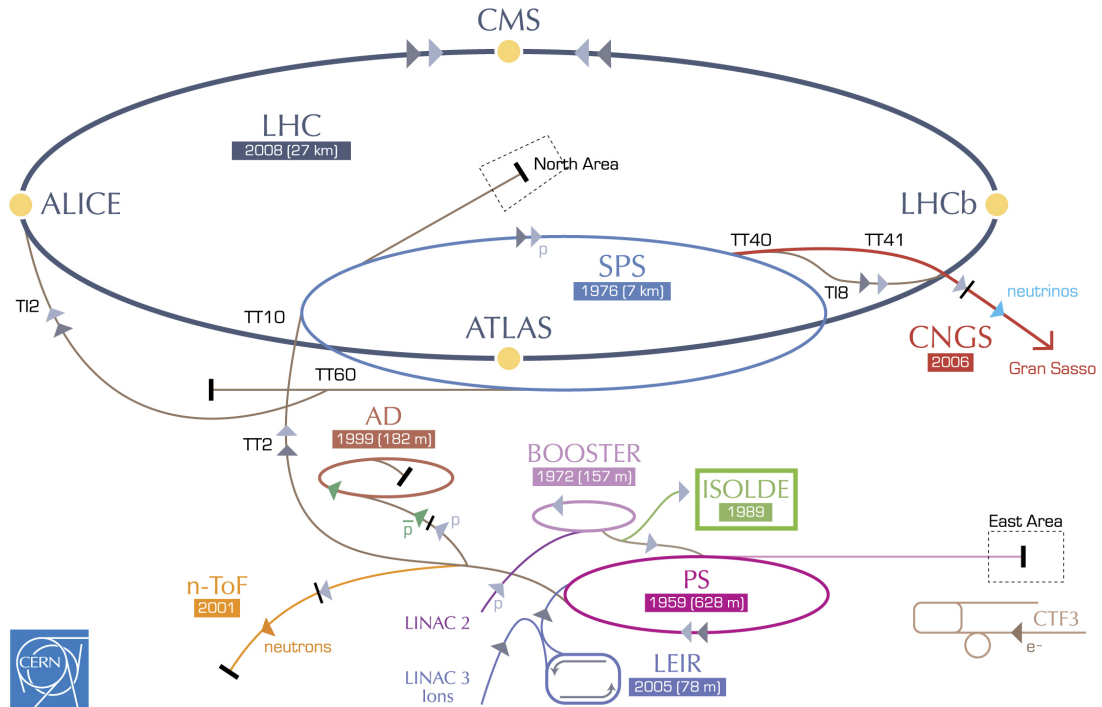


**Figure 3.1:** The CERN accelerator complex, adapted from [17]. ISOLDE, marked with a green box, receives accelerated protons from LINAC 2 and the PS Booster.

## 3.2 Experimental setup

### 3.2.1 Beam production

[Figure 3.2](#) shows a sketch of the experimental setup of the  $^{140}\text{Sm}$  Coulomb excitation experiment. Accelerated proton beam bunches from the PSB comes into the ISOLDE facility and collide with a thick production target, the primary target. Two proton beam bunches are separated by 1.2 s. The proton beam has an energy of 1.4 GeV and an intensity up to  $2 \mu\text{A}$  [18, 19]. ISOLDE typically takes 50% [16] of all proton bunches form the PSB, the rest goes to the Large Hadron Collider (LHC) and the other experiments shown in [Figure 3.1](#). The target material is chosen depending on the RIB of interest. If the requested RIB is neutron-rich, then fission is the production process and a primary target of uranium ( $^{238}\text{U}$ ) is chosen. In this experiment, a neutron-deficient RIB was requested, and a primary target of tantalum (Ta,  $Z = 73$ ) was chosen. The production target is selected from a region in the chart of nuclides containing stable nuclei that are heavier than the nucleus of interest. When the proton beam collides with the primary target, the target is smashed into pieces and radioactive nuclides in the chart of nuclides up to Ta are produced. In this way, a large range of isotopes are produced. The remaining challenge is to extract the isotope of interest in order to create a RIB. Before the isotope of interest can be obtained, a method of selecting the chemical element of interest has to be used.

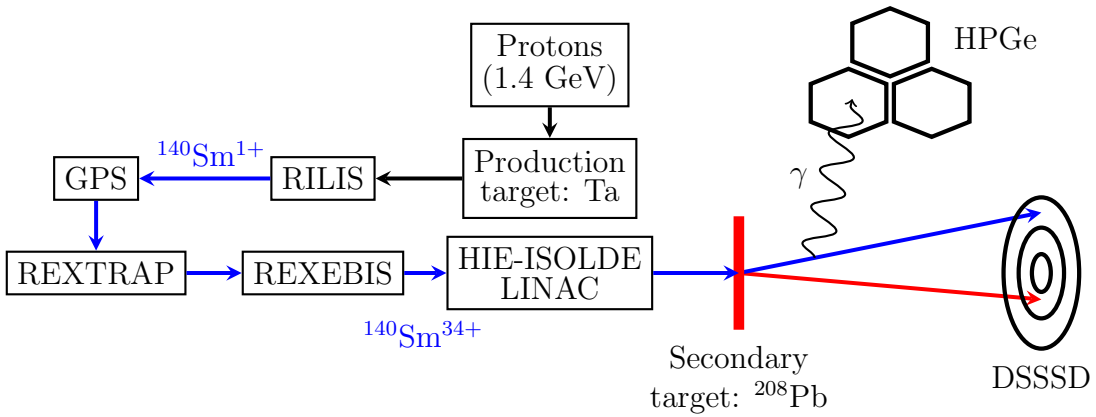


**Figure 3.2:** The Coulomb excitation setup at ISOLDE. Adapted from [1]. See text for information.

To get the atomic element of interest, one approach is to use a method of selective ionization and then a high voltage electrostatic field to extract the ions. Electronic transitions are characteristic for each chemical element. A laser with precisely tuned wavelength can obtain the photon energy that matches the electronic transition energies in the atom [20, 21]. Thus we can use one laser to

excite an electron to a specific excited electron-state in the atom, a second laser to excite electrons further to another excited electron-state and a third laser to remove the electron. In this way we only ionize the atomic element of interest.

A common challenge is contaminants from surface ionization, that is atoms that collide with the walls of the ion source. This can be significant, even dominant in some cases, but in this experiment it was not a problem. Sm has the lowest ionization potential of the rare earth elements. In any case it needs to be monitored using laser on/off measurements. By periodically switching the laser on and off, the resulting contaminants in the beam can be detected.

The Resonance Ionization Laser Ion Source (RILIS) is based on the method of step-wise (2-3 step) excitation and ionization of the atom. It is an element-selective process which is used to produce ion beams of the desired element [22]. In this experiment RILIS was used to select samarium (Sm) with atomic number  $Z = 62$ . After RILIS has selected Sm, we have a continuous beam of Sm ions of 60 keV energy. The target is on a 60 kV high voltage platform [11, 18].

The next step in the process is to perform a mass separation, and then to give the continuous beam a time structure. The post-accelerator cannot accept an incoming continuous beam, it accelerates bunches. The beam may hit one of two target stations; either the General Purpose Separator (GPS) or the High Resolution Separator (HRS). The GPS has one bending magnet and can deliver beams of different masses simultaneously into three beam lines, while the HRS has two bending magnets with high mass resolving power which delivers the beam into the main beam line. Both separators feed the beam lines in the experimental hall. The two extra beam lines that the GPS can feed, can have an isotope mass difference of  $\pm 13\%$  compared to the main beam line isotope mass [18, 23]. Even though the HRS have a high mass resolving power,  $M/\Delta M > 5000$ , it is not sufficient resolving power to separate the isobars, which is why RILIS had to be used. In this experiment the GPS was used to select the isotope of Sm with mass number  $A = 140$ . The mass separator also excludes the contaminants that exits RILIS with a different mass than  $A = 140$ . In principle, isobaric contaminants from surface ionization can still be present in the beam. Luckily, the neighboring elements of Sm produces very little surface ionization.

Following the GPS, a continuous beam of  $^{140}\text{Sm}$  is obtained. In the Radioactive beam EXperiment TRAP (REXTRAP), the  $^{140}\text{Sm}$  ions are collected in order to release them in bunches that are matched to the time structure of the LINear ACcelerator (LINAC). REXTRAP is a penning trap which has the tasks of accumulation, bunching and cooling of the RIB [10, 24, 25]. The ions are released in bunches and transferred to the REX Electron Beam Ion Source (REXEgis).

REXEgis is a charge breeder where the RIB obtains a high charge state [26], with a mass-to-charge ( $A/q$ ) ratio typically between 2.5 and 4.5 [27]. In REXEgis more electrons in the RIB are removed through interaction with a high-intensity electron beam. The longer the ions stay in REXEgis, the higher

the charge state becomes. The EBIS blasts off more electrons from Sm, which leaves the nucleus in a high charge state, going from  $^{140}\text{Sm}^{+1}$  to  $^{140}\text{Sm}^{+34}$  with  $A/q \approx 4.1$ . To accelerate the charged ions, that is the beam, to high energy, the beam must consist of highly charged ions. Inside REXEBIS we get a distribution of charge states. The LINAC can only accept one charge state, so the parts of the RIB that have the wrong charge state is lost [28–31]. REXEBIS releases the beam with a certain energy through another mass separator and into the HIE-ISOLDE LINAC [10].

The HIE-ISOLDE LINAC accelerates the beam of  $^{140}\text{Sm}$  with excellent purity to 4.65 MeV/u (total energy 651 MeV) through the beam line. Magnets bend the beam into the Miniball spectrometer, where the beam hits a secondary target of  $^{208}\text{Pb}$ . In the EM interaction between the beam and the secondary target, the beam particles gets excited. A lot of  $^{140}\text{Sm}$  particles from the beam and  $^{208}\text{Pb}$  particles from the secondary target fly onwards to the particle detector. On their way to the particle detector, the beam particles de-excite and emits  $\gamma$ -rays which is detected by the  $\gamma$ -detectors. This experiment was one of the first Miniball experiments with the new upgraded superconducting accelerator, the HIE-ISOLDE LINAC.

### 3.2.2 Sources of beam contaminants

To have a successful experiment, the purity of the beam is of great importance. Contaminants in the beam can come from different sources [16]. From the primary target we can have:

- isobaric contaminants which are inseparable by the mass separator because of the same mass number
- isotopes with an integer multiple of both mass and charge

and from stable isotopes the contaminants can come from:

- buffer gas in REXTRAP (e.g. Ne, Ar)
- residual gas in REXEBIS (e.g. C, O)
- components of REXEBIS (e.g. La from the cathode)

### 3.2.3 The secondary target

For the current experiment, a target consisting of  $^{208}\text{Pb}$  with a thickness of 1.4 mg/cm<sup>2</sup> was chosen. It is quite difficult to excite  $^{208}_{82}\text{Pb}_{126}$  as it is a doubly magic nuclei, and it is therefore well suited for the experiment. In that way, transitions from the target will not complicate the spectrum. With a target consisting of

the highest possible  $Z$  of a stable isotope ( $Z = 82$ ), the excitation probability of  $^{140}\text{Sm}$  is maximized.

$^{208}\text{Pb}$  has no quadrupole deformation. The first excited state is of octupole vibration with an energy of 2615 keV, a half-life of  $T_{1/2} = 16.7$  ps and a spin and parity of  $J^\pi = 3^-$ . There is a probability of seeing a little bit of the first excited state in the spectrum. This happens if the EM interaction is almost head on, and the target hits one of the inner rings.

Another advantage of this experiment was that there was no need for  $\gamma$  normalization. From the previous experiment [4] and from lifetime measurements [32], the  $B(E2, 0_1^+ \rightarrow 2_1^+)$  value of  $^{140}\text{Sm}$  was ?extracted / obtained / calculated?.

Unfortunately there was a finger print on the target, so even before beginning the experiment, there was some contamination (probably carbon).

### 3.2.4 Miniball spectrometer

Figure 3.3 shows an overview picture of the Miniball spectrometer.

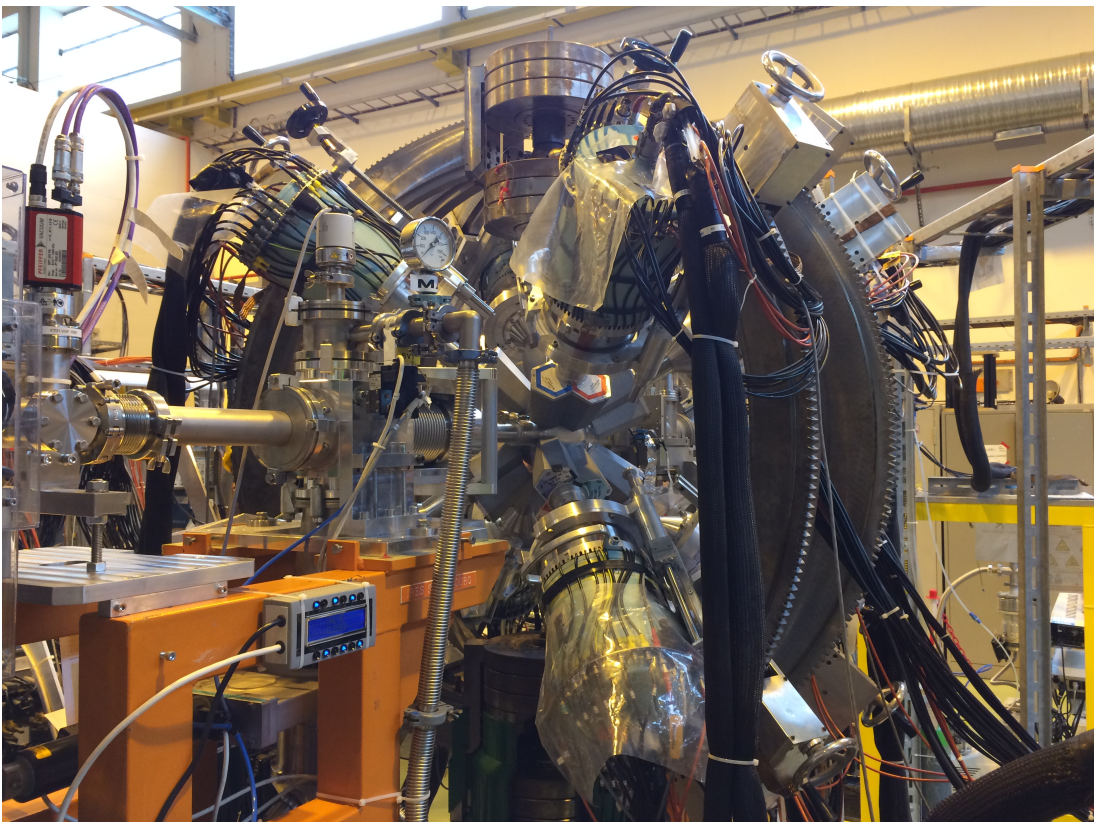


**Figure 3.3:** An overview picture of the Miniball spectrometer. The target chamber is in the middle of the picture, surrounded by the  $\gamma$ -detector array.  
Photo by: Trond Wiggo Johansen.

### Target chamber

The target chamber is a hollow sphere made out of a machined out, single piece of aluminium alloy ( $\text{AlMg}_3$ ), with a thin wall and an inner radius of approximately 80 mm. Inside the chamber we find a target wheel and a particle detector. The target wheel can hold up to six different targets as shown in [Figure 3.4](#). The particle detector can be positioned 25 - 31 mm from the target wheel, limited by the space inside the chamber. Outside of the target chamber the average distance from each  $\gamma$ -detector cluster to the center of the target chamber is approximately 10 cm. The forward detectors and the backward detectors has an angular position  $\theta$  of approximately  $45^\circ$  and  $135^\circ$  respectively, compared to the beam line. In the vertical plane, perpendicular to the beam line, the four  $\gamma$ -detectors in forward and backward position are placed roughly on a circle with a separation of  $\phi = 90^\circ$  [[16](#)].

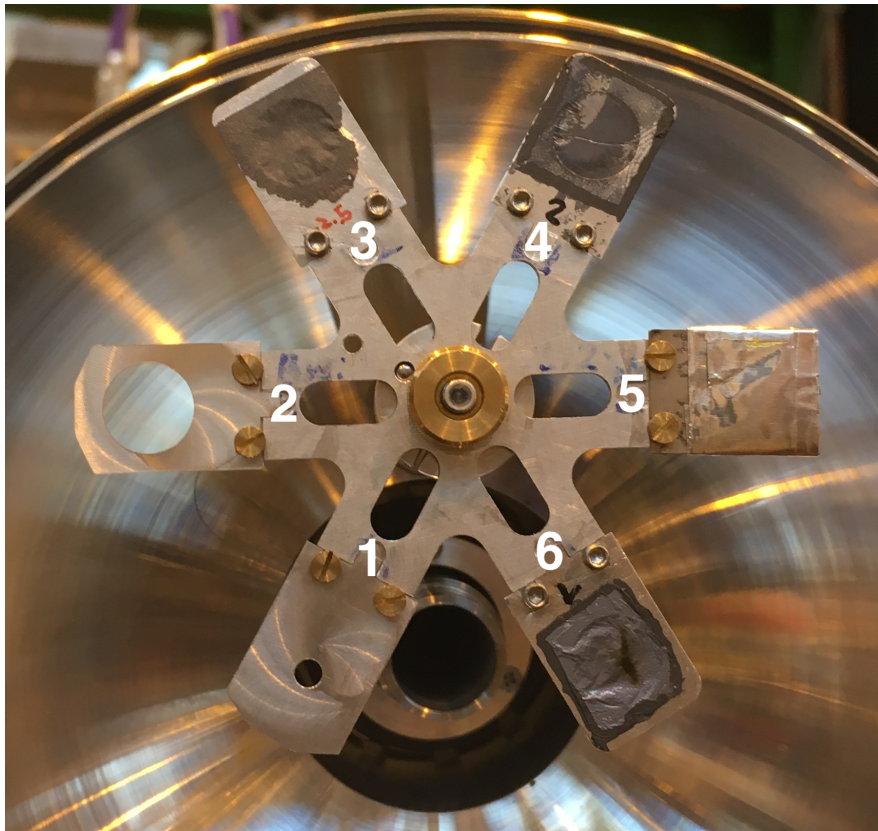


**Figure 3.4:** The target wheel can hold up to six different targets. Position 1 and 2 are holes with a diameter of 3 and 12 mm respectively. They are used for beam tuning. Position 3 and 4 has  $^{208}\text{Pb}$  targets with thickness 2.5 and 0.7 mg/cm $^2$  respectively. Position 5 had 13 layers of  $^{27}\text{Al}$  foil. Position 6 has the target  $^{208}\text{Pb}$  with thickness 1.4 mg/cm $^2$ , which was the secondary target used in the experiment. Photo by: Dr. Liam Gaffney, date: 07.08.2017.

### Particle detector, DSSSD (CD)

To detect the scattered beam and target nuclei, a segmented Double Sided Silicon Strip Detector (DSSSD) composed of four quadrants was used. [Figure 3.5](#) shows a sketch of the front and back side. The DSSSD looks very like an audio Compact Disc (CD), and hence it is called the CD. In the front of the CD, one quadrant consists of 16 annular strips (rings) with a pitch of 2 mm, while the back consists of 24 sector (radial) strips with a pitch of 3.5°. The innermost strip has an inner radius of the active area of 9 mm, while the outermost strip has an outer radius of the active area of 40.9 mm. The active area is the area in which a particle can be detected, the detectable surface. In total, there are 160 discrete detector elements for all four quadrants (64 in front, 96 in back). Each quadrant is connected to its own Analog to Digital Converter (ADC). As a result of too few available channels in the ADC, the sector strips in the back are paired up. In consequence, it is effectively 12 strips at the back side of the CD. The whole CD detector has a total area of 5000 mm<sup>2</sup>, where approximately 93% of the detector consists of a detectable surface. In Coulomb excitation experiments the silicon wafer thickness is usually 500 μm. The silicon wafer is the thin slice of semiconductor which can detect the incoming particles. For simplicity the dead layer thickness is usually assumed to be 0.7 μm [16, 33]. [Table 3.1](#) shows some of the specifications of the CD. The distance from the target to the CD was 27 ± 1 mm. In the laboratory (LAB) reference frame the CD has a angular coverage between 18.4° and 56.6°. An extensive description of the CD can be found in [34].

**Table 3.1:** CD specifications.

	Annular strips (CD Front)	Secular strips (CD Back)
Number of strips	16	24
Inner radius of active area	9.000 mm	-
Outer radius of active area	40.900 mm	-
Strip pitch	2.000 mm	3.5°
Strip width	1.900 mm	3.4°
Strip length	-	31.900 mm
Active angle coverage	81.6°	81.6°
Inner strip distance	-	0.100 mm

### The high-purity germanium (HPGe) $\gamma$ detectors

In Coulomb excitation experiments, the target chamber is surrounded by the  $\gamma$  detectors as displayed in [Figure 3.6](#). The  $\gamma$ -ray spectrometer consists of a total of 24 six-fold segmented High-Purity Germanium (HPGe) crystals, which are divided into 8 clusters of 3 crystals each. Each crystal is encapsulated and

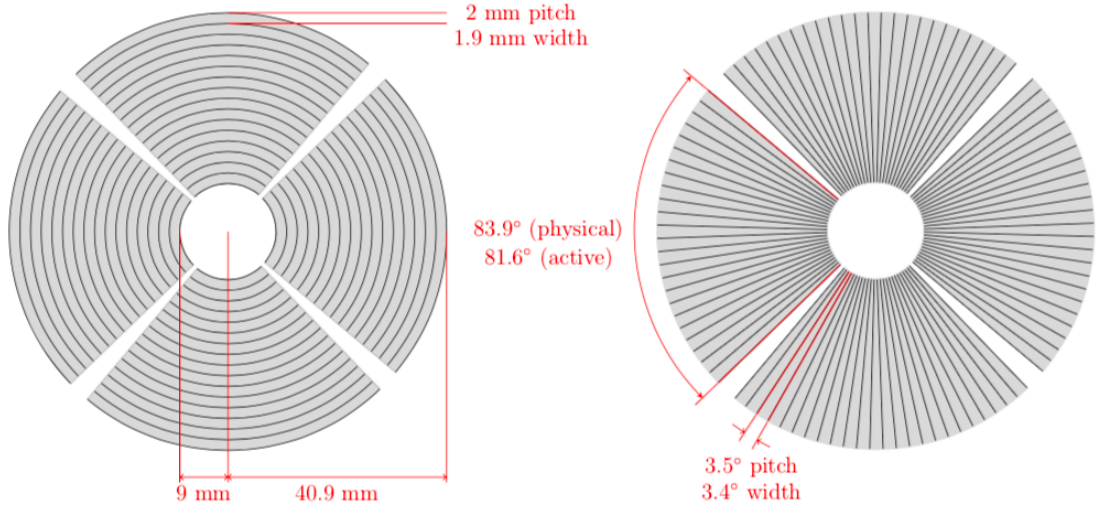


**Figure 3.5:** CD sketch, adapted from [33]. On the left is the front side of the CD. The numbering of the strips goes from strip 0 (outermost) to strip 15 (innermost). Quadrants are numbered in clockwise direction with respect to the beam direction, so that left is 1, up is 2, right is 3 and down is 4. On the right side is the back side of the CD. The numbering of the strips goes from strip 0 to strip 23 in counter-clockwise direction viewed from this side. Quadrants are numbered in clockwise direction with respect to the beam direction. From this perspective right is 1, up is 2, left is 3 and down is 4.

segmented into 6 parts, making a total of 144 segments. For maximum efficiency, the detectors are placed in a compact geometry around the target chamber [16, 35]. The detector-array can cover a solid angle of about 60% of  $4\pi$ , when the optimum distance between the target chamber and the HPGe-clusters is achieved. The average energy resolution at  $E_\gamma = 1.3$  MeV is 2.3 keV [36]. Figure 3.7 shows a sketch of one triple-cluster of the HPGe  $\gamma$ -detector array. From each detector we get seven signals in total for each event, one from the core and six from each segment. This requires 168 channels for data acquisition. The shapes of these signals are analyzed to provide information about the energy and time of the  $\gamma$ -ray, in addition to the detection position within the detector cluster. Compared to using the whole crystal, a better Doppler correction can be performed when the  $\gamma$ -detectors are segmented. During operation the HPGe-clusters needs to be cooled down by liquid nitrogen which is provided by the automated filling system [35].

### 3.3 The data acquisition system

Signals from the CD and the HPGe clusters are read out by the ADC and Digital Gamma Finder (DGF) modules and sent to a Personal Computer (PC) in the

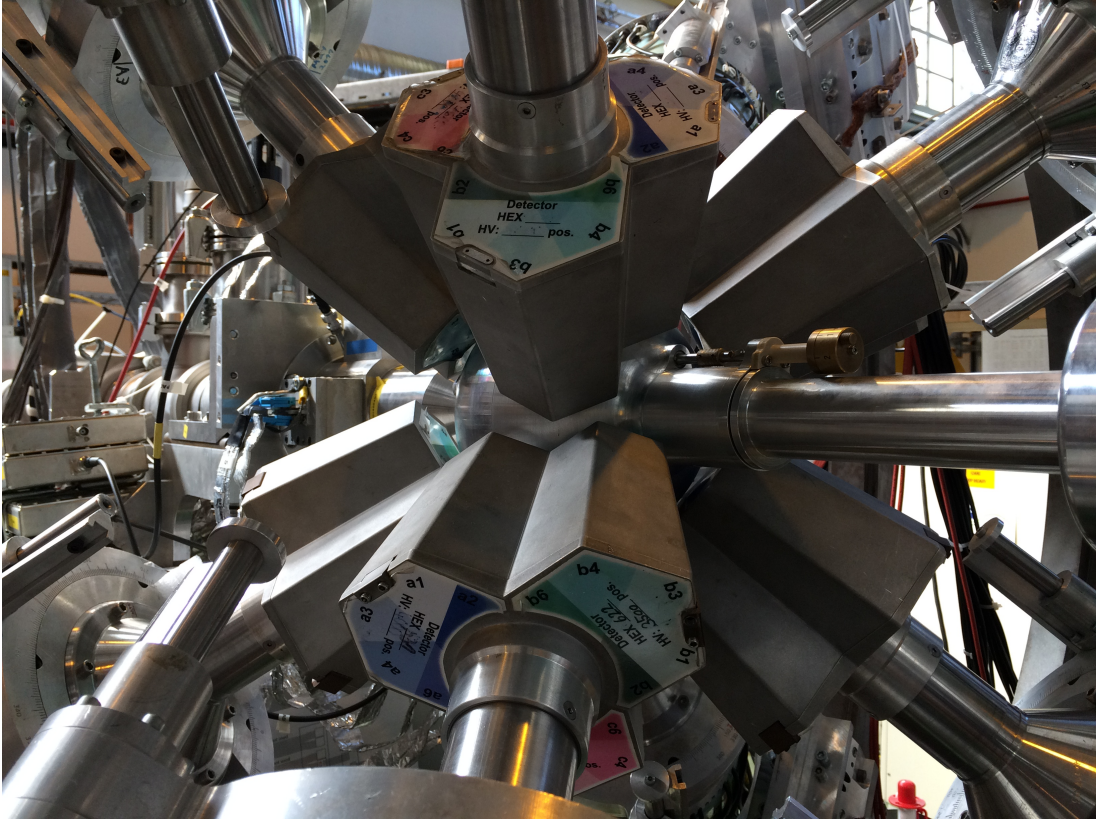


**Figure 3.6:** Close up picture of the Miniball spectrometer. The Miniball target chamber is in the middle, surrounded by the triple-cluster encapsulated  $\gamma$  crystals. The beam line goes through the target chamber.  
Photo by: Trond Wiggo Johansen.

Data AcQuisition (DAQ) room at ISOLDE. The data is then stored in a PC. The collection of data is done by the MAR<sub>a</sub>BQU [38] DAQ system [16]. It is split in two parts, as presented in Figure 3.8, one front-end part based on the Multi Branch System (MBS) [39] and one back-end part based on the ROOT framework [40]. The front-end takes care of data readout, event building and data transportation, while the back-end takes care of the setup, run control, histogramming, data analysis and data storage. The system can manage high counting rates without dead time. For a detection system, the dead time is the time after a readout of events where the system is unable to record another event. The ADCs and TDCs can buffer up to 32 events at a time [16]. Essentially, the largest limitation to the DAQ system is pile-up, which is when the detection system starts processing another event before the previous event was finished. The events adds on top of each other, which leads to loss of information from both events.

During an experiment, the ROOT back end is mostly used to inspect the

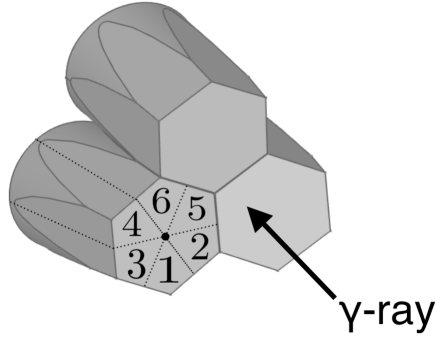


**Figure 3.7:** HPGe triple-cluster sketch, adapted from [37]. Each cluster is segmented into 6 parts. The core signal is marked by the black dot in the middle of the left crystal.

experiment live. As will be detailed in chapter 4, the offline ROOT analysis is very time consuming, and is largely performed after the experiment. This is the main part of the thesis.

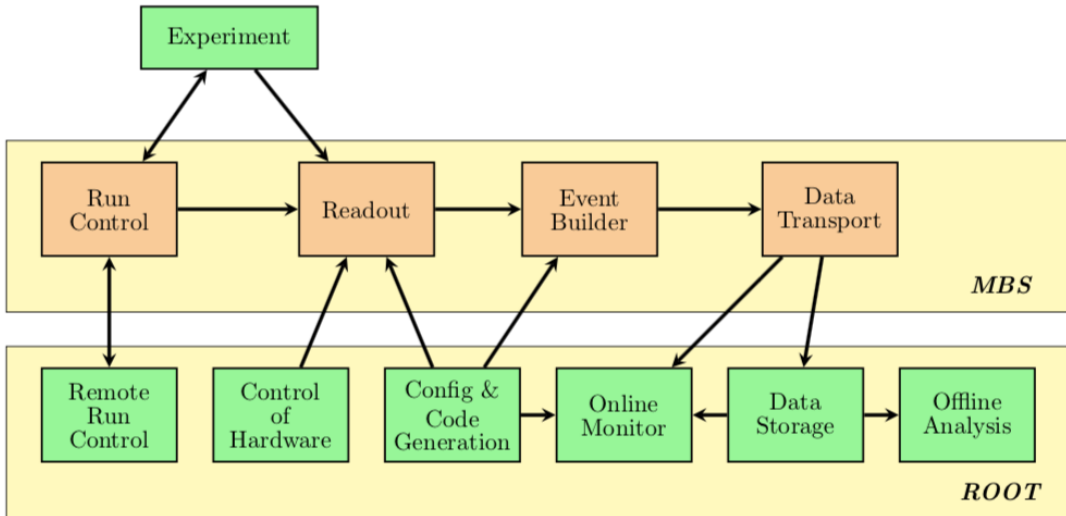


**Figure 3.8:** MAR<sub>a</sub>BQU tasks, adapted from [38].

## 3.4 The time structure

Figure 3.9 shows a schematic of the ISOLDE time structure. The Miniball data acquisition is happening during two time windows, the "on-beam" and "off-beam" windows. When REXEBIS releases the beam to the HIE-ISOLDE LINAC, a signal is also sent to generate the on-beam window. This window, called the "slow extraction mode" was  $800 \mu\text{s}$ , but in 2011 it was extended to 1 ms, because

the method of extraction of the beam was improved. All the data are read out after the on-beam window. This causes the DAQ to become dead for a while, so the next on-beam window is triggered when the DAQ is operable again. The off-beam window starts  $60 \mu\text{s}$  after the end of a readout, triggered by the disappearance of the DAQ is inoperable signal, to then allow the ADCs and TDCs time to start. In the off-beam window, which has the same duration of time as the on-beam window, data recordings of the background is conducted. After the off-beam window closes, a readout of the records is triggered. It is then possible to subtract the windows from each other to get the beam contribution. The DAQ system records the signals from each detector segment, which is individually time-stamped. With these records, a full reconstruction of the real events and coincidences are possible [41].

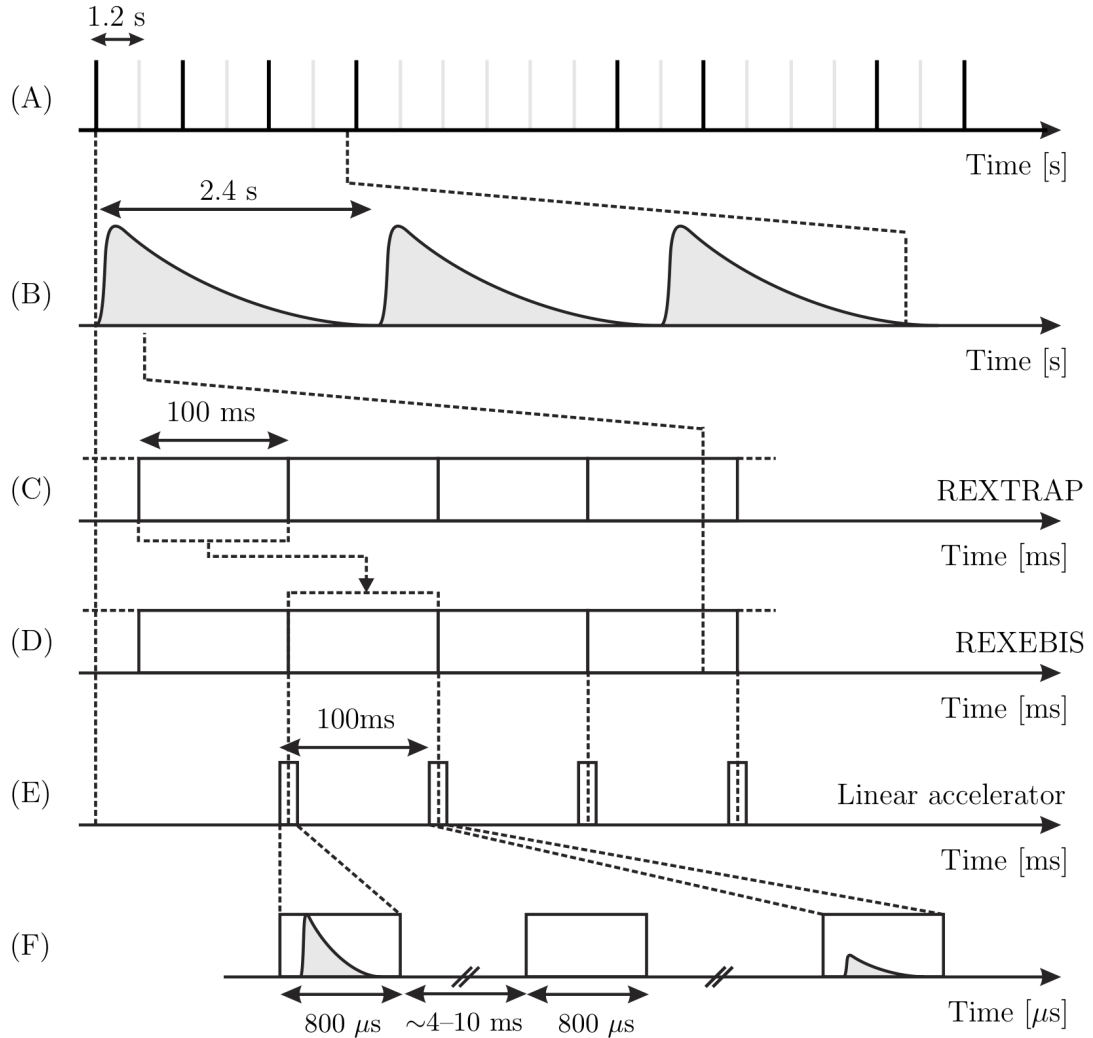


**Figure 3.9:** Schematic of the ISOLDE time structure. (A) The supercycle of proton beam bunches with a width of  $\approx 100 \mu\text{s}$  from the PSB separated by 1.2 s. The black vertical lines shows an allocation of the the bunches which the ISOLDE production target receives, while the others are distributed to other experiments. (B) The release profile of radionuclides from the production target, which is heavily modulated by the PSB cycle. (C+D) REXTRAP and REXEBIS beam bunches, synchronized with (E) the radio frequency (RF) window of the HIE-ISOLDE LINAC. (F) The "on-beam" and "off-beam" time window of  $800 \mu\text{s}$  using the Miniball setup. Figure courtesy of J. van de Walle [42].



# Chapter 4

## Data analysis

*"Not everything that can be counted counts, and not everything that counts can be counted."*

– William Bruce Cameron

In this chapter, the various programs and scripts applied in the detector calibration and data analysis will be introduced. Scripts developed in the present thesis work for the fitting procedures are slightly based on scripts written by Ville Virtanen<sup>1</sup> and Dr. Liam Gaffney<sup>2</sup>. The codes have been further developed and heavily re-written in the current work. Presently the code has only a minor resemblance to the original code. The remaining Python and bash scripts are written and developed by the author. All of the scripts written in C/C++ are dependent on the ROOT 6 framework, a C/C++ data analysis framework developed and maintained at CERN.

### 4.1 Data handling

The raw data from Miniball experiments essentially<sup>3</sup> comes in list mode (identification, energy, time), where every line is an event. It is stored in *.med*-files, MBS Event Data or also known as Miniball Event Data, with the naming convention *140Sm\_208Pb\_pos6\_0xy.med* for this experiment, where *x* and *y* are numbers between 0 and 9. The goal of the data analysis is to obtain Doppler-corrected  $\gamma$ -spectra with various conditions on particles and angles, in order to analyze the Coulomb excitation of  $^{140}\text{Sm}$ .

---

<sup>1</sup>Ville Virtanen is a student from University of Jyväskylä.

<sup>2</sup>Dr. Liam Gaffney is a research fellow at ISOLDE, affiliated with Miniball.

<sup>3</sup>The format is not entirely correct, since it has identification of where the particle and  $\gamma$  hit. A more detailed format is: identification, time, particle energy (front strip, back strip),  $\gamma$  energy (cluster, crystal, segment), etc.

For Miniball experiment data, the preferred sorting and analysis code is *MiniballCoulexSort* [43]. The main steps of how to download, install<sup>4</sup> and use it is outlined in the *README.md* file in the GitHub repository of Miniball, linked in the reference. The program is written in C/C++ and depends on the ROOT framework. It is under constant development at CERN-ISOLDE under the management of Dr. Liam Gaffney. Unfortunately the code isn't very well documented, so it takes some time to learn what it does and how to use it. To get from the raw data to the Doppler-corrected  $\gamma$ -spectra, the code is divided into a three step procedure:

### 1. MedToRoot

- converts the raw data to ROOT format

### 2. TreeBuilder / AQ4Sort

- event building
  - calibrate detectors and apply thresholds
  - use particle- $\gamma$  coincidences (correlations) to build events
  - store everything in a tree structure for easy access

### 3. CLXAna

- apply gates on particles and perform Doppler correction

For the CD, *TreeBuilder*<sup>5</sup> sorts each quadrant for itself, but it is not possible to see each pixel of the detector. In the front, each annular strip can be viewed and in the back each secular strip can be viewed as a whole, the back strip contains the energy information of all of the 16 annular strips. The secular strips cover a wide angular range, thus they show no sharp peaks. *TreeBuilder* also takes a number of command line flag options. If the *-cdpad* flag option is not used, then there will be no particle events, because they come into the CD. Other flag options will be introduced later in the chapter.

One program that is mentioned in the Miniball GitHub repository, but not showed how to use, is the *AQ4Sort*<sup>6</sup>. It is used in the same way as the *TreeBuilder* script, but it sorts the histograms in another way and it does not take any command line flag options. *AQ4Sort* is used before and during the calibration of the particle detector, because it gives information about every single ring and every

---

<sup>4</sup>If the **make** step fails, try doing a **make clean** and then **make**. The program might think that it is already built.

<sup>5</sup>*TreeBuilder* is found in the *~/GitHub/Miniball/MiniballCoulexSort/TreeBuilder* directory.

<sup>6</sup>*AQ4Sort* is also found in the *~/GitHub/Miniball/MiniballCoulexSort/TreeBuilder* directory.

single back strip (the "pixels" of the CD). These pixels are used for calibration and are made by gating on the annular (front) rings to see peaks in the secular (back) strips.

#### 4.1.1 Counting and naming convention

The numbering of the CD rings and strips are different in different programs and scripts. Histograms sorted by `TreeBuilder` starts counting from 0 (outermost ring) to 15 (innermost ring) as showed in [Figure 3.5](#). `AQ4Sort` starts from 1 (outermost ring) to 16 (innermost ring), shifted compared to `TreeBuilder`. For calibrated spectra, `TreeBuilder` shows the energy in MeV, while `AQ4Sort` shows energy in keV. The simulation program `kinsim3` counts from 1 (innermost ring) to 16 (outermost ring), the opposite of `AQ4Sort`. It is easy to be confused by all the different counting, but this thesis will try to use the counting order of `kinsim3` for the CD, it seems like the most logic way of counting. [Table 4.1](#) shows the CD wiring. A change of the wiring of the CD will probably not happen, but it is possible to choose a logic order of counting software wise. [Table 4.2](#) shows a comparison of the logic counting and the histogram naming from `TreeBuilder` and `AQ4Sort`. Calibration coefficients given to the calibration file, which is introduced in later sections, follow the naming convention of `TreeBuilder` in [Table 4.2](#).

## 4.2 Data conversion

In order to analyze the data in the ROOT framework, the first part of the code is just to convert the `.med`-files produced by MAR<sub>a</sub>BQ<sub>U</sub> into `.root`-files with the program `MedToRoot`. To avoid copy and paste the commands used with `MedToRoot` in the terminal for every data file, a bash script called `M2R.sh` was made to do this. It uses `MedToRoot` to take in as many files as you want, and convert it in one go. It takes one command line argument because it was initially developed to convert files from different elements, so it is fairly simple to expand. If no command line arguments are given, the script will print out how to use it. First all of the interesting raw data files are converted with the `M2R.sh` script. An example of the use with terminal output for the `140Sm_208Pb_pos6_0xy.med`-file with  $xy = 08$  is as follows:

```
$ cd ~/GitHub/MasterThesis/Scripts/sorting
$ ./M2R.sh Sm
opening file ../../Raw_data/Sm/140Sm_208Pb_pos6_008.med ...
EventBuffer::EventBuffer(GlobalSettings *)
Processing event number      0
Start trigger #14

Processing event number 130000
```

```

Stop trigger #15

Unpacked 132802 events:
wrong dgf hit pattern: 0 ( 0.0 %)
wrong adc headers: 0 ( 0.0 %)
# of overflows in adc channels: 599712 (451.6 %)
# of underflows in adc channels: 0 ( 0.0 %)
pattern unit mismatches: 0 ( 0.0 %)

Number of ebis pulses: 66351
Number of t1 pulses: 2211
Number of supercycle pulses: 429
committed 1 243 951 987 bytes to tree tr, 'Tree for on
beam data of Coulex setup@Miniball'
and 15 338 250 bytes to tree bg, 'Tree for on
beam background data of Coulex setup@Miniball'
and 237 454 436 bytes to tree tr, 'Tree for off
beam data of Coulex setup@Miniball'
wrote 97 189 bytes to file ../../Raw_data/Sm
/140Sm_208Pb_pos6_008_OnBeam.root => compressed by a
factor of 12799.3
, 18 362 bytes to file ../../Raw_data/Sm
/140Sm_208Pb_pos6_008_OnBeamBackground.root => compressed
by a factor of 835.3
, 67 934 bytes to file ../../Raw_data/Sm
/140Sm_208Pb_pos6_008_OffBeam.root => compressed by a
factor of 3495.4
and 22 167 bytes to file ../../Raw_data/Sm
/140Sm_208Pb_pos6_008_Scaler.root => compressed by a
factor of 2769.1

```

For each file converted with `MedToRoot`, the program makes four files with the naming convention

- `140Sm_208Pb_pos6_0xy_OnBeam.root`
- `140Sm_208Pb_pos6_0xy_OnBeamBackground.root`
- `140Sm_208Pb_pos6_0xy_OffBeam.root`
- `140Sm_208Pb_pos6_0xy_Scaler.root`

where the file of interest is the first one. The `OnBeam.root`-files are the files used in the sorting and event building with `TreeBuilder` and/or `AQ4Sort`.

## 4.3 Detector calibration

The general idea of the calibration is to make sure that the energy spectra from the detectors have the same physical features, that the detectors show the same

energy distribution at the same position for the same kind of particles or  $\gamma$ -rays hitting the same or the angular similarly place in the detectors. Calibration of the detectors minimize the measurement uncertainty by making the detectors more accurate and consistent. We want to determine centroids of peaks in the spectra, compare these with simulations using kinematics of the reaction and energy loss, to get linear coefficients of the detectors. In this context, the centroids refer to the channels of the maximum height of the peaks or the center of the peaks.

Both detector types in this experiment are semiconductor detectors. Except for silicon (as the CD), semiconductors generally require cooling to low temperatures before they can be operated. The basic principle of operation is that incoming ionizing radiation<sup>7</sup> creates electron-hole pairs in the semi-conducting material which are then collected by an electric field. The number of electron-hole pairs is proportional to the energy of the incoming radiation to the semiconductor [44].

Assuming a linear correlation between the energy  $E$  of the particle (or  $\gamma$ -ray) and the channel number  $n$  of the ADC (or DGF), we get

$$E = g \cdot n + a \quad (4.1)$$

where  $a$  is the offset in keV and  $g$  is the gain in keV/ $n$ . The gain  $g$  and the offset  $a$  are the coefficients needed to do the calibration. From Equation (4.1), the offset  $a$  can easily be expressed as

$$a = E - g \cdot n \quad (4.2)$$

To find the gain  $g$  in the CD denoted by  $p$  for particle (or  $\gamma$ -detectors denoted by  $\gamma$ ), at least two measuring points are needed, e.g. the peak energy of Sm and the peak energy of Pb for a given angle (or the peak of Eu and Ba explained in Section 4.3.6). The relationship can be written as

$$g_p = \frac{E_{\text{Sm}} - E_{\text{Pb}}}{n_{\text{Sm}} - n_{\text{Pb}}} \quad \left( g_\gamma = \frac{E_{\text{Eu}} - E_{\text{Ba}}}{n_{\text{Eu}} - n_{\text{Ba}}} \right) \quad (4.3)$$

where the peak energies are obtained from a simulation of the Coulomb excitation experiment and the channel numbers are obtained from the raw data of the actual experiment.

An assumption when calibrating is that the energy on the front side and the back side of the detector is the same. This is not entirely correct, since there will be a small energy loss when the particle goes through the front side, but in most cases this is negligible.

---

<sup>7</sup>For the CD, the ionizing radiation is the beam or target particles scattered from the reaction, while the ionizing radiation for the HPGe-detectors is the high-energy photons ( $\gamma$ ) from de-excitation of the nuclei.

### 4.3.1 Simulation

To calibrate the data, we need to know the expected energy of the centroids of the peaks. This was done by simulating the experiment using the program `kinsim3` [45] written by Dr. Liam Gaffney. The purpose of the program is to simulate the kinematics of a Coulomb excitation experiment done with the CD. The simulations are theoretical predictions of the energy distribution of the peaks for each ring in the CD. `kinsim3` gives simulated spectra for the LAB and CM frame, in addition to every (annular) strip of the CD. These strips are fitted, their energy centroids are collected and used in the calibration as shown in [Appendix E](#). For stopping powers, the program uses SRIM-2013 [46] generated files relevant to the `scattering/reaction?` with some random spread (SRIM is an acronym for the Stopping and Range of Ions in Matter). It also takes into account the energy loss in the dead layer of the detector, which is energy and angle dependent. The simulation considers cross sections in the way that the COULEX probability increases with the CM angle ( $0^\circ \Rightarrow P_{CE} = 0, 180^\circ \Rightarrow P_{CE} = 0.1539$ ), but the angular distribution is flat (`uniform?`).

The main function of `kinsim3` looks like this

```
void kinsim3( int Zb, int Zt, double Ab, double At,
    double thick /* mg/cm^2 */, double Eb /* MeV/u */,
    double dEb = 0.1 /* MeV/u */, double Ex = 1.0 /* MeV */,
    double res = 0.6 /* % */, double cd_dist = 28.0 /* mm */,
    bool flat = false /* angular distribution? */,
    long Nevts = 1E6, string srim_dir = "../srin" )
```

where  $Z_b$  and  $Z_t$  is the proton number of the beam and target respectively,  $A_b$  and  $A_t$  is the mass number of the beam and target respectively,  $thick$  is the target thickness in  $\text{mg}/\text{cm}^2$ ,  $E_b$  is the beam energy in  $\text{MeV}/\text{u}$ ,  $dEb$  is the `distribution?` of the beam energy in  $\text{MeV}/\text{u}$ ,  $Ex$  is the excitation energy,  $res$  is the detector resolution in percent,  $cd\_dist$  is the distance form the target to the CD in mm,  $flat$  is the choice of a uniform or angular distribution,  $Nevts$  is the number of events and  $srim\_dir$  is the relative path of the SRIM directory.

`kinsim3` was run with the following commands in the terminal to do the simulation

```
$ cd ~/GitHub/Miniball/kinsim
$ root
root [0] .L kinsim3.cc++
root [1] kinsim3(62, 82, 140, 208, 1.4, 4.65, 0.02, 1.0, 0.6,
    26.98, false, 1e6, "../SRIM")
... <showing output from program>
root [2] .q
$ mv 140Sm_208Pb_1.4mg_4.65MeVu_d0.02MeVu_res0.6.root ../..
MasterThesis/Sorted_data/sim_140Sm_208Pb.root
```

To load `kinsim3` into ROOT, the `.L <filename>` command was used. Adding the `'++'` at the end, forces ROOT to compile the code. After the simulation program was run, the file was moved and renamed with the `mv` command. `kinsim3` generates pdf-files of the stopping powers automatically. The rest of the plots are available inside the generated `.root`-file. To get the energy simulation for each ring, the function `simulation_plots()` from the script `ParticlePlot.cpp` was used.

```
$ cd ~/GitHub/MasterThesis/Scripts/plotting
$ root
root [0] .L ParticlePlot.cpp++
root [1] simulation_plot("setup.Sm.txt", 1)
... <showing output from script>
```

[Appendix E](#) shows the simulated energy for each ring of the CD, in addition to the fitted peaks of each ring. In the fitting of the simulated data, a Gaussian function with linear background was applied

$$g(x) = c + sx + Ae^{-\frac{1}{2}\left(\frac{x-\mu}{\sigma}\right)^2} \quad (4.4)$$

where  $c$  is the background constant,  $s$  is the background slope,  $A$  is the amplitude (Gauss constant),  $\mu$  is the mean (expected value) and  $\sigma$  is the standard deviation (Gauss width). [Table 4.3](#) shows the mid ring CD angles in the LAB frame for the front of the CD. A general kinematics simulation in the LAB frame is shown in [Figure 4.1](#).

### 4.3.2 Online calibration of the particle detector

Every year there is a campaign at ISOLDE, where the staff configures a settings-file if there are any changes in the setup system. In addition the staff makes a calibration file containing the calibration coefficients for the CD and the Miniball  $\gamma$ -detector array. For the calibration of the CD, a cocktail beam composed of different isotopes is accelerated into a specific target. For the calibration of the  $\gamma$ -detectors, usually two  $\gamma$  sources are placed in the target position. The data from these runs are used to make the calibration file. It contains the calibration coefficients for the ADCs and DGFs in addition to the Miniball geometry. This calibration file is adjusted for each experiment following the campaign period. In this way it is easy to sort and analyze during the experiments, to check if it is going well and to make preliminary Doppler-corrected  $\gamma$ -spectra. For IS558, the settingsfile `MBSettings2017_CLX_IS558.dat` and the calibration file `IS558-online.cal` was made.

The calibration step usually starts with `TreeBuilder`, which generates histograms of the CD and the  $\gamma$ -detectors separately. It also contains information

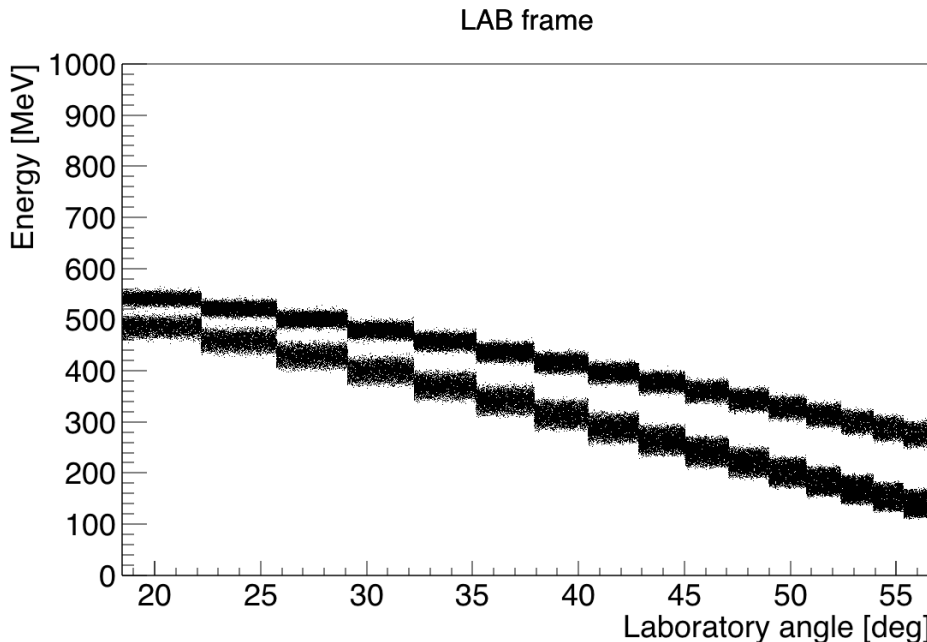


**Figure 4.1:** Simulation of the kinematics in the LAB frame for  $^{140}\text{Sm}$  on  $^{208}\text{Pb}$  at 4.65 MeV/u. The upper curve is the Sm and the lower curve is the Pb. Smaller angles corresponds to the inner rings and larger angles to the outer rings.

about the timing between particles and  $\gamma$ 's. In this step, the correlating of particles and  $\gamma$ 's is started. Just as for the `MedToRoot` program, the bash script `Q4S.sh` was made to utilize the `TreeBuilder` and `AQ4Sort` programs. `Q4S.sh` uses either `TreeBuilder` or `AQ4Sort` to sort a lot of data files in one go. From `TreeBuilder`, only the front side calibration coefficients of the CD can be extracted. For the back side, `AQ4Sort` has to be used. [Section 4.3.3](#) will go into more details about `AQ4Sort`. When using the online calibration, we don't need to use the `AQ4Sort` program, because we already have the calibration coefficients in the `IS558-online.cal` file. The coefficients are adjusted in the beginning and during the experiment. The `OnBeam.root`-files are loaded into `TreeBuilder` via `Q4S.sh` with the commands

```
$ cd ~/GitHub/MasterThesis/Scripts/sorting
$ ./Q4S.sh Sm online TB
... <showing output from script>
$ mv Sm_online-TreeBuilder-2019-06-24.root ../../Sorted_data/
```

After the sorting, the file was moved to a folder of sorted data with the `mv` command, and the relative path was given to the `setup_Sm.txt` file used as input in the `ParticlePlot.cpp` script. This script was made to extract different his-

tograms from the *.root*-file generated by either `TreeBuilder` or `AQ4Sort`. The script has to be loaded into the ROOT framework to work, because it was built to utilize the power of the framework. Histograms extracted from this step go through some formatting changes, to make them more presentable. To run the `ParticlePlot.cpp` in interaction with ROOT, the following commands are used

```
$ cd ~/GitHub/MasterThesis/Scripts/plotting
$ root
root [0] .L ParticlePlot.cpp++
root [1] plot_front_back_energy("setup_Sm.txt", "online")
... <showing output from script>
```

[Figure 4.5a](#) shows the back vs. front energy (online calibration) for the four different quadrants of the CD. The plots shows a part of a line for each front and back strip. An indication of a good calibration is when all detectors lie on a linear line ( $y = x$ ), meaning that the front side and the back side of the CD has detected the same energy. From the figure we see that not all detectors fit the line, indicating that there are some calibration coefficients wrong in some of the strips. One major problem with the online calibration is that a number of the back strips have the wrong gains as shown in [Figure 4.6b](#).

### 4.3.3 User calibration of the particle detector

An ambitious goal of the calibration was to make a program that could automatically fit the centroid of the peaks needed. It turned out to be very difficult, and it became more and more manual labor. Because of the complex peak shapes, it is very hard to do an automatic fitting it seems. [Figure 4.2](#) shows one strip that is easy to calibrate and one that is difficult to calibrate. The peaks demands very much individual care, which is very difficult to do with a automatic program. In logarithmic (log) scale the data looked more Gaussian distributed, but it is not the case in linear scale. For the centroids, it was very hard to tell in log scale how precise the automatic fitting was. It turned out that it was not very precise, so a lot of time was wasted looking at the data in log scale.

On the front side of the CD, there is effectively only two measuring points per angle interval. If the contaminant in the spectra was known and if it only consists of one element, it could have been a third measuring point. On the back side of the CD there are two peaks per gated annular strip that can be fitted, so per back strip a maximum of 32 measuring points. By doing a function fit, Gaussian or other, the centroids of the peaks for both Sm and Pb can be extracted. On the front side of the CD, [Equation \(4.2\)](#) and [Equation \(4.3\)](#) can be used to calculate the calibration coefficients. For more than two centroids per strip, as the back side of the CD have, linear regression is used to find the best fit of the calibration coefficients.

Calibrating the back strips of the CD is the same as the front, however because they cover a large range of angles in the  $\theta$  direction (according to [Figure 2.1a](#)), a gate on one of the front strips is needed to define an angle and thereby an energy. For this purpose, the program `AQ4Sort` is used. It operates the same files as `TreeBuilder` does, but with the purpose of making every combination of gates on front and back strips so that the front and back centroids for every "pixel" of the detector is available.

The total amount of annular strips to calibrate on the front side of the CD is 64, since there is 4 quadrants with 16 rings. On the back side, there is effectively 48 secular strips, 4 quadrants with 12 strips. To fully calibrate the CD, we need all the centroids of the peaks from both sides, 128 centroids ( $64 \text{ annular strips} \cdot 2 \text{ peaks/stripe}$ ) on the front side and 1536 centroids ( $48 \text{ secular strips} \cdot 2 \text{ peaks/stripe} \cdot 16 \text{ rings}$ ) on the back side. This gives a total of 1664 centroids to extract, which is not a task one would like to do manually. For a quick calibration, or a bare minimum calibration, one needs two peaks in each annular strip and two peaks in each secular strip, making it 224 centroids. By taking more centroids, which is generally a good idea, it is possible to check for non-linearities or instabilities in time. It makes the calibration more precise.

[Figure 4.3](#) shows a flowchart of the programs, scripts and files used in the user calibration. The idea was to use the `kinsim3()` function from `kinsim3.cc` to simulate the data and the `Q4S.sh` script to sort the experimental data with `AQ4Sort` to get each pixel of the CD. This data could either be analyzed in ROOT with the `TBrowser()` or through different functions in `ParticlePlot.cpp`. From either ROOT or `ParticlePlot.cpp`, information about the range of the peaks and guesses of the centroids of Pb and Sm would be written down in input files used in `ParticleFit.cpp`. Here the automatic fitting would have used the input files to fit the peaks, collect the centroids and written them to output files which would have been used as input files in `particle-calibration.py`. In this Python script, the centroids would have been plotted and a linear regression method using least squares of a first degree polynomial fit<sup>8</sup> would have fitted a line to reproduce the points as best as possible. It would also write the gains and offsets to separate output files, which would be used as input in `ADC_generator.py`. This Python script will write the calibration coefficients to the terminal, and from there it is possible to copy and paste it into the calibration file `IS5558-user.cal`. This calibration file is then used to sort the data once more with `Q4S.sh` using `TreeBuilder` and the new calibration coefficients. To visualize plots after a new calibration, either ROOT or `ParticlePlot.cpp` can be used. The gray boxes related to the  $\gamma$ -calibration will be discussed in [Section 4.3.6](#).

The downfall of the automatic centroid collector came when trying it on the secular strips of the CD. There is just too much individual differences to calibrate

---

<sup>8</sup>Polynomial fit: <https://docs.scipy.org/doc/numpy/reference/generated/numpy.polyfit.html>

the secular strips with a simple script given a channel range for all 12 back strips. This was discovered way too late. There isn't any range to "rule them all", at least since the fitting function can behave very strange given a too small or too big range. Another problem is the complex shape of the peaks. To implement a proper automatic fitting program, one would have to find a function with a negatively-skewed distribution, where most of the data values are concentrated on the right side of the distribution graph. Sadly this was discovered too late to implement it.

In some spectra it was very hard to determine the centroid of the Pb peaks, as shown in [Figure 4.2b](#). To try to solve this problem, additional data from an experiment conducted right before this one was applied. The experiment was IS553,  $^{144}\text{Ba}$  on  $^{58}\text{Ni}$ , and the reason for trying additional data was to try to get calibration for the lower energy spectra. But sadly the data from the IS553 experiment was a bad fit with this experiment. Unfortunately there is no way of knowing if a data set is useful or not until it is tested. It may be that the energy loss or target thickness was wrong, or that the beam energy was different, or that the simulation didn't account for all the details of the stopping. The only way to get a good calibration is to have as much data as possible and then kick out the bad data until there is a good fit. What was clear at the moment was that the scatter between the data points from the different reactions was too large to simply average out with a straight line fit. It is important to select data that agree. The fitting just didn't seem reliable. It gave a steeper slope than the online calibration. By looking at the front vs. back energy plots, the diagonal lines were almost disappearing in the middle, and they were a lot broader than the online calibration. One big problem of not using the IS553 data, was that it was not possible to get any good calibration coefficients for front ring 16 and maybe also ring 15. But this problem was also found in the IS553 data. It would have been nice with some low-energy points as well as high-energy points in order to do the calibration. The user calibration did appear to get worse in a few aspects. Firstly, the diagonal line in the front vs. back energy spectra was not as defined as the online calibration. Secondly, the off-diagonal events seemed to increase, implying that there was an increase in the mismatch of front and back events. The latter could be due to the visualization coming from the  $z$ -scale, since there are a different number of events in the quadrants.

Looking at the energy vs. channel plots, it was clear that something was not good. It was clear that a Gaussian fit did not work. Since the Gaussian distribution was a bad fit for the experimental data, a built in function in ROOT of a 4th degree polynomial was tried out to fit the complex peak shapes. The predefined ROOT function

$$f(x) = p_0 + p_1 \cdot x + p_2 \cdot x^2 + p_3 \cdot x^3 + p_4 \cdot x^4 \quad (4.5)$$

sets the initial values of the parameters automatically. Only a initial guess of

the parameters have to be given. It turned out that this did not match the peak shapes either.

It was anyways decided to stick with the online calibration for this thesis since there is no time to do a new calibration of the detectors. A lot of time have been used on scripts, and then the auto-fitting was a much harder problem than first expected because of the shape of the peaks. The user calibration of the CD is basically the online calibration without the innermost ring. An explanation of why the innermost ring was removed can be found in [Section 4.3.8](#). As [Figure 4.5b](#) shows, the calibration of the CD got better by removing the innermost ring. The most visibly lines which did not fit  $y = x$  vanished, implying that most of the problem was in fact the coefficients of ring 1.

In several strips in quadrant 1 and 4, there was a double-peak structure of  $^{140}\text{Sm}$  like the one in [Figure 4.4a](#). To explain this we have to look at the two-dimensional (2D) spectrum in [Figure 4.4b](#), which can be divided into four parts [\[37\]](#):

- Region 1: The measured energy at the front and back side of the CD are equal, which indicates that they are linearly correlated.
- Region 2: In these events the detected energy is lower at the back side, while at the front side the energy is artificially increased. One explanation of this is if the energy is detected in one strip on the front side, but is shared between two neighboring strips on the back side. The reduced energy on the back side only occurs when the impact position is close to or inside the dead layer between two strips. The current from the two neighboring strips can possibly induce an artificially higher energy to the front side of the CD. A similar phenomenon has been observed in segmented HPGe detectors discussed in detail in [\[47–51\]](#). Another explanation is that there are some charge trapping and charge recombination of the particle-hole pairs. This causes a Pulse-Height Defect (PHD) in the detector signal, which is discussed in detail in [\[52, 53\]](#).

The second Sm-peak at higher energies in [Figure 4.4a](#) comes from the projection of the 2D spectrum from [Figure 4.4b](#) onto the x-axis.

- Region 3: This area has a similar, but different pattern to region 2. The detected energy is lower at the front side, while it is higher at the back side of the CD. Here, the reduced energy on the front side originates from charge sharing between neighboring annular strips if the incoming particle hits close to or inside the dead layer. On the back side, the strips are coupled to a positive voltage which protects against the induction of an artificially higher energy by the front side charge sharing. These phenomena are discussed in detail in [\[54, 55\]](#).

- Region 4: This structure originates from the same place as region 2. These events occur because of the paired up secular strips on the back side of the CD. Because of the connection of two neighboring strips, the charge is split among them and it is added up to the total charge.

In [Figure 4.6](#) the energy of every strip is shown for each quadrant separately.  
**What can I say about these plots?**

An example of how to use `Q4S.sh` with `TreeBuilder` is shown below

```
$ cd ~/GitHub/MasterThesis/Scripts/sorting
$ ./Q4S.sh Sm user TB
____ TreeBuilder ____
input file(s):
... <shows a list of all input files>
output file: Sm_user-TreeBuilder-2019-06-20.root
calibration file: ../../Miniball-config/IS558-user.cal
WeightPR: 0.75
Particle distribution:
Q0 fired: 12243817
Q1 fired: 12277727
Q2 fired: 11479362
Q3 fired: 10936096
Finished.
$ mv Sm_user-TreeBuilder-2019-06-20.root ../../Sorted_data/
```

In the output, there is a line reading WeightPR: 0.75. This parameter is needed when calibrating the  $\gamma$ -detectors explained in [Section 4.3.6](#). A similar example of how to use `Q4S.sh` with `AQ4Sort` is shown below

```
$ ./Q4S.sh Sm user Q4
Info: No flag option for 'AQ4Sort'. Ignoring optional flag.
____ AQ4Sort ____
calibration file: ../../Miniball-config/IS558-user.cal
input file(s):
... <shows a list of all input files>
output file: Sm_user-AQ4Sort-2019-06-24.root
$ mv Sm_user-AQ4Sort-2019-06-24.root ../../Sorted_data/
```

**Skal jeg forklare mer om "the fitting procedure" i denne seksjonen?**

#### 4.3.4 Threshold

The continuum of events at low energy comes from charge sharing between the strips. [Figure 4.7](#) shows the big peak of the charge sharing on the front and back side of the CD. This peak is called the "pedestal", because it is like a massive statue in front of the interesting data. For the very heavy ions, the total amount

of charge deposited gets split between neighboring strips of the CD. There is a single common gate for each ADC, containing channels from one CD quadrant. Therefore, when there is an event in one strip of the CD all channels are readout, but the channels without a real event read a "zero" energy. These are the events in the pedestal. A software threshold is applied to cut away the pedestal. For each ADC channel, the threshold can, and should be set. One should define the threshold for each ADC channel to be above this peak. After a correct calibration is applied, the pedestal will be calibrated out of the physical energy range.

*MiniballCoulexSort* does perform some tricks to try to recover the correct energy and position of the particles, but that depends on counting the number of strips that fire. The default threshold is set to channel 100 if none is given in the calibration file. In some cases this is too much and in others this is not enough. If the threshold is set too low, pedestal events are included and it will get things wrong. If the threshold is too high, some events that have charge sharing will be missed and this leads to getting the wrong energy for the particle. The goal is to not include the pedestal, and don't cut away too many events from the continuum. It is easier to set thresholds in linear scale than logarithmic, because in log scale the threshold value will decrease very much and it is difficult to see where to set the limit. [Figure 4.8](#) shows the software threshold set in the user calibration file on the front and back side for one strip on each side. These values were also put into the online calibration file.

The key spectra to look at are [Figure 4.9](#) and [Figure 4.10](#). [Figure 4.10](#) shows how many particles have strips fired on the front side or back side of the CD. It counts how many particles have  $x$  strips fired on the front side and  $y$  strips fired on the back side. [Table 4.4](#) explains the different debug IDs. The goal is to have a lot more counts in CD debug ID 0 compared to ID 3 as shown in [Figure 4.10](#). If we have too many debug ID = 3, then the threshold is too low. If we have a large continuum/background in [Figure 4.9](#), the thresholds are too high. The best thing to do is to play about with different values to see what is best. Debug ID 20 is when no particle can be found, because there is no energy registered in either the front or the back strips. This can only happen when the front energy is below the software threshold set by the user in the calibration file and the back energy is either in a broken strip or is also below the software threshold. It is likely that it is some noise events or charge sharing that comes below the threshold.

### 4.3.5 Time calibration

Each quadrant of the CD is independently connected to a Time to Digital Converter (TDC), which keeps track of the time of registered particle- $\gamma$  (**and particle- $\gamma\text{-}\gamma$ ?**) coincidences. The ADCs and DGFs record an energy and a time-stamp with 25 ns ticks. It is the multiplicity of the output of the DGFs that is used to

generate the  $\gamma$  signal, which in turn is used to make the particle- $\gamma$  coincidence.

The purpose of the time calibration is to align the time spectra so that a prompt time gate can be set. In this way it is possible to correlate particles and  $\gamma$ -rays. Using the `ParticlePlot.cpp` script, the ADC time offset spectra can be extracted by the following commands

```
$ cd ~/GitHub/MasterThesis/Scripts/plotting
$ root
root [0] .L ParticlePlot.cpp++
root [1] check_ADC_time_offsets("setup_Sm.txt")
```

or they can be manually reached by

```
$ cd ~/GitHub/MasterThesis/Sorted_data
$ root Sm-user-TreeBuilder-2019-06-20.root
root [1] new TBrowser()
```

In the browser, the histograms are named `tdiff_gp_i`, where  $i$  is a number between 0 and 3 implying quadrant 1 to 4. They lie within the `.root`-file without a folder. [Figure 4.11](#) shows the time offsets for the CD. The peaks of these plots have the interesting x-axis values. Zooming into the peaks, it is very clear what the value in each quadrant is. The values can change depending on the amount of data sorted, so it is wise to double check them when more data is added to the `.root`-file. After the peak values have been collected, they should be written into the calibration file under ADC time offsets (ticks). The time offsets of this experiment was the following

```
# ADC time offsets (ticks)
adc_0.TimeOffset: 0
adc_1.TimeOffset: -2
adc_2.TimeOffset: -3
adc_3.TimeOffset: 5
```

After the software threshold and ADC time offsets are added to the calibration file, a re-run of the `Q4S.sh`-step with `TreeBuilder` and the updated calibration file has to be conducted.

### 4.3.6 Calibration of the $\gamma$ detectors

The online calibration of the  $\gamma$  detectors is quite good for most detectors in a certain energy range, because it is designed to be that way. During the setup of the experiment, a hardware calibration of the  $\gamma$  detectors was performed. The gains of each DGF are matched so that the online analysis is more straightforward. However, there are non-linearities and drifting offsets and gains over time

that have to be corrected for with a proper calibration using the  $^{133}\text{Ba}$  and  $^{152}\text{Eu}$  source data collected in the end of the experiment. The  $^{133}\text{Ba}$  and  $^{152}\text{Eu}$  sources are placed at the target position simultaneously, back to back, and the data is also used to determine the relative efficiency of Miniball.

Histograms used for  $\gamma$ -detector calibration sorted by `TreeBuilder` use the naming convention  $E\_gam\_seg\_c\_d\_s$ , where  $c \in [0, 7]$  is the cluster number,  $d \in [0, 2]$  is the detector number and  $s \in [0, 6]$  is the segment number, where  $s = 0$  is actually the core signal. There was no time to do a proper calibration of the  $\gamma$ -detectors in this thesis, but the online calibration was quite good anyways. Just as for the particle calibration, scripts for  $\gamma$ -detector calibration was supposed to be made. The gray boxes in [Figure 4.3](#) are related to the  $\gamma$ -detector calibration. The idea was to use the `Q4S.sh` script to sort the experimental data with `TreeBuilder`. Then use `GammaPlot.cpp` or ROOT to analyze the data using the  $\gamma$ -histograms mentioned above. Information about the peaks should have been used as input in `GammaFit.cpp`, where the fitting would have taken place. The Python scripts `DGF-generator.py` and `Geometry-generator.py` does at the moment reproduce the calibration coefficients and geometry parameters from the online calibration. These were supposed to be changed to fit the proper calibration in time. The output from these scripts should have been copied and pasted into the calibration file `IS558-user.cal`. [Section 4.3.7](#) explains why it is important to know the geometry of the  $\gamma$ -detector setup. After the calibration coefficients and the geometry parameters are added to the calibration file, a re-run of the `Q4S.sh`-step with `TreeBuilder` and the updated calibration file has to be conducted. The next step is to do a Doppler correction, which is explained in [Section 4.3.7](#).

After the Doppler correction the `CLXAna` program needs to be used. in order to get the Doppler-corrected  $\gamma$ -spectra to analyze the Coulomb excitation of  $^{140}\text{Sm}$ .

`CLXAna` makes event trees and energy spectra for both particle and  $\gamma$  detection which can be used for analyzing the Coulomb excitation events.

The `-s` flag (singles) is for adding particles which come without a  $\gamma$ -ray and the `-addback` flag is for adding Compton scattered events together in the Miniball clusters.

### Then I have misunderstood the singles method?

There are three methods of sorting the events from Miniball; singles, add-back and reject. When applying the singles method, every  $\gamma$ -ray entering a detector is counted as an event. There are no assumptions of Compton scattering in this kind of sorting. This implies that some of the events counted as true events are in fact scattered  $\gamma$ 's corresponding to a different energy. When utilizing the add-back method, events occurring in neighboring detectors in the same cluster within a 100 ns time window are added together as a single event. The energies of the events that occurred in the separate segments are summed, and

the segment with the highest energy is assumed to be the position of the incident  $\gamma$ -ray. An advantage of the add-back method is that the full energy of a single  $\gamma$ -ray, which has undergone a Compton scattering process, can be reconstructed to increase the efficiency. A disadvantage of the method is the uncertainty in the assumptions of the addition of several events into a single event. The timing resolution cannot distinguish true  $\gamma\text{-}\gamma$  events from Compton scattering events. The add-back method can cause an increase in the intensity of  $\gamma$ -ray sum peaks since it has no way to deal with pile-up of different  $\gamma$ -rays, thus no correction is performed when different  $\gamma$ -rays pile up in the detector. When applying the reject method for the sorting, events occurring in neighboring detectors in the same cluster within a 100 ns time window is excluded as an event. The total statistics for the reject method will therefore be smaller. If the amount of total statistics is large, it is possible and maybe even advantageous to apply the reject method, because it will give a higher probability of getting the actual full energy peaks of the  $\gamma$ -rays detected.

All input parameters for **CLXAna** are stated in the GitHub repository of *MiniballCoulexSort*, but they are not explained in detail. From private communications with Dr. Liam Gaffney, some of the input parameters now have a little more context

- c** The configuration file is a file that contains all of the input parameters, except -cut, in order to not type the parameters into the command line each time.
- cut** The cut file is a root file containing the graphical cuts on the kinematics from the "part" histogram. This is the only file path that is not possible to put into the configuration file as stated above.
- Ex** Excitation energy of the state that you want to perform the Doppler correction for, given in keV. This is not a significant value.
- depth** The depth of the interaction in the target in mg/cm<sup>2</sup>. Usually assumed to be half of the thickness of the target. Different values can be tested to see if it improves the Doppler correction.
- cdoffset** The rotation of the CD detector in the phi angle, with a default value of 242.6 degrees. This can be optimized, but the value is usually around the default value.
- deadlayer** The thickness of the Si dead layer in mm, with a default value of 0.0007 mm.
- spedelist** Not needed for this experiment.
- bg\_frac** This value depends on the time windows defined in TreeBuilder, which means it should be -0.75 for the current version. The number can also be

checked by taking the ratios of the beta-decay background peaks in the prompt gammas "p" and random gammas "r" spectra in the output file of **CLXAna**.

As mentioned in [Section 4.3.3](#), one line in the output from **Q4S.sh** using **TreeBuilder** was

```
WeightPR: 0.75
```

This value is the one supposed to be used with the **-bg\_frac** input parameter when using **CLXAna**. Even though the WeightPR value is positive, the input parameter is supposed to be negative. In this thesis, the input parameters used with **CLXAna** can be found in the *config-IS558.dat* file.

The first time **CLXAna** is run, every input parameter except **-cut** needs to be provided. A plot of energy vs. LAB angle named "part" is needed in order to make the cut file, and this plot is found inside the *.root*-file sorted by **CLXAna**. It would have been more logical to include this plot in **TreeBuilder**, but for some reason it is not. There is also a plot named "part" inside the *.root*-file sorted by **TreeBuilder**, but this contains energy vs. annular strip. To make the cut file, the "part" plot from the output file of **CLXAna** needs to be opened. It is also advised to use log scale on the z-axis, the draw option "colz" and to zoom into the correct area. From this plot, graphical cuts around the beam-like and target-like particles needs to be done separately. After making the cuts, right click and SetName to set the names to "Bcut" and "Tcut" respectively. Then right click and SaveAs, giving the name of a *.root*-file of your choice for each cut separately. The key is the *.root* extension so that it knows which format to use. In this thesis, the files were saved as *Bcut.root* and *Tcut.root* respectively. The two files can be added together using a ROOT program called **hadd**, which is used like this

```
hadd outputfile.root input_file_1.root input_file_2.root
```

If the files are supposed to be saved somewhere else, the absolute path can be given. With the cut files above, this step was done by

```
$ cd ~/GitHub(ROOT-framework/build/bin
$ hadd /Users/trondwj/GitHub/MasterThesis/Sorted_data/
      outputfile.root /Users/trondwj/GitHub/MasterThesis/
      Sorted_data/part.root /Users/trondwj/GitHub/MasterThesis/
      Sorted_data/Bcut.root /Users/trondwj/GitHub/MasterThesis/
      Sorted_data/Tcut.root
```

Now that the cut file is made, a second run of **CLXAna** can be performed. In order to not copy and paste all command into the command line, a script named

`Coulex.sh` was made to sort the data with CLXAna. It uses the configuration file `config-IS558.dat` and the cut file `outputfile.root`. In addition it takes one command line flag of the four different options of sorting the data

```
'-d' (default)
'-s' (singles)
'-a' (addback)
'-r' (reject)
```

An example of running the script and the output given by CLXAna is shown below

```
$ ./Coulex.sh -d
____ Coulex: default ____
Input parameters:
Zb = 62
Ab = 140
Zt = 82
At = 208
Eb = 4650 keV/u
Ex = 531 keV
thick = 1.4 mg/cm2
depth = 0.7 mg/cm2
cddist = 26.98 mm
cdoffset = 242.6 degrees
deadlayer = 0.0007 mm
contaminant = -1 mg/cm2
spededist = 23.6 mm
bg_frac = -0.75
srilm = /Users/trondwj/GitHub/MasterThesis/SRIM
cutfile = ../../Sorted_data/outputfile.root:Bcut:Tcut
Begin g_clx loop.
Info in <TCanvas::Print>: pdf file /Users/trondwj/GitHub/
    MasterThesis/SRIM/140Sm_208Pb.pdf has been created
Info in <TCanvas::Print>: pdf file /Users/trondwj/GitHub/
    MasterThesis/SRIM/208Pb_208Pb.pdf has been created
Info in <TCanvas::Print>: pdf file /Users/trondwj/GitHub/
    MasterThesis/SRIM/140Sm_Si.pdf has been created
Info in <TCanvas::Print>: pdf file /Users/trondwj/GitHub/
    MasterThesis/SRIM/208Pb_Si.pdf has been created
Initialising histograms...
Looping over events...
Warning in <TClass::Init>: no dictionary for class trevts is
    available
1-particle events = 89020258%
Finished.
```

As seen above, the cut file `outputfile.root` is provided as

```
outputfile.root:Bcut:Tcut
```

The :Bcut:Tcut ending are the names of the cuts in the file. The first cut is the beam-like and the second is the target-like. These names can be chosen otherwise, but they must match the names set in the first step.

[Figure 4.12](#) shows the cuts of the beam and target for the detected particle events. These cuts are used in the Doppler correction of the  $\gamma$ -rays. [What more can I say?](#)

[Figure 4.13 ... what can I say about this plot?](#)

[Table 4.5](#), not sure how to make this table. How is the histogram names and the calibration coefficients linked?

### 4.3.7 Doppler correction

[Does this belong in the theory chapter?](#)

In order to perform the Doppler correction, the interaction point angles in the Miniball frame of reference has to be known. [Figure 4.14](#) shows a sketch of the Miniball cluster geometry and [Table 4.6](#) gives the angles and distance of the different clusters. The parameters  $\theta$ ,  $\phi$  and  $R$  describes the position of the central axis of the detector clusters, while  $\alpha$  describes the orientation about the axis of the cluster. All these parameters are needed to calculate the position of the segments or the position of a point determined by the pulse-shape analysis. The interaction point is determined either from the segment with the largest energy or using a pulse-shape analysis. In the first case, the position of the center of each segment has to be known. In the second case, geometrical information to relate the time-to-steepest slope and ratio of the mirror charge amplitudes to the angle between the interaction point, the target and the emitted particle need to be known. This is built into `MiniballCoulExSort`, which does the geometrical calculations. The geometry parameters of the Miniball clusters has to be written into the calibration file.

Because of the significant velocity of the scattered particles, the emitted  $\gamma$ -rays from the particle de-excitation has a Doppler shifted  $\gamma$ -energy given by

$$E_\gamma = \frac{E'_\gamma}{\gamma(1 - \beta \cos \theta)} \quad (4.6)$$

where  $E_\gamma$  is the  $\gamma$ -energy detected in the LAB frame,  $E'_\gamma$  is the  $\gamma$ -energy in the nucleus' frame of reference,  $\beta = \frac{v}{c}$ ,  $v$  is the nucleus' velocity,  $c$  is the speed of light,  $\theta$  is the angle of the emitted  $\gamma$ -ray with respect to the nucleus' direction of motion and  $\gamma = 1/\sqrt{1 - \beta^2}$  is the Lorentz factor. Since both the CD and the HPGe-array are segmented, the emission angle  $\theta$  of the  $\gamma$ -ray can be calculated by

$$\cos \theta = \sin \theta_p \sin \theta_\gamma \cos(\phi_p - \phi_\gamma) + \cos \theta_p \cos \theta_\gamma \quad (4.7)$$

where  $(\theta_p, \phi_p)$  and  $(\theta_\gamma, \phi_\gamma)$  are the detection angles of the particle and  $\gamma$ -ray respectively,  $(\theta_p, \theta_\gamma)$  are the angles with respect to the beam axis and  $(\phi_p, \phi_\gamma)$  are the azimuthal angles [16, 57]. The Doppler correction factor is found by combining [Equation \(4.6\)](#) and [Equation \(4.7\)](#) into

$$\frac{E'_\gamma}{E_\gamma} = \gamma(1 - \beta(\sin \theta_p \sin \theta_\gamma \cos(\phi_p - \phi_\gamma) + \cos \theta_p \cos \theta_\gamma)) \quad (4.8)$$

### 4.3.8 Broken detector segments

The innermost ring of the CD was very damaged by the bombardment of particles hitting it, so it had to be removed from the data set. It was impossible to separate the beam and target peaks as shown by [Figure 4.15a](#). This was unfortunate since the ring 1 has the most statistics. Si detectors don't last forever, it was "old" and supposed to be changed after our experiment.

On the back side of the CD, one pixel was acting weird compared to the other back strips in the same quadrant. Secular strip 1 (B1) gated on annular strip 16 in quadrant 4 showed a lot more counts than all of the other strips as shown by [Figure 4.15b](#). There was also other rings where B1 was a bit off, but not nearly as much as in the named pixel. Maybe B1 should have been excluded from the data set, but it was not in this thesis.

In [Figure 4.13](#), core ID 20 was removed because it was a broken segment. Core ID 15 shows fewer counts than the neighbors, this is because it was a cross-talk issue involving a dead segment in detector 18A (cluster 5, core 0, segment 1 and 2). It means that some events had to be vetoed to avoid double-peaking, and this reduces the efficiency.

Excluding detector strips is easy, the only thing to do is to set gain and offset to -1, or gain to 0 and offset to -1. That will make the energy calibration negative, and fall out of the scope. It is the way it is usually done for dead CD strips or dead  $\gamma$ -detectors.

**Table 4.1:** CD wiring for Coulomb excitation experiments.

ADC	Quadrant	Channel	Front strip [F] or back strip [B]
0 - 3	1 - 4	0	F
0 - 3	1 - 4	1	F
0 - 3	1 - 4	2	F
0 - 3	1 - 4	3	F
0 - 3	1 - 4	4	F
0 - 3	1 - 4	5	F
0 - 3	1 - 4	6	F
0 - 3	1 - 4	7	F
0 - 3	1 - 4	8	F
0 - 3	1 - 4	9	F
0 - 3	1 - 4	10	F
0 - 3	1 - 4	11	F
0 - 3	1 - 4	12	F
0 - 3	1 - 4	13	F
0 - 3	1 - 4	14	F
0 - 3	1 - 4	15	F
0 - 3	1 - 4	16	B
0 - 3	1 - 4	17	B
0 - 3	1 - 4	18	B
0 - 3	1 - 4	19	B
0 - 3	1 - 4	20	B
0 - 3	1 - 4	21	B
0 - 3	1 - 4	22	B
0 - 3	1 - 4	23	B
0 - 3	1 - 4	24	B
0 - 3	1 - 4	25	B
0 - 3	1 - 4	26	B
0 - 3	1 - 4	27	B
0 - 3		28	Empty
0 - 3		29	Empty
0 - 3		30	Empty
0 - 3	1 - 4	31	PAD
4		0	Ionization Chamber
4		1	Ionization Chamber

**Table 4.2:** The logic counting and the naming of histograms from TreeBuilder and AQ4Sort.

Quadrant	Logic counting		TreeBuilder	AQ4Sort
	Front strip [F]	Back strip [B]		
1	F 1		adc_0_15	fE_Q1_f16
1	F 2		adc_0_14	fE_Q1_f15
1	F 3		adc_0_13	fE_Q1_f14
:	:		:	:
1	F 15		adc_0_1	fE_Q1_f2
1	F 16		adc_0_0	fE_Q1_f1
1	B 1		adc_0_16	bE_Q1_b1
1	B 2		adc_0_17	bE_Q1_b2
1	B 3		adc_0_18	bE_Q1_b3
:	:		:	:
1	B 11		adc_0_26	bE_Q1_b11
1	B 12		adc_0_27	bE_Q1_b12
2	F 1		adc_1_15	fE_Q2_f16
:	:		:	:
2	F 16		adc_1_0	fE_Q2_f1
2	B 1		adc_1_16	bE_Q2_b1
:	:		:	:
2	B 12		adc_1_27	bE_Q2_b12
3	F 1		adc_2_15	fE_Q3_f16
:	:		:	:
3	F 16		adc_2_0	fE_Q3_f1
3	B 1		adc_2_16	bE_Q3_b1
:	:		:	:
3	B 12		adc_2_27	bE_Q3_b12
4	F 1		adc_3_15	fE_Q4_f16
:	:		:	:
4	F 16		adc_3_0	fE_Q4_f1
4	B 1		adc_3_16	bE_Q4_b1
:	:		:	:
4	B 12		adc_3_27	bE_Q4_b12

**Table 4.3:** The mid ring CD angles in the LAB frame, with a distance from the target to the CD of 26.98 mm. Ring 1 is the innermost ring and ring 16 is the outermost ring. The centroid energies comes from simulation with `kinsim3`.  $E_t$  is the energy of the target particle (Pb) and  $E_b$  is the energy of the beam particle (Sm).

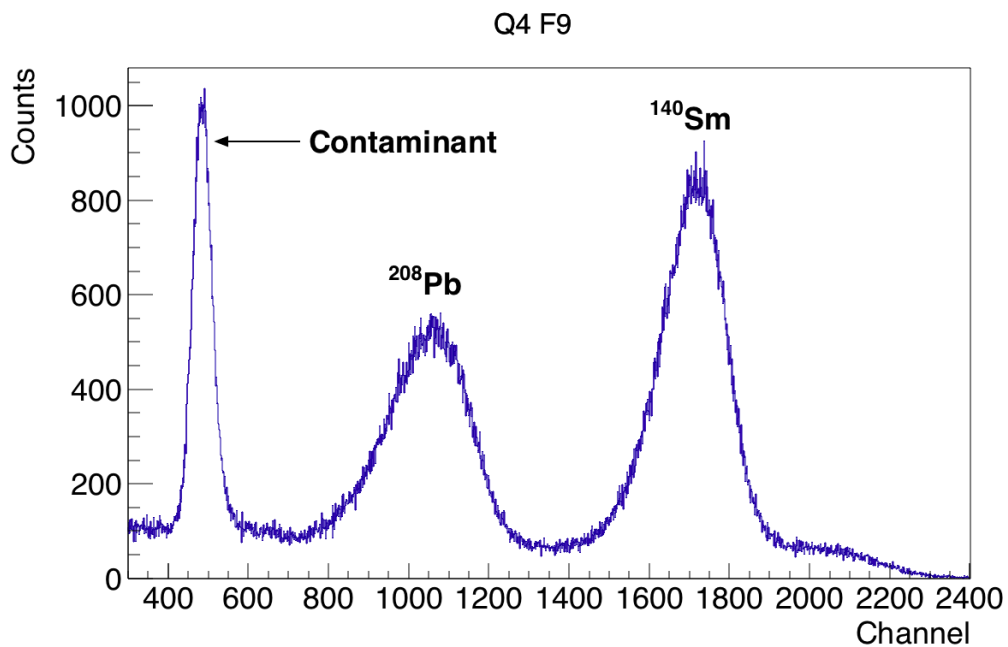
Ring number	Mid ring			$E_t$ [MeV]	$E_b$ [MeV]
	Distance from beam line [mm]	Angle [°]			
1	10	20.3		484.86	539.89
2	12	24.0		457.53	520.55
3	14	27.4		428.87	499.72
4	16	30.7		398.95	478.33
5	18	33.7		369.54	456.71
6	20	36.5		340.64	435.42
7	22	39.2		313.65	414.84
8	24	41.7		287.31	395.31
9	26	43.9		262.77	376.35
10	28	46.1		240.36	358.75
11	30	48.0		219.53	342.40
12	32	49.9		198.95	326.87
13	34	51.6		182.41	312.31
14	36	53.1		164.55	299.11
15	38	54.6		151.51	286.78
16	40	56.0		139.62	273.80

**Table 4.4:** CD debugging shows the number of strips fired at the front and back side of the CD.

CD debug ID	Strips fired	
	Front side	Back side
0	1	1
1	1	2
2	2	1
3	>1	>1
20	No particle found	

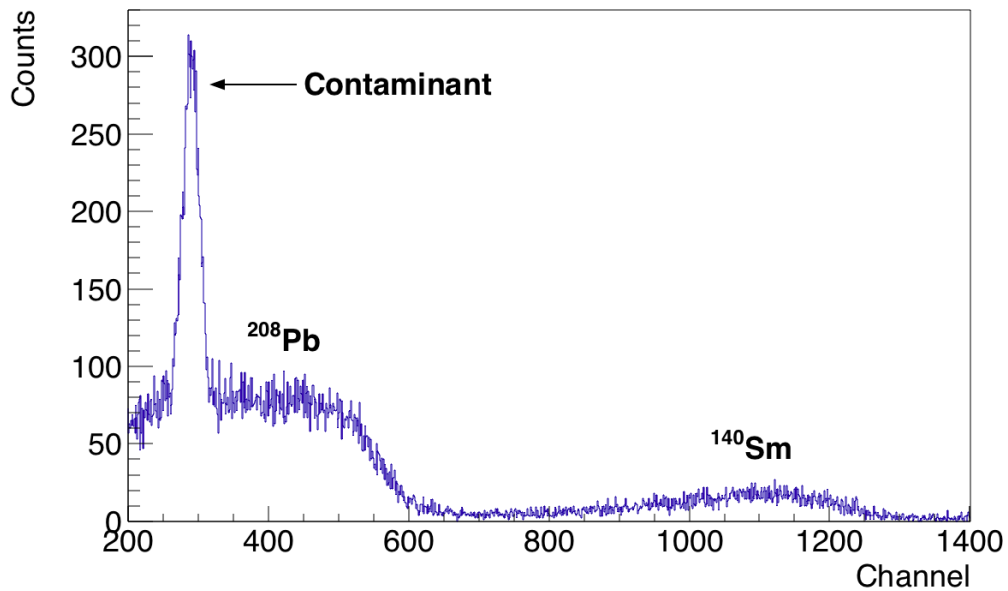
**Table 4.5:** DGF

Cluster	Detector	Segment	TreeBuilder
0	0	0	E_gam_seg_0_0_0



(a) Front strip 9 in quadrant 4.

bE Q1 F16 B12



(b) Back strip 12, gated on ring 16 (outermost ring) in quadrant 1.

**Figure 4.2:** Calibration of the CD is not always straightforward. The upper figure shows a front strip, where it is fairly easy to determine the centroids of the particles. The lower figure shows a back strip, where it is actually very difficult to determine where the centroid of  $^{208}\text{Pb}$  is.

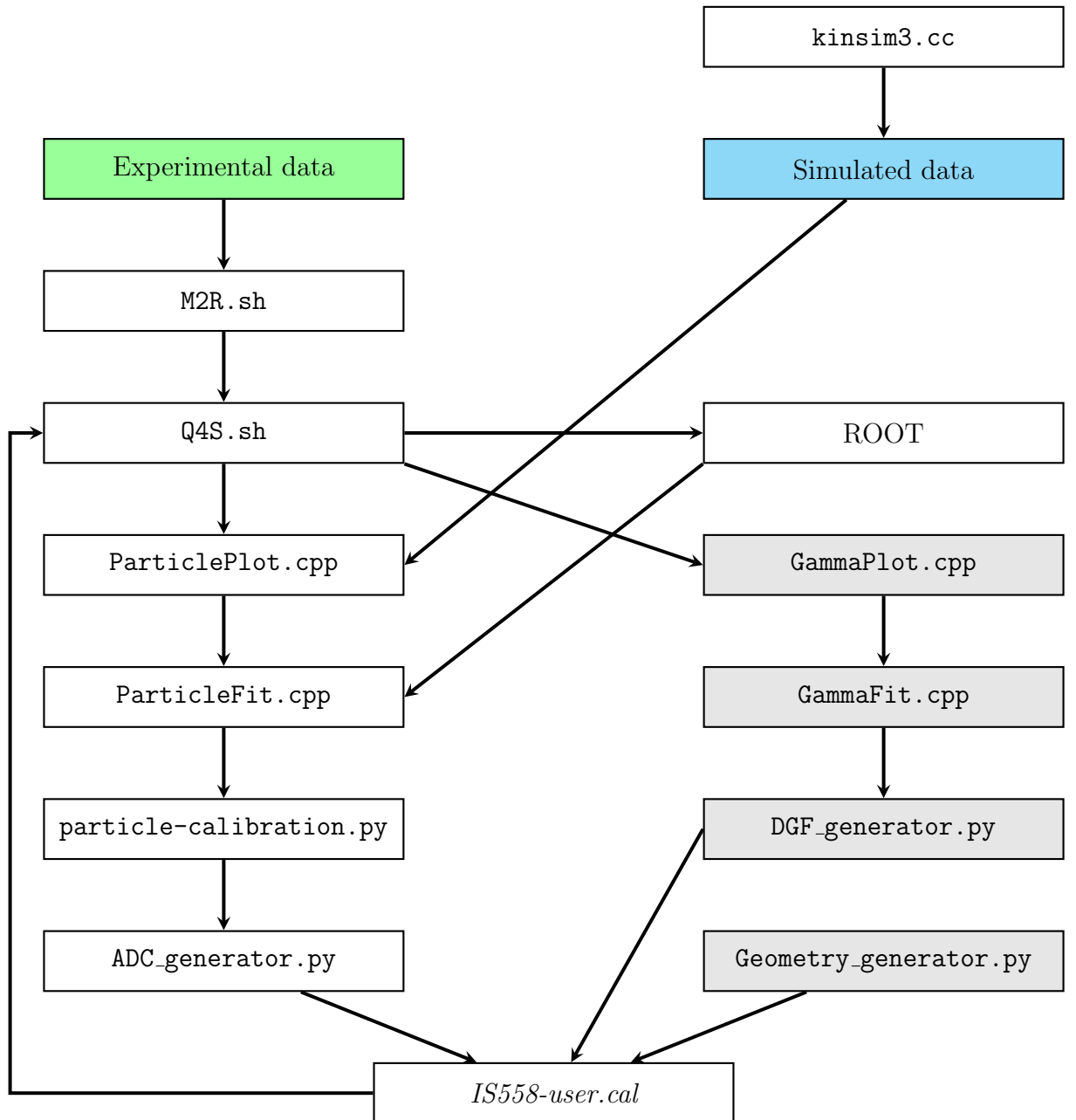
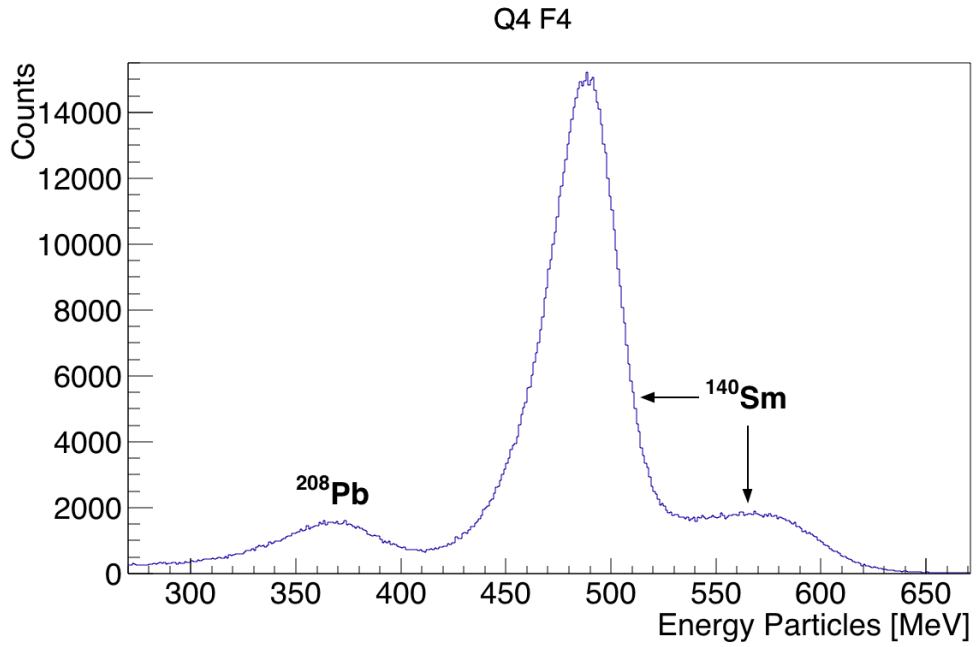
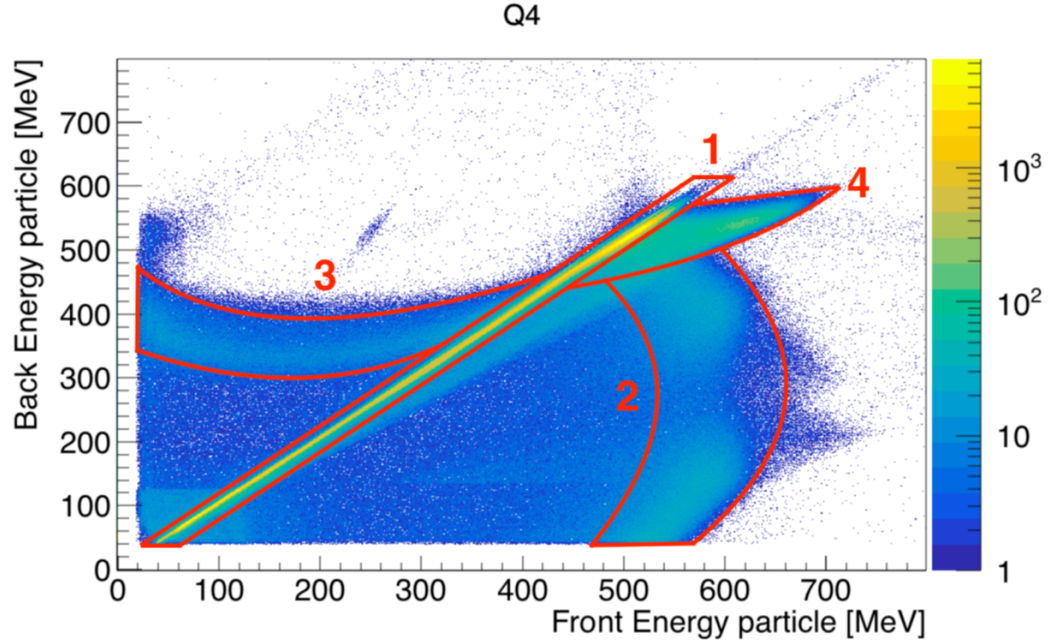


**Figure 4.3:** Flowchart of the programs, scripts and files used in the user calibration. The relative paths of these programs and scripts is shown in Table D.2.

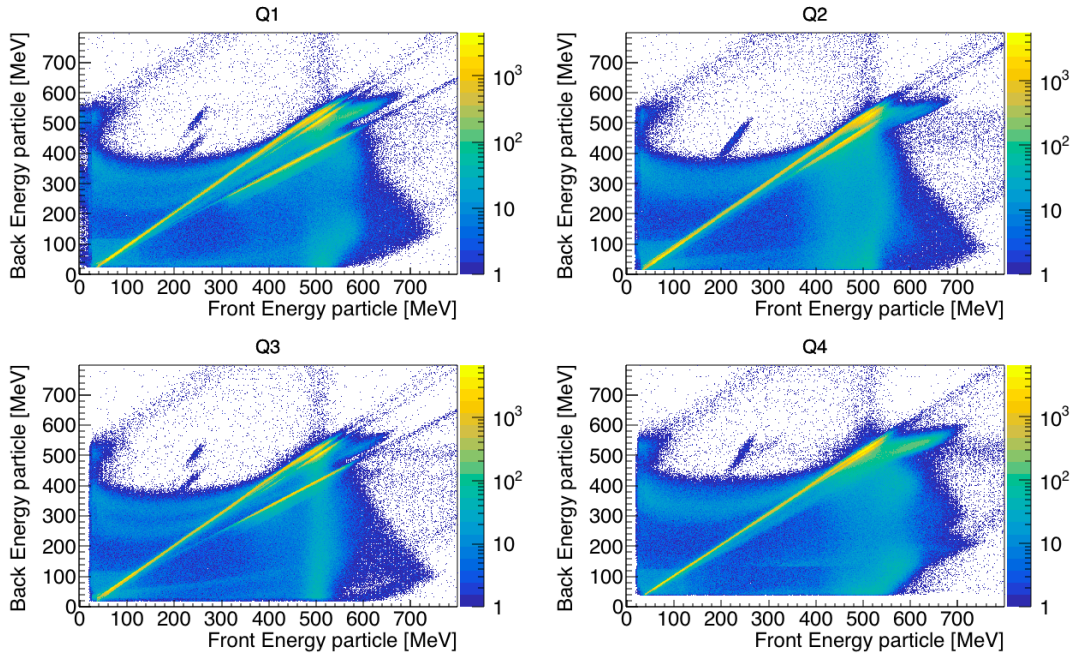


(a) Annular strip 4 in quadrant 4. At higher energies, there is a double-peak structure of  $^{140}\text{Sm}$ .

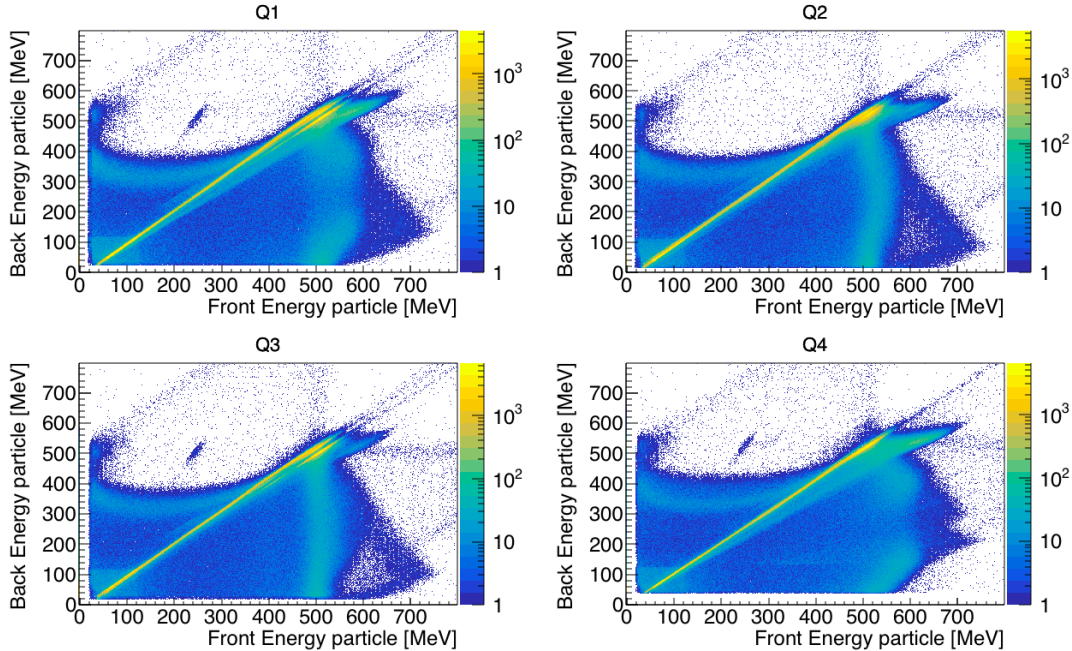


(b) Back energy vs. front energy for quadrant 4 of the CD. A similar figure to figures 39 and 40 in [37].

**Figure 4.4:** (a) The second peak of  $^{140}\text{Sm}$  can be explained by region 2 from (b). For more information, see text.

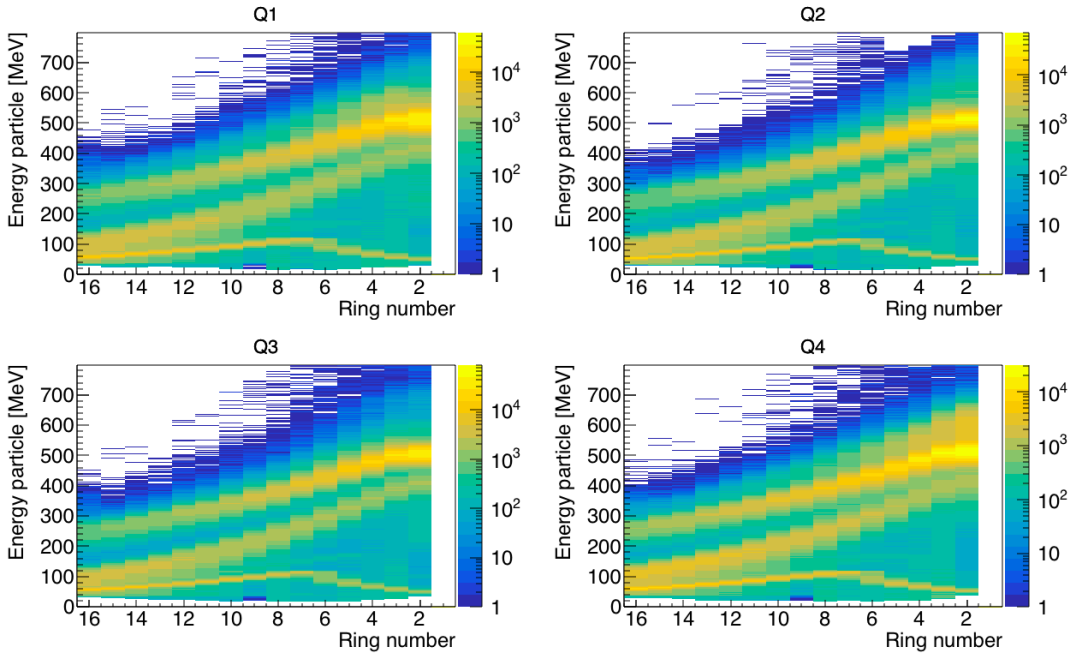


(a) Online calibration for the CD showing the four quadrants. It generally looks quite good, but there is a number of the secular strips (back side) that have the wrong gains.

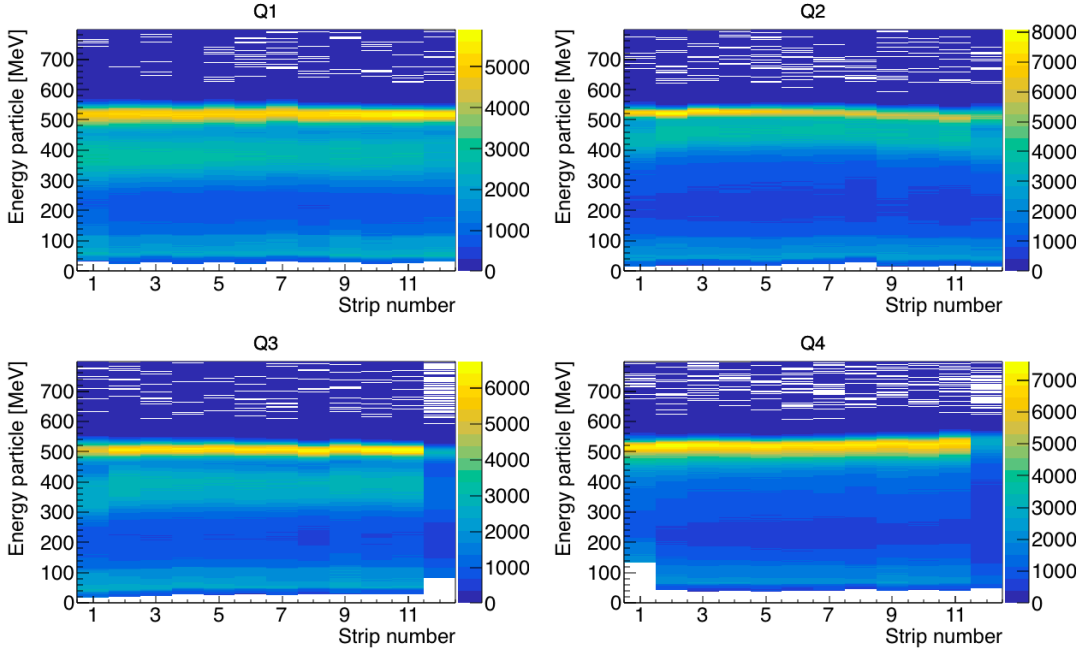


(b) User calibration for the CD showing the four quadrants. This is actually the online calibration without the innermost ring, which was broken.

**Figure 4.5:** Back energy vs. front energy for each quadrant of the CD.

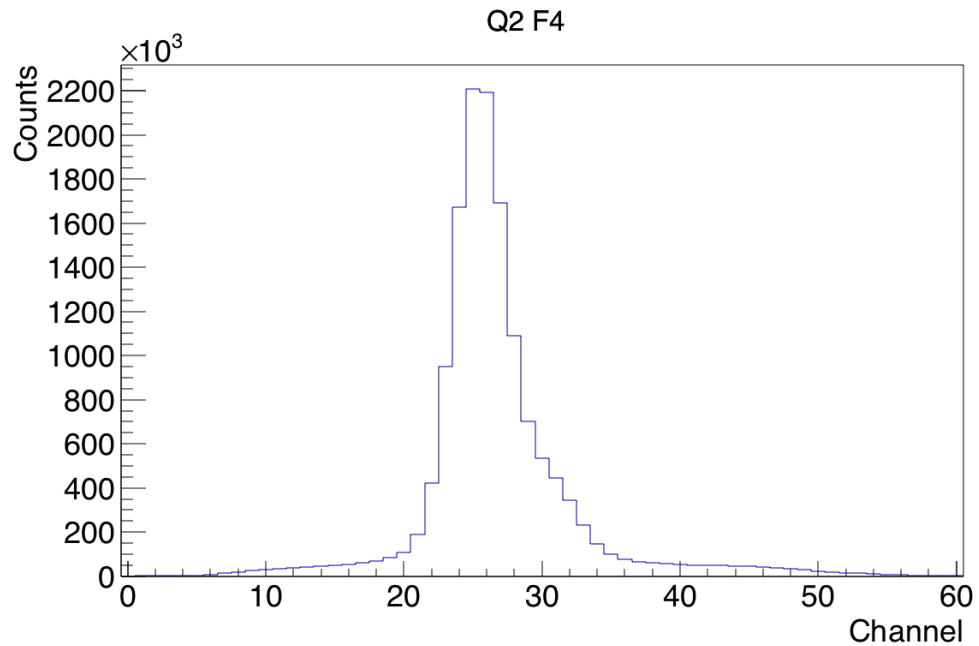


(a) CD front. Ring number 16 is the outermost ring and ring number 1 is the innermost ring.

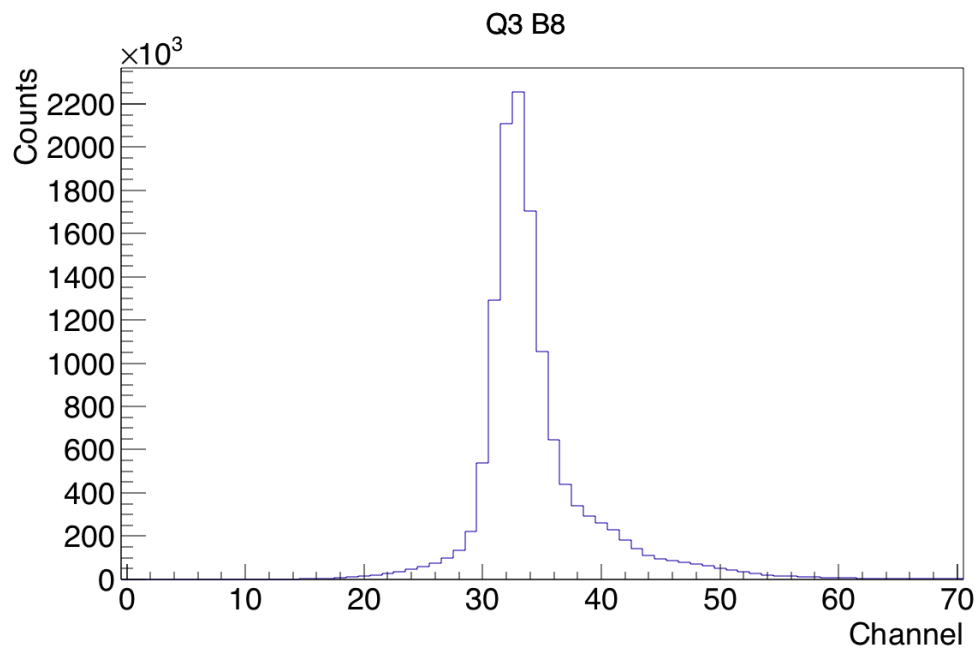


(b) CD back. A number of the secular strips have the wrong gains.

**Figure 4.6:** Energy vs. strip number for each quadrant of the CD.

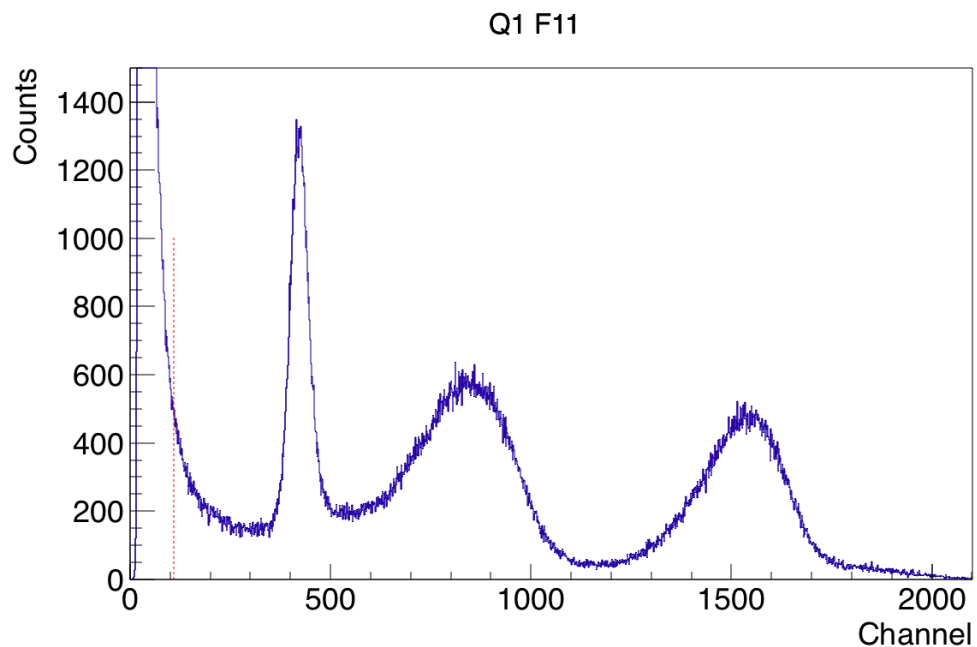


(a) Pedestal from annular strip 4 in quadrant 2.



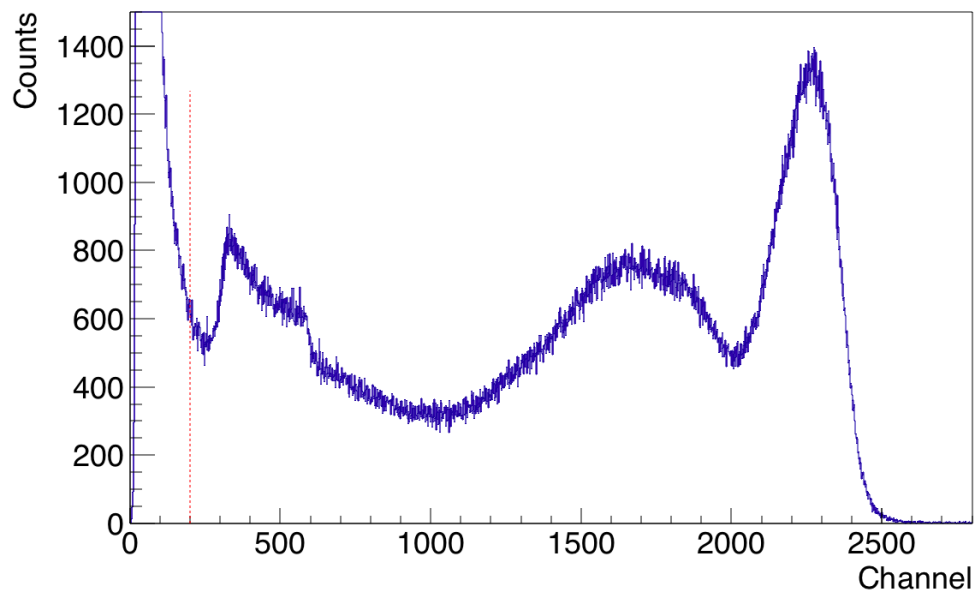
(b) Pedestal from secular strip 8 in quadrant 3.

**Figure 4.7:** The pedestal from charge sharing in the front and back side of the CD.



(a) Annular strip 11 in quadrant 1.

Q1 B6



(b) Secular strip 6 in quadrant 1.

**Figure 4.8:** The threshold, marked with a red dotted line, set for one front and one back strip of the CD.

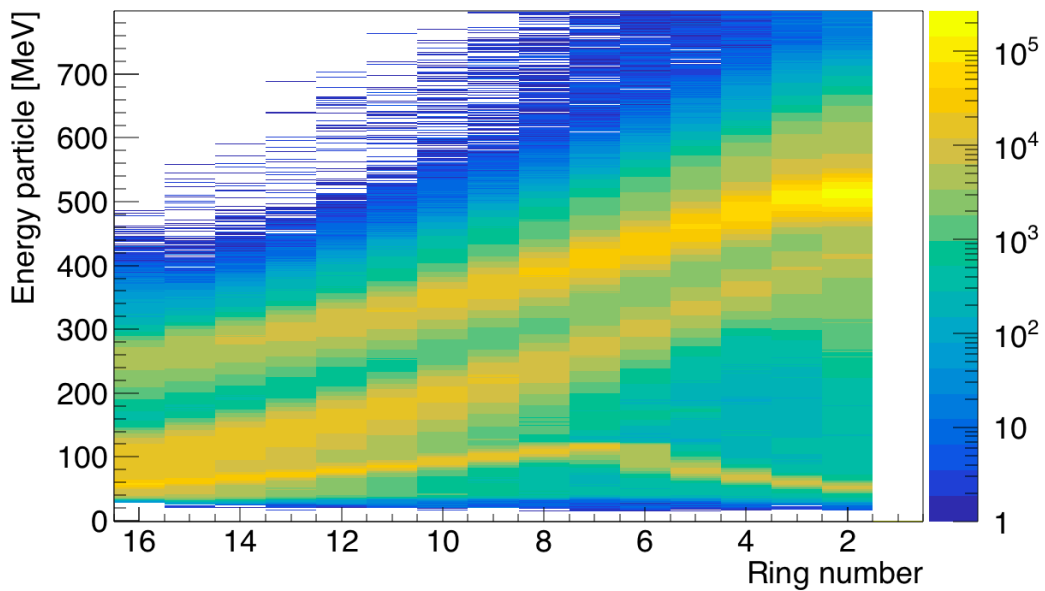


**Figure 4.9:** Energy vs. ring number all quadrants of the CD combined. The upper yellow curve is  $^{140}\text{Sm}$ , the middle one is  $^{208}\text{Pb}$  and the lower one is the contaminant. Ring 1, which is removed, is the innermost ring and ring 16 is the outermost ring.

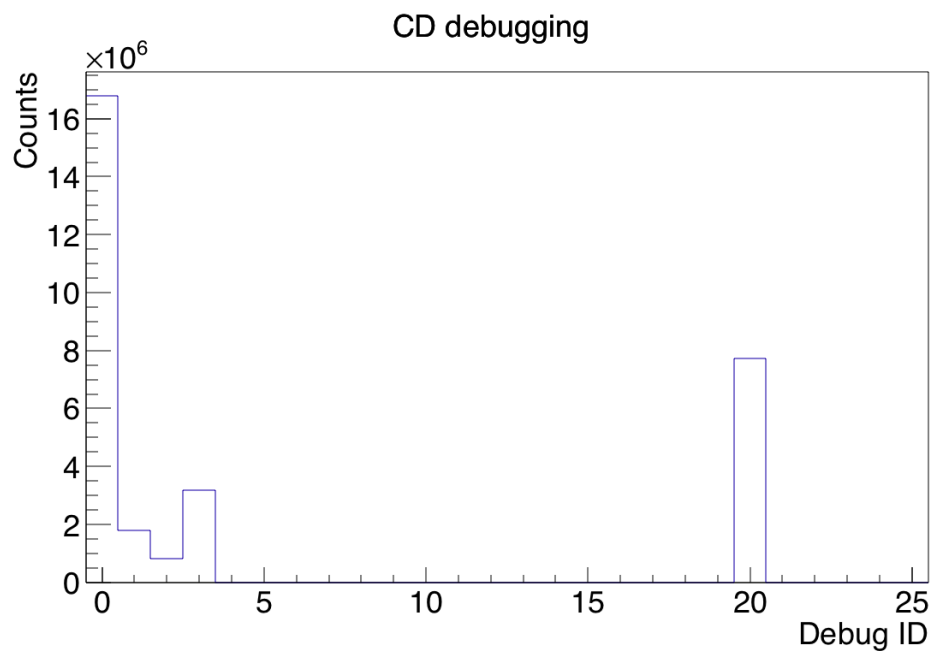


**Figure 4.10:** CD debugging. The debug IDs are explained by [Table 4.4](#).

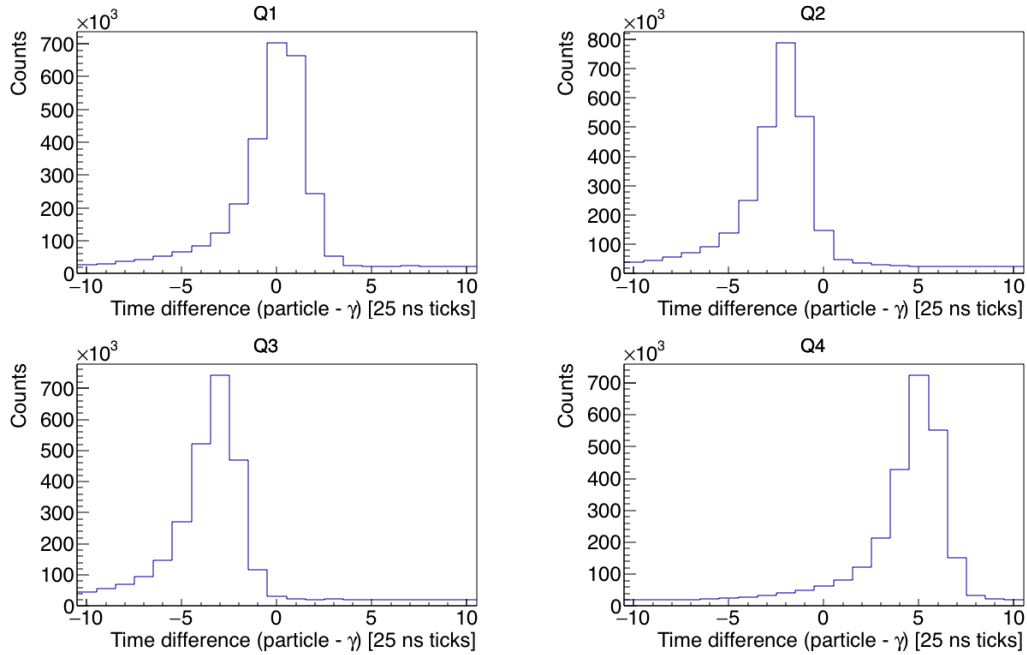


**Figure 4.11:** ADC time offsets for the four quadrants of the CD.

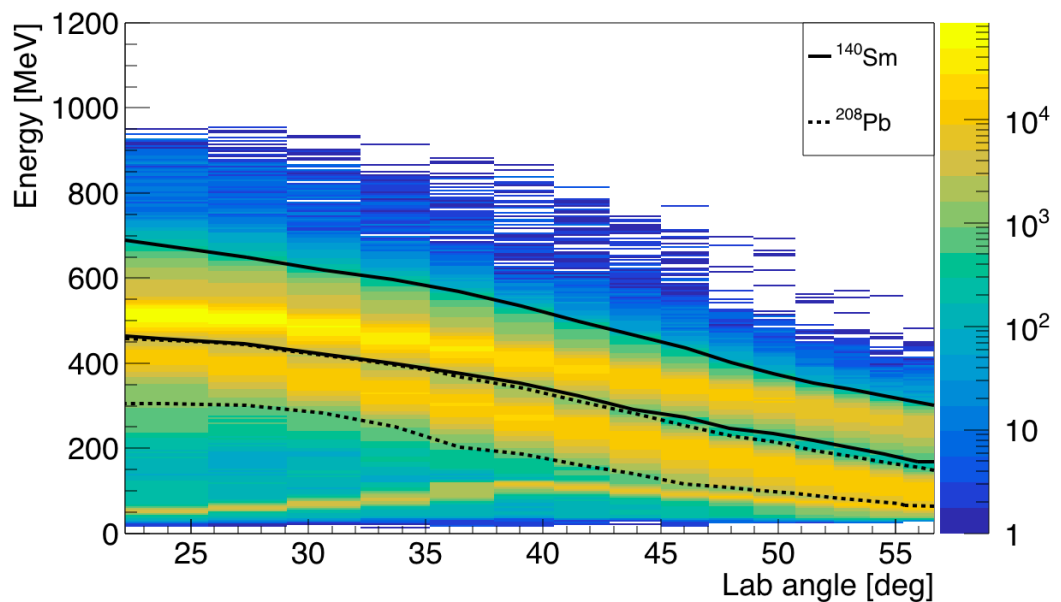


**Figure 4.12:** Detected particle events with cuts.

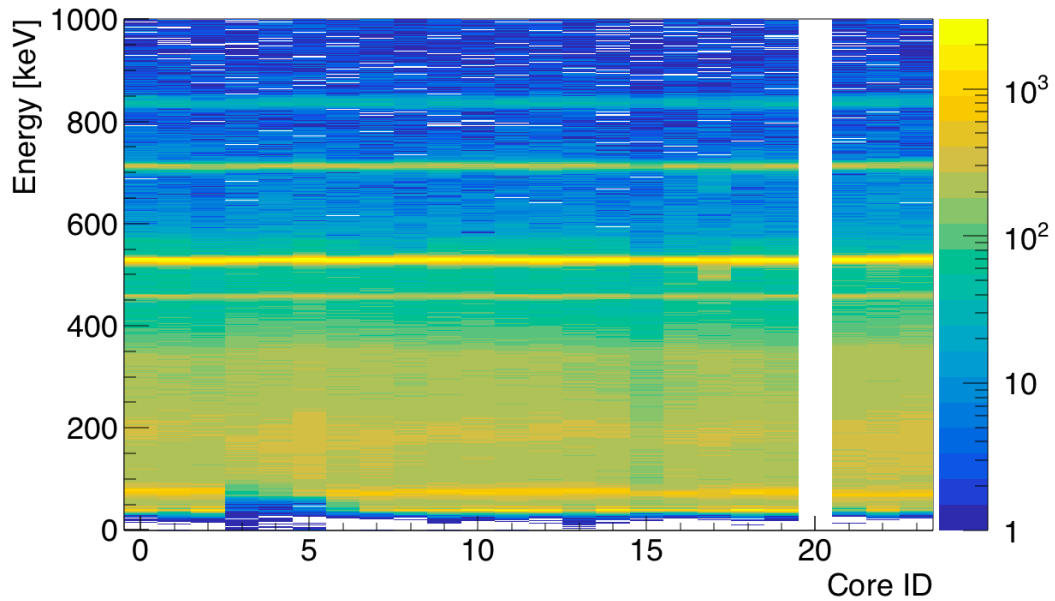


**Figure 4.13:** Beam gated prompt, Doppler corrected  $\gamma$ -rays. Core ID 20 is removed, see [Section 4.3.8](#).

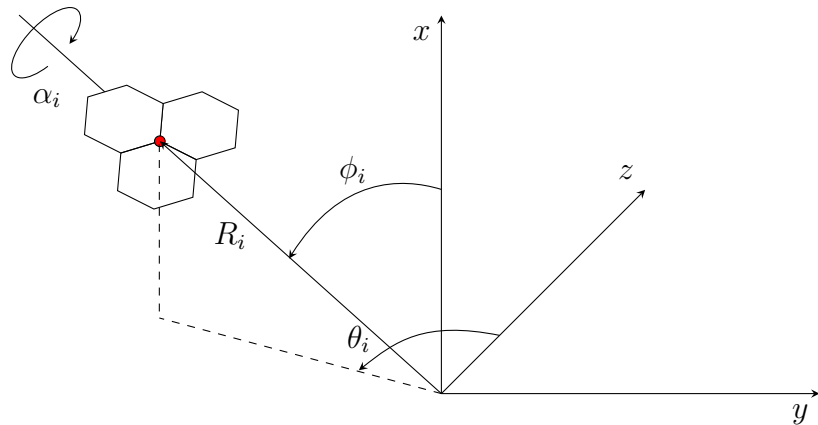
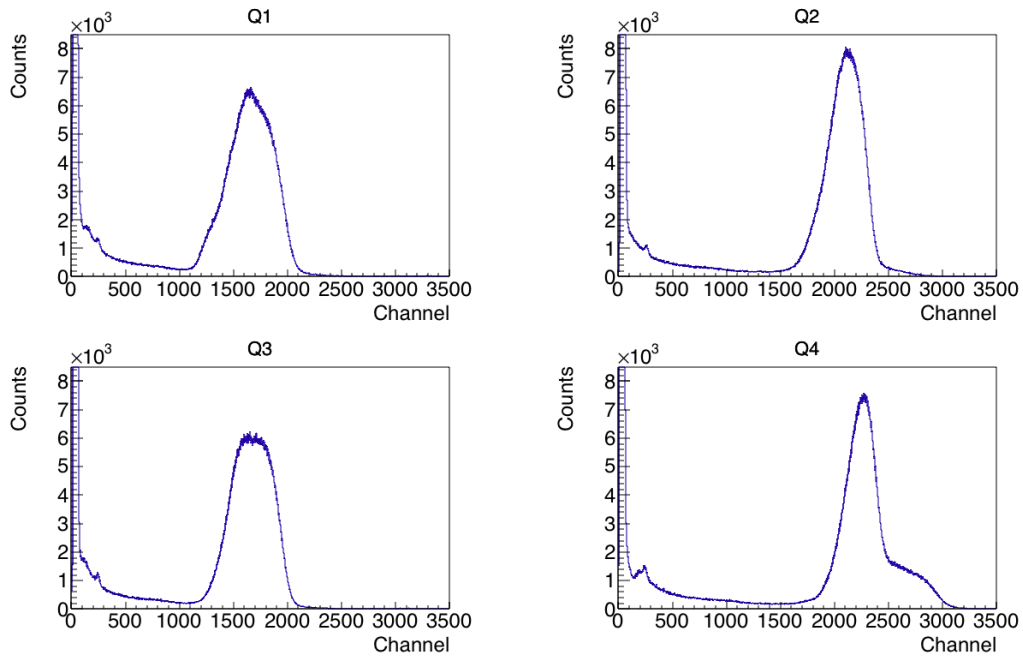


**Figure 4.14:** Miniball angles, where  $i$  denotes cluster number from [Table 4.6](#) and the  $z$ -axis is the beam direction. The angles,  $\theta$  and  $\phi$ , are defined from a right-hand polar coordinate system, while the angle  $\alpha$  determines the clockwise rotation around the center of the triple-cluster as seen from the target position [[37](#), [56](#)].

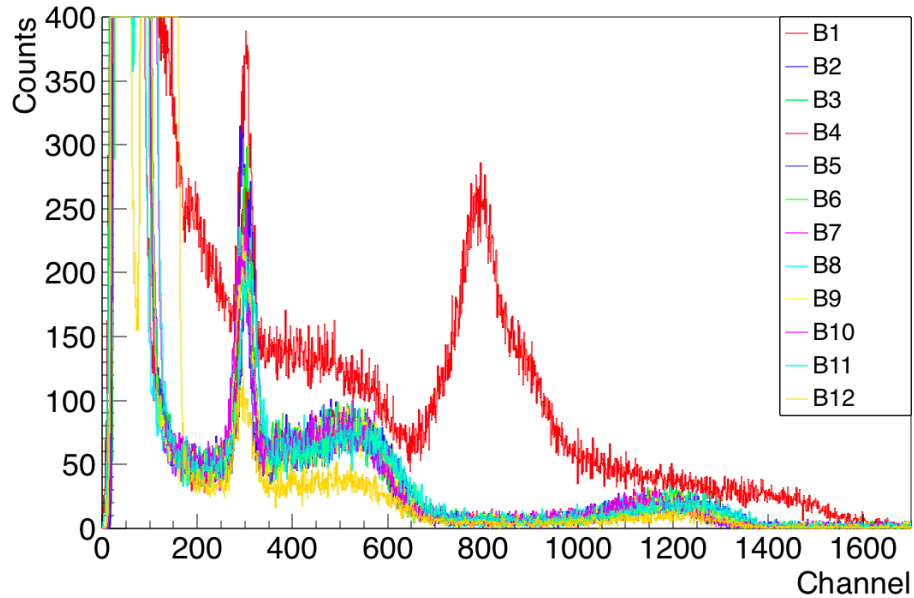
**Table 4.6:** Geometry to the center of the Miniball HPGe clusters (red dot in [Figure 4.14](#)) for the Doppler correction.

Cluster	$\theta_i$ [°]	$\phi_i$ [°]	$\alpha_i$ [°]	$R_i$ [mm]
0	311.16	126.67	129.79	107.08
1	51.08	62.74	51.83	100.59
2	309.02	126.87	51.23	105.76
3	251.90	57.44	130.31	105.40
4	296.93	235.53	128.74	106.48
5	233.45	239.09	46.67	105.18
6	59.42	308.67	131.04	127.04
7	130.56	309.09	46.46	110.18



(a) CD front ring 1 (innermost ring). It is impossible to separate  $^{208}\text{Pb}$  from  $^{140}\text{Sm}$ .

bE Q4 F16 B1-12



(b) CD back strip 1 gated on front ring 16 (outermost ring) in quadrant 4. B1 shows a lot more counts than the other strips around channel 800.

**Figure 4.15:** Broken detector segments in the CD.

# Chapter 5

## Experimental results and discussion

Very pure beam (did we have statistics of this?) - resultat til avhandling. sjekk etter doppler-korrigering. Nd-contaminasjon? i så fall veldig lite, 1-2 prosent?

Tilbakemelding:

we would have to look at the  $\gamma$ -spectra to identify any contaminants. There may be a little bit of Nd-140 in the beam, but if so, it is very little (judging from on-line spectra).

Level scheme (from Klintefjord?)

Tilbakemelding:

at some point you should show the level scheme.

- motivation: to explain what is known, and which transition probabilities you want to measure.

Perhaps also to explain what theory predicts.

- discussion: if you get  $\gamma$ -spectrum for  $^{140}\text{Sm} \rightarrow$  to explain what you see.

Figure 5.2 ...

Figure 5.3 ...

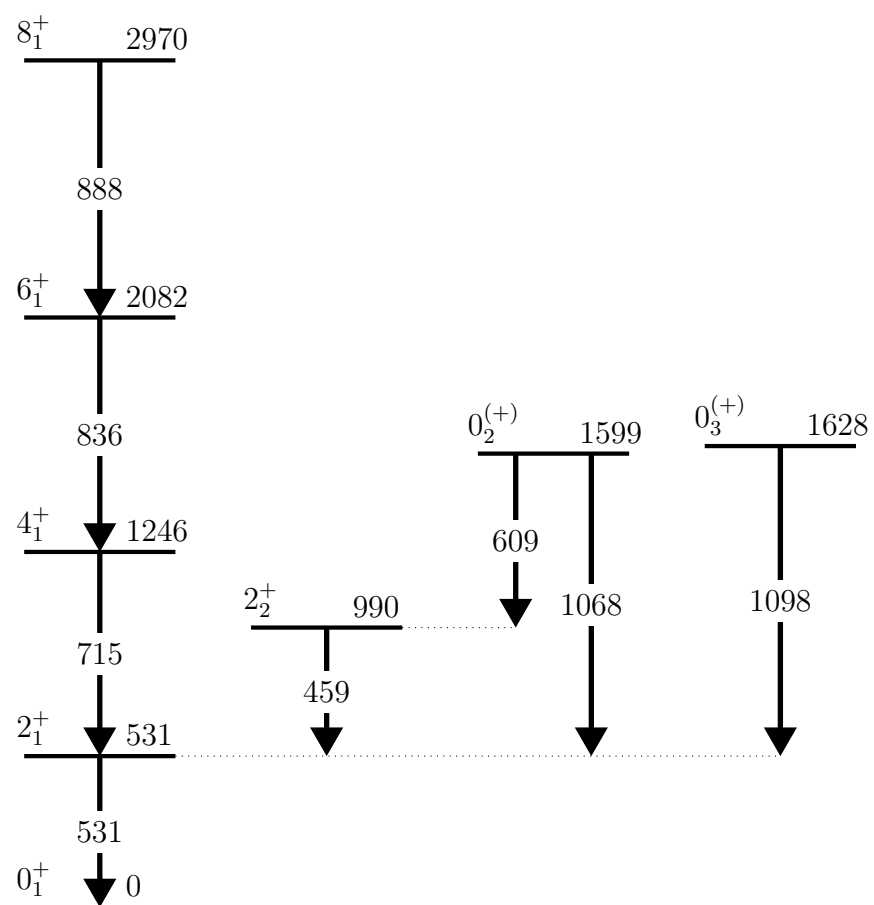
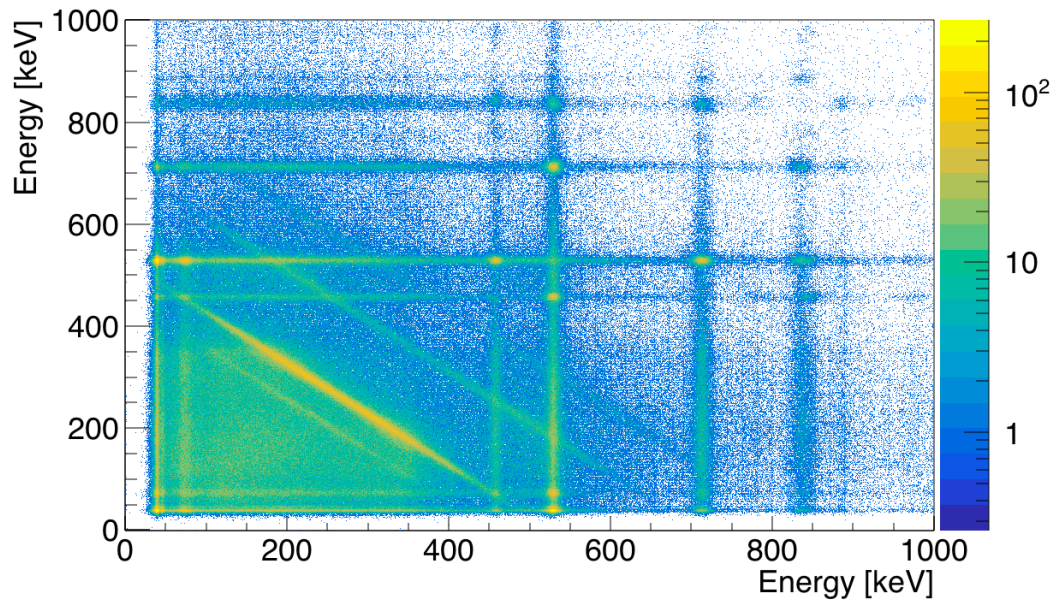
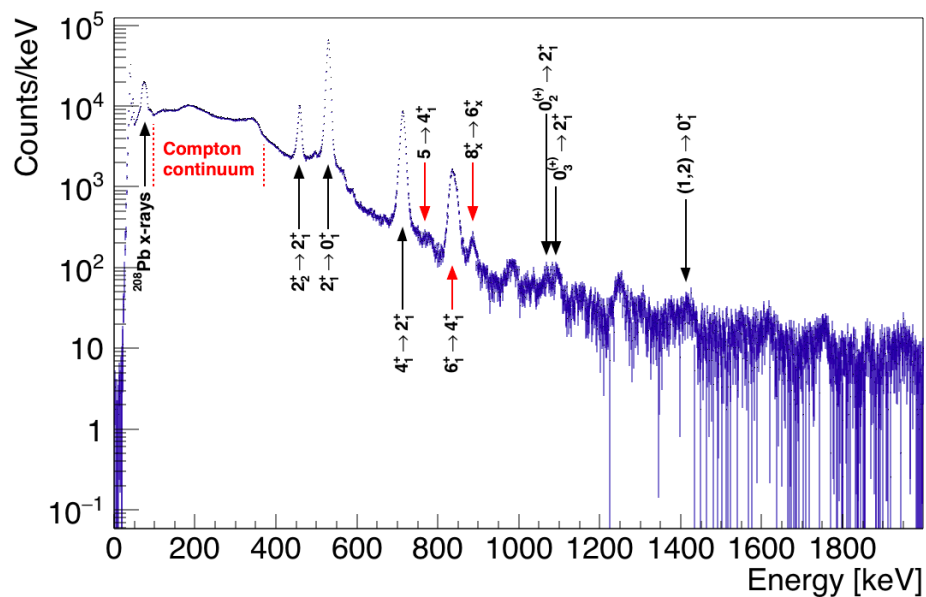


Figure 5.1: Level scheme for  $^{140}\text{Sm}$ .



**Figure 5.2:**  $\gamma$ - $\gamma$  matrix, Doppler corrected for beam.



**Figure 5.3:** Total statistics for  $\gamma$ -rays, background subtracted, Doppler corrected for scattered projectile.



# Chapter 6

## Summary and outlook

Future work: Better calibration of particle detectors and  $\gamma$ -detectors (online not perfect). Take into account the shape of the peaks  $\implies$  calibrate the particle detectors manually.. Takes a lot of time! But maybe less than trying to fit all in a script? If someone only knew and told this story...

Use a second opinion on the simulation, maybe try LISE++ or some other simulation program to get the centroids? Maybe `kinsim3` uses too much energy loss in CD? If you are using only the Pb and Sm for calibration, and then applying that calibration back to the data, then it should matter if the absolute energies are correct. This is an internal calibration, so that would simply mean that the peaks would have the wrong energy, but they should still be aligned on the front and back.

Geometry: For the geometry, I am not sure exactly what the best set of angles are. You should produce some spectra to analyse before determining this. In the output file of CLXAna you will find a histogram called `B_dcB_cid`, which is the Doppler corrected spectra vs. each detector. The peak energies should of course be constant as a function of detector number, if they vary, then the angles need to be improved.

In the Sm data, the issue came in determining the peak centroid or maximum for the experimental data. The peak shape is a convolution of many effects; intrinsic resolution of the detector, the beam energy width, straggling in the target, interaction points in the target, angular width of the detector strip, etc. While the simulation tries to include all these things, it was found that the peak shapes were not exactly the same. It might be worthwhile spending a bit of time to play with the parameters and try to get the peak shape as similar as possible. At that point, maybe use a certain feature of the peak, such as the maximum, or the highest energy edge. Or, honestly, it might be better to simply hover the mouse over the correct "feature" of the peak and position it by eye, be it the centroid or the maximum. Then the same feature in the corresponding simulated

spectrum can be analyzed. The maximum of the peak on the high energy side is not the center of the peak, but roughly equivalent to the maximum. It can be imagined as fitting a Gaussian to the right-hand side, the high-energy side only, as this would be roughly where the centroid is.

Efficiency calibration ++

**Fra oppgaveteksten:**

determine Coulomb excitation yields. These yields will then, in a second step, be compared to theoretical calculations and transition probabilities and quadrupole moments will be extracted using chi-square minimization procedures.

GOSIA and GOSIA2 analysis?

[https://www.pas.rochester.edu/~cline/Gosia/Gosia\\_Manual\\_20110609.pdf](https://www.pas.rochester.edu/~cline/Gosia/Gosia_Manual_20110609.pdf)

# Appendices



## **Appendix A**

### **Acronyms and abbreviations**

---

ADC	Analog to Digital Converter
bash	Bourne-Again SHell
CERN	European Council for Nuclear Research (in French: Conseil Européen pour la Recherche Nucléaire)
COULEX	COULomb EXcitation
CM frame	Center of Mass frame
DAQ	Data AcQuisition
DGF	Digital Gamma Finder
DSSSD	Double Sided Silicon Strip Detector (also known as CD)
CD	Compact Disc (also see DSSSD)
GPS	General Purpose Separator
HRS	High Resolution Separator
HIE-ISOLDE	High Intensity and Energy upgrade at ISOLDE
HPGe	High Purity Germanium
ISOL	Isotope Separator On Line
ISOLDE	ISOL DEvice
LAB frame	LABoRatory frame
LINAC	LINear ACcelerator
MBS	Multi Branch System
MED	MBS Event Data (also known as Miniball Event Data)
MAR <sub>a</sub> BQ <sub>U</sub>	MBS And ROOT Based Online/Offline Utility
PHD	Pulse-Height Defect
PSB	Proton Synchrotron Booster
RF	Radio Frequency
REX	Radioactive beam EXperiment
EBIS	Electron Beam Ion Source
REXEgis	Radioactive beam EXperiment Electron Beam Ion Source
REXTRAP	Radioactive beam EXperiment TRAP
REX-ISOLDE	Radioactive beam EXperiment at ISOLDE
RIB	Radioactive Ion Beam
RILIS	Resonance Ionization Laser Ion Source
SRIM	Stopping and Range of Ions in Matter
TDC	Time to Digital Converter

---

# Appendix B

## Symbol list

**Table B.1:** Table of symbols with explanations.

$T_{1/2}$	Half-life
-----------	-----------



# Appendix C

## Two-particle collision

### C.1 Laboratory (LAB) frame of reference

The angles of the two-particle collision in the laboratory frame from [Figure 2.1a](#) is calculated in this section. A general approach is used to make it easier to hold track of the parameters. From the figure we can express the velocities as

$$\begin{aligned}\mathbf{u} &= \mathbf{u}_1 = u\hat{\mathbf{x}} \\ \mathbf{u}_2 &= 0 \\ \mathbf{v}_b &= \mathbf{v}_1 = v_1(\cos\theta\hat{\mathbf{x}} + \sin\theta\hat{\mathbf{y}}) \\ \mathbf{v}_t &= \mathbf{v}_2 = v_2(\cos\varphi\hat{\mathbf{x}} - \sin\varphi\hat{\mathbf{y}})\end{aligned}\tag{C.1}$$

where  $\mathbf{u}_1$  and  $\mathbf{v}_1$  is the initial and final velocity of the projectile  $m_b = m_1$  respectively, and  $\mathbf{u}_2$  and  $\mathbf{v}_2$  is the initial and final velocity of the target  $m_t = m_2$  respectively. The angles  $\theta_b = \theta$  and  $\theta_t = \varphi$  are the projectile and target angle respectively. We also introduce a ratio of the projectile mass to the target mass,  $\alpha = m_1/m_2$ .

Conservation of momentum gives

$$m_1\mathbf{u}_1 = m_1\mathbf{v}_1 + m_2\mathbf{v}_2$$

which in x-direction can be expressed as

$$\begin{aligned}m_1u &= m_1v_1 \cos\theta + m_2v_2 \cos\varphi \\ m_1(u - v_1 \cos\theta) &= m_2v_2 \cos\varphi \\ \frac{m_1}{m_2}(u - v_1 \cos\theta) &= v_2 \cos\varphi \\ \alpha(u - v_1 \cos\theta) &= v_2 \cos\varphi\end{aligned}\tag{C.2}$$

and in y-direction can be expressed as

$$\begin{aligned} 0 &= m_1 v_1 \sin \theta - m_2 v_2 \sin \varphi \\ m_1 v_1 \sin \theta &= m_2 v_2 \sin \varphi \\ \frac{m_1}{m_2} v_1 \sin \theta &= v_2 \sin \varphi \\ \alpha v_1 \sin \theta &= v_2 \sin \varphi \end{aligned} \quad (\text{C.3})$$

Conservation of energy gives

$$\begin{aligned} \frac{1}{2} m_1 \mathbf{u}_1^2 &= \frac{1}{2} m_1 \mathbf{v}_1^2 + \frac{1}{2} m_2 \mathbf{v}_2^2 \\ \frac{1}{2} m_1 (u^2 - v_1^2) &= \frac{1}{2} m_2 v_2^2 \\ \frac{m_1}{m_2} (u^2 - v_1^2) &= v_2^2 \\ \alpha (u^2 - v_1^2) &= v_2^2 \end{aligned} \quad (\text{C.4})$$

We now have three equations (Equation (C.2) - Equation (C.4)) with four unknown quantities ( $v_1, \theta, v_2, \varphi$ ). Using the target angle  $\varphi$  as an independent variable, we can find expressions for the other three variables.

Squaring Equation (C.2)

$$\begin{aligned} \alpha^2 (u - v_1 \cos \theta)^2 &= v_2^2 \cos^2 \varphi \\ \alpha^2 (u^2 - 2uv_1 \cos \theta + v_1^2 \cos^2 \theta) &= v_2^2 \cos^2 \varphi \end{aligned}$$

and Equation (C.3)

$$\alpha^2 v_1^2 \sin^2 \theta = v_2^2 \sin^2 \varphi$$

and adding them together gives

$$\begin{aligned} \alpha^2 (u^2 - 2uv_1 \cos \theta + v_1^2 \cos^2 \theta + v_1^2 \sin^2 \theta) &= v_2^2 (\cos^2 \varphi + \sin^2 \varphi) \\ \alpha^2 (u^2 - 2uv_1 \cos \theta + v_1^2) &= v_2^2 \\ \alpha^2 u^2 - 2\alpha^2 uv_1 \cos \theta + \alpha^2 v_1^2 &= v_2^2 \\ \alpha^2 v_1^2 &= -\alpha^2 u^2 + 2\alpha^2 uv_1 \cos \theta + v_2^2 \\ \alpha^2 v_1^2 &= -\alpha^2 u^2 + 2\alpha u (\alpha v_1 \cos \theta) + v_2^2 \end{aligned} \quad (\text{C.5})$$

From Equation (C.2) we have

$$\begin{aligned} \alpha(u - v_1 \cos \theta) &= v_2 \cos \varphi \\ \alpha u - \alpha v_1 \cos \theta &= v_2 \cos \varphi \\ \alpha v_1 \cos \theta &= \alpha u - v_2 \cos \varphi \end{aligned} \quad (\text{C.6})$$

Substituting for [Equation \(C.6\)](#) into [Equation \(C.5\)](#) we get

$$\begin{aligned}\alpha^2 v_1^2 &= -\alpha^2 u^2 + 2\alpha u(\alpha u - v_2 \cos \varphi) + v_2^2 \\ \alpha^2 v_1^2 &= -\alpha^2 u^2 + 2\alpha^2 u^2 - 2\alpha u v_2 \cos \varphi + v_2^2 \\ \alpha^2 v_1^2 &= \alpha^2 u^2 - 2\alpha u v_2 \cos \varphi + v_2^2\end{aligned}\quad (\text{C.7})$$

Using [Equation \(C.4\)](#) we get

$$\begin{aligned}\left(\frac{\alpha}{\alpha}\right) \alpha(u^2 - v_1^2) &= v_2^2 \\ \alpha^2(u^2 - v_1^2) &= \alpha v_2^2 \\ \alpha^2 u^2 - \alpha^2 v_1^2 &= \alpha v_2^2 \\ \alpha^2 v_1^2 &= \alpha^2 u^2 - \alpha v_2^2\end{aligned}\quad (\text{C.8})$$

Combining [Equation \(C.7\)](#) and [Equation \(C.8\)](#) gives

$$\begin{aligned}\alpha^2 u^2 - 2\alpha u v_2 \cos \varphi + v_2^2 &= \alpha^2 u^2 - \alpha v_2^2 \\ v_2^2 + \alpha v_2^2 &= 2\alpha u v_2 \cos \varphi \\ v_2^2(1 + \alpha) &= 2\alpha u v_2 \cos \varphi \\ v_2 &= 2 \left( \frac{\alpha}{1 + \alpha} \right) u \cos \varphi\end{aligned}\quad (\text{C.9})$$

Substituting [Equation \(C.9\)](#) into [Equation \(C.8\)](#) we get

$$\begin{aligned}\alpha^2 v_1^2 &= \alpha^2 u^2 - \alpha \left( 2 \left( \frac{\alpha}{1 + \alpha} \right) u \cos \varphi \right)^2 \\ v_1^2 &= u^2 - \frac{1}{\alpha} \left( 4 \left( \frac{\alpha^2}{(1 + \alpha)^2} \right) u^2 \cos^2 \varphi \right) \\ v_1^2 &= u^2 \left( 1 - 4 \left( \frac{\alpha}{(1 + \alpha)^2} \right) \cos^2 \varphi \right) \\ v_1 &= u \sqrt{1 - 4 \frac{\alpha}{M} \cos^2 \varphi}\end{aligned}\quad (\text{C.10})$$

where  $\alpha/M = \alpha/(1 + \alpha)^2$ . The ratio of [Equation \(C.3\)](#) and [Equation \(C.6\)](#) gives

$$\begin{aligned}\frac{\alpha v_1 \sin \theta}{\alpha v_1 \cos \theta} &= \frac{v_2 \sin \varphi}{\alpha u - v_2 \cos \varphi} \\ \tan \theta &= \frac{v_2 \sin \varphi}{\alpha u - v_2 \cos \varphi}\end{aligned}\quad (\text{C.11})$$

Inserting Equation (C.9) into Equation (C.11) gives

$$\begin{aligned}
 \tan \theta &= \frac{\left(2\left(\frac{\alpha}{1+\alpha}\right) u \cos \varphi\right) \sin \varphi}{\alpha u - \left(2\left(\frac{\alpha}{1+\alpha}\right) u \cos \varphi\right) \cos \varphi} \\
 \tan \theta &= \frac{\alpha u \left(\frac{1}{1+\alpha}\right) 2 \sin \varphi \cos \varphi}{\alpha u \left(1 - 2\left(\frac{1}{1+\alpha}\right) \cos^2 \varphi\right)} \\
 \tan \theta &= \frac{\sin 2\varphi}{\left(1 + \alpha\right) \left(1 - 2\left(\frac{1}{1+\alpha}\right) \cos^2 \varphi\right)} \\
 \tan \theta &= \frac{\sin 2\varphi}{1 + \alpha - 2 \cos^2 \varphi} \\
 \tan \theta &= \frac{\sin 2\varphi}{\alpha - (2 \cos^2 \varphi - 1)} \\
 \tan \theta &= \frac{\sin 2\varphi}{\alpha - \cos 2\varphi} \\
 \theta &= \arctan \left( \frac{\sin 2\varphi}{\alpha - \cos 2\varphi} \right)
 \end{aligned} \tag{C.12}$$

Substituting back the variable names from Figure 2.1a into Equation (C.12) gives

$$\theta_b = \arctan \left( \frac{\sin 2\theta_t}{\alpha - \cos 2\theta_t} \right) \tag{C.13}$$

## C.2 Center of mass (CM) frame of reference

Using the same approach as section C.1. From figure Figure 2.1b we can express the velocities as

$$\begin{aligned}
 \mathbf{u}'_1 &= u'_1 \hat{\mathbf{x}} \\
 \mathbf{u}'_2 &= u'_2 \hat{\mathbf{x}} \\
 \mathbf{v}'_b &= \mathbf{v}'_1 = v'_1 (\cos \theta' \hat{\mathbf{x}} + \sin \theta' \hat{\mathbf{y}}) \\
 \mathbf{v}'_t &= \mathbf{v}'_2 = v'_2 (-\cos \theta' \hat{\mathbf{x}} - \sin \theta' \hat{\mathbf{y}}) = -v'_2 (\cos \theta' \hat{\mathbf{x}} + \sin \theta' \hat{\mathbf{y}})
 \end{aligned} \tag{C.14}$$

where  $\mathbf{u}'_1$  and  $\mathbf{v}'_1$  is the initial and final velocity of the projectile  $m_b = m_1$  respectively, and  $\mathbf{u}'_2$  and  $\mathbf{v}'_2$  is the initial and final velocity of the target  $m_t = m_2$  respectively. The angle  $\theta'_b = \theta'$  is the projectile angle.

In the center of mass (CM) frame of reference, the position of the center of mass is given by

$$\mathbf{R} = \frac{m_1 \mathbf{r}_1 + m_2 \mathbf{r}_2}{m_1 + m_2} \tag{C.15}$$

and the velocity is

$$\mathbf{V} = \frac{d\mathbf{R}}{dt} = \frac{d}{dt} \left( \frac{m_1 \mathbf{r}_1 + m_2 \mathbf{r}_2}{m_1 + m_2} \right) = \frac{m_1 \mathbf{u}'_1 + m_2 \mathbf{u}'_2}{m_1 + m_2} \quad (\text{C.16})$$

At the origin of the CM frame,  $\mathbf{R} = 0$ , which implies  $\mathbf{V} = 0$ . The total momentum before the collision is

$$\begin{aligned} m_1 \mathbf{u}'_1 + m_2 \mathbf{u}'_2 &= 0 \\ m_2 \mathbf{u}'_2 &= -m_1 \mathbf{u}'_1 \\ \mathbf{u}'_2 &= -\frac{m_1}{m_2} \mathbf{u}'_1 \\ \mathbf{u}'_2 &= -\alpha \mathbf{u}'_1 \end{aligned} \quad (\text{C.17})$$

and after the collision it is

$$\begin{aligned} m_1 \mathbf{v}'_1 + m_2 \mathbf{v}'_2 &= 0 \\ m_2 \mathbf{v}'_2 &= -m_1 \mathbf{v}'_1 \\ \mathbf{v}'_2 &= -\frac{m_1}{m_2} \mathbf{v}'_1 \\ \mathbf{v}'_2 &= -\alpha \mathbf{v}'_1 \\ -v'_2 (\cos \theta' \hat{\mathbf{x}} + \sin \theta' \hat{\mathbf{y}}) &= -\alpha v'_1 (\cos \theta' \hat{\mathbf{x}} + \sin \theta' \hat{\mathbf{y}}) \\ v'_2 &= \alpha v'_1 \end{aligned} \quad (\text{C.18})$$

Conservation of energy gives

$$\begin{aligned} \frac{1}{2} m_1 u'^2_1 + \frac{1}{2} m_2 u'^2_2 &= \frac{1}{2} m_1 v'^2_1 + \frac{1}{2} m_2 v'^2_2 \\ m_1 u'^2_1 + m_2 u'^2_2 &= m_1 v'^2_1 + m_2 v'^2_2 \end{aligned} \quad (\text{C.19})$$

Substituting Equation (C.17) and Equation (C.18) into Equation (C.19) gives

$$\begin{aligned} m_1 u'^2_1 + m_2 (-\alpha u'_1)^2 &= m_1 v'^2_1 + m_2 (\alpha v'_1)^2 \\ m_1 u'^2_1 + \alpha^2 m_2 u'^2_1 &= m_1 v'^2_1 + \alpha^2 m_2 v'^2_1 \\ (m_1 + \alpha^2 m_2) u'^2_1 &= (m_1 + \alpha^2 m_2) v'^2_1 \\ u'^2_1 &= v'^2_1 \\ u'_1 &= v'_1 \end{aligned} \quad (\text{C.20})$$

Substituting Equation (C.20) into Equation (C.17) gives

$$u'_2 = -\alpha v'_1 \quad (\text{C.21})$$

### C.3 Connection between the LAB frame and the CM frame

Galilean transformations describes the relationship between the LAB frame and the CM frame

$$\begin{aligned} x' &= x - vt & v'_x &= v_x - V_{cm} \\ y' &= y & v'_y &= v_y \\ z' &= z & v'_z &= v_z \\ t' &= t \end{aligned}$$

Using the same approach as section C.1. In the LAB frame Figure 2.1a, conservation of momentum is given by

$$m_1 \mathbf{u}_1 + m_2 \mathbf{u}_2 = m_1 \mathbf{v}_1 + m_2 \mathbf{v}_2 = (m_1 + m_2) \mathbf{V} \quad (\text{C.22})$$

which can be written as

$$\begin{aligned} m_1 \mathbf{u}_1 + m_2 \mathbf{u}_2 &= (m_1 + m_2) \mathbf{V} \\ \mathbf{V} &= \frac{m_1 \mathbf{u}_1 + m_2 \mathbf{u}_2}{m_1 + m_2} & \mathbf{u}_2 &= 0 \\ \mathbf{V} &= \frac{m_1}{m_1 + m_2} \mathbf{u}_1 \\ \mathbf{V} &= \frac{\alpha}{1 + \alpha} u \hat{\mathbf{x}} \\ V &= \frac{\alpha}{1 + \alpha} u \end{aligned} \quad (\text{C.23})$$

Using Galilean transformations, the connection between  $\mathbf{v}'_1$  and  $\mathbf{v}_1$  is expressed as

$$\begin{aligned} \mathbf{v}'_1 &= \mathbf{v}_1 - \mathbf{V} \\ \mathbf{v}_1 &= \mathbf{v}'_1 + \mathbf{V} \end{aligned} \quad (\text{C.24})$$

which in x-direction gives

$$v_1 \cos \theta = v'_1 \cos \theta' + V \quad (\text{C.25})$$

and in y-direction gives

$$v_1 \sin \theta = v'_1 \sin \theta' \quad (\text{C.26})$$

The ratio of [Equation \(C.26\)](#) and [Equation \(C.25\)](#) gives

$$\begin{aligned}\frac{v_1 \sin \theta}{v_1 \cos \theta} &= \frac{v'_1 \sin \theta'}{v'_1 \cos \theta' + V} \\ \tan \theta &= \frac{\sin \theta'}{\cos \theta' + \frac{V}{v'_1}} \\ \tan \theta &= \frac{\sin \theta'}{\frac{V}{v'_1} + \cos \theta'}\end{aligned}\tag{C.27}$$

We need to reformulate the velocity ratio. Substitution from [Equation \(C.20\)](#) gives

$$\frac{V}{v'_1} = \frac{V}{u'_1}\tag{C.28}$$

Using Galilean transformation and [Equation \(C.23\)](#) we have that

$$\begin{aligned}\mathbf{u}'_1 &= \mathbf{u}_1 - \mathbf{V} \\ u'_1 &= u_1 - V \\ u'_1 &= u - \frac{\alpha}{1+\alpha}u \\ u'_1 &= u \left(1 - \frac{\alpha}{1+\alpha}\right) \\ u'_1 &= u \left(\frac{1+\alpha-\alpha}{1+\alpha}\right) \\ u'_1 &= \frac{1}{1+\alpha}u\end{aligned}\tag{C.29}$$

Substituting [Equation \(C.23\)](#) and [Equation \(C.29\)](#) into [Equation \(C.28\)](#) gives

$$\frac{V}{u'_1} = \frac{\frac{\alpha}{1+\alpha}u}{\frac{1}{1+\alpha}u} = \alpha\tag{C.30}$$

Substituting [Equation \(C.30\)](#) into [Equation \(C.27\)](#) gives

$$\begin{aligned}\tan \theta &= \frac{\sin \theta'}{\alpha + \cos \theta'} \\ \theta &= \arctan \left( \frac{\sin \theta'}{\alpha + \cos \theta'} \right)\end{aligned}\tag{C.31}$$

Substituting back the variable names from [Figure 2.1b](#) into [Equation \(C.31\)](#) gives

$$\theta_b = \arctan \left( \frac{\sin \theta'_b}{\alpha + \cos \theta'_b} \right) \quad (\text{C.32})$$

Using Galilean transformations, the connection between  $\mathbf{v}'_2$  and  $\mathbf{v}_2$  is expressed as

$$\begin{aligned} \mathbf{v}'_2 &= \mathbf{v}_2 - \mathbf{V} \\ \mathbf{v}_2 &= \mathbf{v}'_2 + \mathbf{V} \end{aligned} \quad (\text{C.33})$$

which in x-direction gives

$$\begin{aligned} v_2 \cos \varphi &= -v'_2 \cos \theta' + V \\ v_2 \cos \varphi &= V - v'_2 \cos \theta' \end{aligned} \quad (\text{C.34})$$

and in y-direction gives

$$v_2 \sin \varphi = v'_2 \sin \theta' \quad (\text{C.35})$$

The ratio of [Equation \(C.35\)](#) and [Equation \(C.34\)](#) gives

$$\begin{aligned} \frac{v_2 \sin \varphi}{v_2 \cos \varphi} &= \frac{v'_2 \sin \theta'}{V - v'_2 \cos \theta'} \\ \tan \varphi &= \frac{\sin \theta'}{\frac{V}{v'_2} - \cos \theta'} \end{aligned} \quad (\text{C.36})$$

We need to reformulate the velocity ratio. Substitution from [Equation \(C.18\)](#) and [Equation \(C.20\)](#) gives

$$\frac{V}{v'_2} = \frac{V}{\alpha v'_1} = \frac{V}{\alpha u'_1} \quad (\text{C.37})$$

Substituting [Equation \(C.30\)](#) into [Equation \(C.37\)](#) gives

$$\frac{V}{v'_2} = \frac{V}{\alpha \frac{V}{\alpha}} = 1 \quad (\text{C.38})$$

Substituting [Equation \(C.38\)](#) into [Equation \(C.36\)](#) gives

$$\begin{aligned}\tan \varphi &= \frac{\sin \theta'}{1 - \cos \theta'} = \frac{1}{\frac{1-\cos \theta'}{\sin \theta'}} = \frac{1}{\tan \frac{\theta'}{2}} = \cot \frac{\theta'}{2} \\ \varphi &= \frac{1}{2}(\pi - \theta') \text{ [radians]} = \frac{1}{2}(180^\circ - \theta') \text{ [degrees]}\end{aligned}\quad (\text{C.39})$$

Substituting back the variable names from [Figure 2.1](#) into [Equation \(C.39\)](#) gives

$$\theta_t = \frac{1}{2}(\pi - \theta'_b) \text{ [radians]} = \frac{1}{2}(180^\circ - \theta'_b) \text{ [degrees]} \quad (\text{C.40})$$



# Appendix D

## Computer setup and environment

Some calibration code is based on the codes of Ville Virtanen and Dr. Liam Gaffney. Other code/scripts have been written by the author in C++ / Python.

### D.1 The computer

The *MiniballCoulexSort* code does not require any a lot of computing power to run. [Table D.1](#) shows the computer with specifications used for the sorting and data analysis. Since the data from the experiment takes up about 60 GB, the limitation was with the SSD<sup>1</sup>. When running the sorting and event-building programs, the space on the computer rapidly vanishes.

**Table D.1:** Computer used for sorting and data analysis.

Model	MacBook Air (13-inch, 2017)
OS	macOS High Sierra (Version 10.13.6)
Processor	1.8 GHz (Intel Core i5, dual core, 4 threads) Max turbo frequency: 2.90 Ghz
Memory	8 GB (1600 MHz DDR3)
SSD	128 GB

---

<sup>1</sup>The SSD (solid-state drive) is the internal storage device in the computer.

## D.2 The environment

**Nevn den relative mappestrukturen, slik at terminal-commandoer gir mening. Både for Miniball kode og ROOT framework.**

The relative path of *MiniballCoulexSort* is

```
~/GitHub/Miniball/MiniballCoulexSort
```

The relative path of *kinsim3* is

```
~/GitHub/Miniball/kinsim
```

The relative path of the ROOT framework is

```
~/GitHub(ROOT-framework/build
```

### D.2.1 Relative path of programs and scripts

Table D.2 shows the relative path of programs, scripts and files used in this thesis. The settingsfile *MBSettings2017\_CLX\_IS558.dat*, and calibration files *IS558-online.cal* and *IS558-user.cal*, used in this experiment can be found in the directory specified in the table, but when used directly with *MiniballCoulexSort* the default path is *~/GitHub/Miniball/MiniballCoulexSort/config*. The file *setup\_Sm.txt* is in the table twice, this is because it is two files with the same name, one for plotting and one for fitting.

## D.3 Run time

**TODO: Run timing on M2R.sh**

## D.4 Script usage?

`ParticleFit.cpp`

Function

```
void AQ4_fit(std::string setup_file,
             std::string detector_side, int ring_gate = 1,
             bool help_lines = false)
```

**Table D.2:** Relative path of programs, scripts and files.

Relative path	Programs / scripts / files
~/GitHub/Miniball/kinsim	<code>kinsim3.cc</code>
~/GitHub/Miniball/MiniballCoulexSort/MedToRoot	<code>MedToRoot</code>
~/GitHub/Miniball/MiniballCoulexSort/TreeBuilder	<code>TreeBuilder</code> <code>AQ4Sort</code>
~/GitHub/Miniball/MiniballCoulexSort/CLXAna	<code>CLXAna</code>
~/GitHub/MasterThesis/Miniball-config	<code>MBSettings2017_CLX_IS558.dat</code> <code>IS558-online.cal</code> <code>IS558-user.cal</code> <code>config-IS558.dat</code>
~/GitHub/MasterThesis/SRIM	SRIM files
~/GitHub/MasterThesis/Scripts/sorting	<code>M2R.sh</code> <code>Q4S.sh</code> <code>Coulex.sh</code> <code>ParticlePlot.cpp</code> <code>GammaPlot.cpp</code> <code>setup_Sm.txt</code>
~/GitHub/MasterThesis/Scripts/plotting	<code>particle-calibration.py</code> <code>ParticleFit.cpp</code> <code>GammaFit.cpp</code> <code>setup_Sm.txt</code>
~/GitHub/MasterThesis/Scripts/calibration	
~/GitHub/MasterThesis/Scripts/fitting	
~/GitHub/MasterThesis/Scripts/generators	<code>ADC_generator.py</code> <code>DGF_generator.py</code> <code>Geometry_generator.py</code>
~/GitHub(ROOT-framework/build	<code>ROOT</code>
~/GitHub(ROOT-framework/build/bin	<code>hadd</code>

## D.5 Connecting MiniballCoulexSort with ROOT

To connect MiniballCoulexSort with ROOT you need them to share their libraries with each other. This is done with a dynamic loader, which you can find out more about here [58].

You have to make a `.rootrc` file in your home folder on your computer. In the `.rootrc` file you want to write something like this

```
Unix .*. Root .DynamicPath:    .:/Users/trondwj/GitHub/ROOT-
framework/build/lib >:/Users/trondwj/GitHub/Miniball/
MiniballCoulexSort/lib :
```

This should all be in one line. The first part is to tell the system to use the dynamic loader of ROOT to connect the given paths that follow. In my case the

**Table D.3:** Run time for building event trees. The run time of the bash scripts was timed with the built in command line script named `time`. It depends on the number of files added for tree building.

Executable	Run time [min]
TreeBuilder	~ 45
AQ4Sort	~ 130

lib folder of the ROOT install was at

```
/Users/trondwj/GitHub(ROOT-framework/build/lib
```

and the lib folder of the *MiniballCoulexSort* was at

```
/Users/trondwj/GitHub/Miniball/MiniballCoulexSort/lib
```

These paths are totally individual, and you will probably not have it in the same place. Therefore these paths must be changed to fit your system.

After making the file you either have restart the terminal or you can source the file by writing this in the terminal

```
$ source ~/.rootrc
```

## D.6 Running ROOT and MiniballCoulexSort from anywhere in the terminal

To run ROOT or the different scripts of *MiniballCoulexSort* anywhere in the terminal, you have to edit your `.bash_profile` file [`.bash_profile` on MacOS, `.bashrc` on Linux]. In the `.bash_profile` the following commands were used

```
# Run ROOT from anywhere
export ROOTSYS=$HOME/GitHub/ROOT-framework/build
export PATH=$ROOTSYS/lib:$PATH
export PATH=$ROOTSYS/bin:$PATH
export DYLD_LIBRARY_PATH=$ROOTSYS/lib:$DYLD_LIBRARY_PATH

# Run MiniballCoulexSort from anywhere
export DYLD_LIBRARY_PATH=$HOME/GitHub/Miniball/
MiniballCoulexSort/lib:$DYLD_LIBRARY_PATH
export PATH=$HOME/GitHub/Miniball/MiniballCoulexSort/lib:$PATH
export PATH=$HOME/GitHub/Miniball/MiniballCoulexSort/bin:$PATH
```

The DYLD\_LIBRARY\_PATH is used on Mac only. On other systems, use LD\_LIBRARY\_PATH instead. You need to locate the *lib* and *bin* folders for both ROOT and *MiniballCoulxSort* and change them to fit your system, and in addition you need the build folder of your ROOT install.



# Appendix E

## CD simulation

On the next page, the CD simulation is showed for each ring. Ring 1 is the innermost ring and ring 16 is the outermost ring. The plots show simulated counts vs. energy, where the first peak (lower energy) is the  $^{208}\text{Pb}$  and the second peak (higher energy) is  $^{140}\text{Sm}$ . The plots were grabbed from the `.root`-file by the commands

```
$ cd ~/GitHub/MasterThesis/Scripts/plotting
$ root
root [0] .L ParticlePlot.cpp++
root [1] simulation_plot("setup_Sm.txt", 0)
... <showing output from script>
```

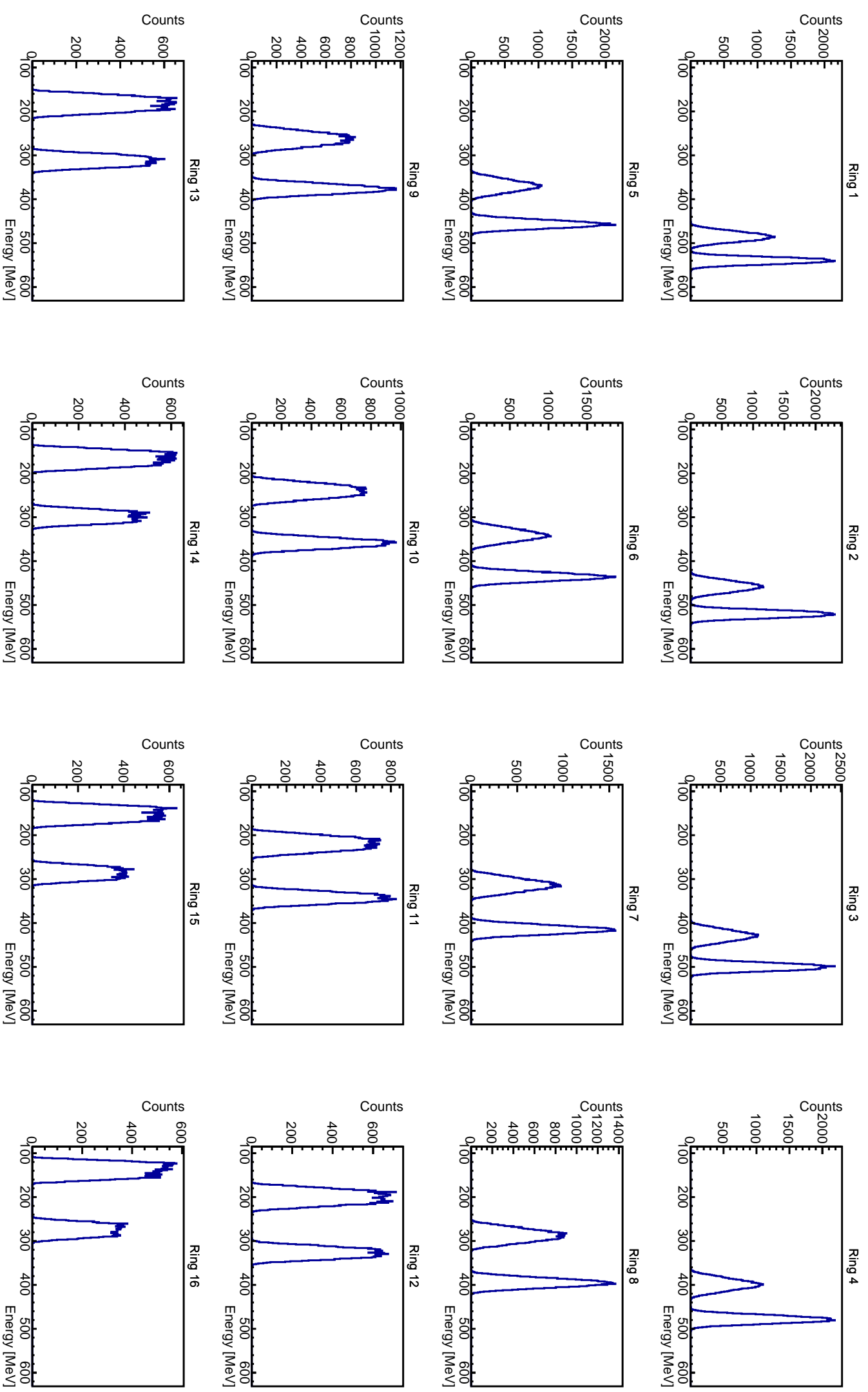
The next page after that shows the fitting of the CD simulation, where the red dotted curves shows the fitting of the peaks and the vertical black dotted lines shows the centroids of the peaks.

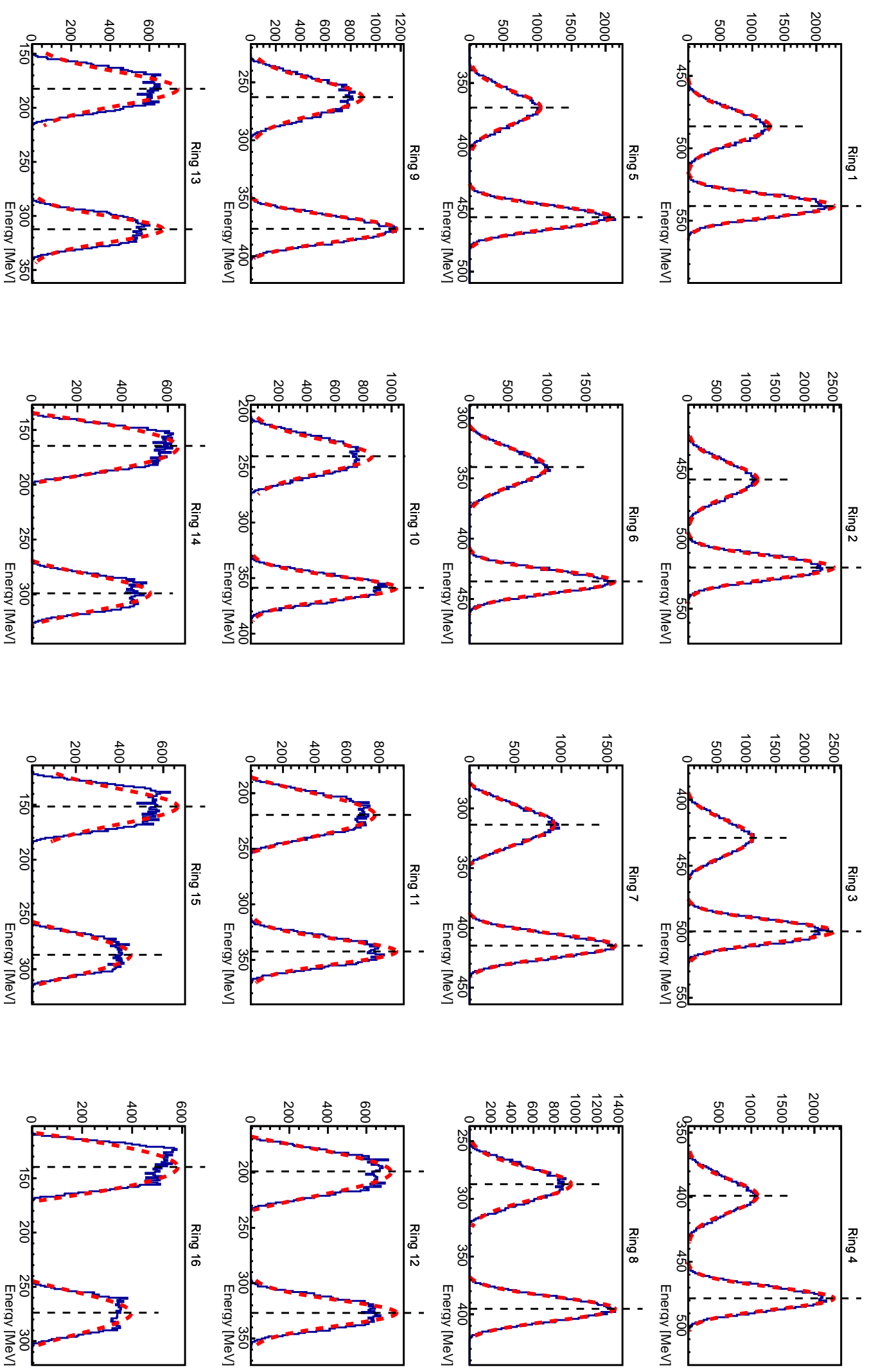
```
$ cd ~/GitHub/MasterThesis/Scripts/fitting
$ root
root [0] .L ParticleFit.cpp++
root [1] simulation_fit("setup_Sm.txt")
... <showing output from script>
```

For the Si dead layer in `kinsim3`, the SRIM files must have units of MeV/mm. If units of MeV/cm<sup>2</sup> are used, the distance on line 359 in `kinsim3` needs to be changed to the correct units. The correction factor is at the bottom of the SRIM file. Line 358 and 359 in `kinsim3` reads

```
// Correct for dead layer loss
dist = TMath::Abs( 0.0007 / TMath::Cos( TTh ) );
```

where the factor needs to be changed.







# Bibliography

- [1] M. Klintefjord. *Evolution of deformation and collectivity away from magic numbers*. PhD thesis, University of Oslo, May 2016. URL <http://urn.nb.no/URN:NBN:no-56121>.
- [2] M. Klintefjord, K. Hadyńska-Klęk, J. Samorajczyk, et al. Spectroscopy of low-lying states in  $^{140}\text{Sm}$ . *Acta Physica Polonica B*, 46(3):607–611, 2015. ISSN 0587-4254. doi: 10.5506/APhysPolB.46.607.
- [3] J. Samorajczyk, M. Klintefjord, C. Droste, et al. Revised spin values of the 991 keV and 1599 keV levels in Sm 140. *Physical Review C - Nuclear Physics*, 92(4):3–6, 2015. ISSN 1089490X. doi: 10.1103/PhysRevC.92.044322.
- [4] M. Klintefjord, K. Hadyńska-Klęk, A. Görgen, et al. Structure of low-lying states in Sm 140 studied by Coulomb excitation. *Physical Review C*, 93(5): 1–14, 2016. ISSN 24699993. doi: 10.1103/PhysRevC.93.054303.
- [5] K. S. Krane. *Introductory Nuclear Physics*. Wiley, 1987. ISBN 9780471805533. URL <https://www.wiley.com/en-us/Introductory+Nuclear+Physics%2C+3rd+Edition-p-9780471805533>.
- [6] D. J. Griffiths. *Introduction to Quantum Mechanics*. Pearson Prentice Hall, 2nd edition, 2005. ISBN 0-13-191175-9.
- [7] NIST Physics Laboratory web site. URL <https://physics.nist.gov/constants>. Accessed: July 2019.
- [8] O. B. Tarasov and D. Bazin. Lise++: Radioactive beam production with in-flight separators. *Nuclear Instruments and Methods in Physics Research Section B: Beam Interactions with Materials and Atoms*, 266(19):4657 – 4664, 2008. ISSN 0168-583X. doi: <https://doi.org/10.1016/j.nimb.2008.05.110>. URL <http://lise.nscl.msu.edu/lise.html>. Proceedings of the XVth International Conference on Electromagnetic Isotope Separators and Techniques Related to their Applications.
- [9] P. Reiter, J. Eberth, H. Faust, et al. The MINIBALL array. *Nuclear Physics A*, 701(1-4):209–212, 2002. ISSN 03759474. doi: 10.1016/S0375-9474(01)01576-7.

- [10] M. J. Borge and K. Riisager. HIE-ISOLDE, the project and the physics opportunities. *European Physical Journal A*, 52(11), 2016. ISSN 1434601X. doi: 10.1140/epja/i2016-16334-4.
- [11] The ISOLDE web page. URL <http://isolde.web.cern.ch>. Accessed: July 2019.
- [12] B. Jonson and K. Riisager. The ISOLDE facility. *Scholarpedia*, 5(7):9742, 2010. doi: 10.4249/scholarpedia.9742. Revision #90796.
- [13] Nucleonica Newsletter, 2019. URL <https://www.nucleonica.com/wiki/images/c/cb/NucleonicaNewsletter2019.pdf>. Accessed: July 2019.
- [14] M. Lindroos. Review of the ISOL Method. Technical Report CERN-AB-2004-086, CERN, Geneva, Aug 2004. URL <https://cds.cern.ch/record/793447>. Revised version submitted on 2004-09-28 17:19:32.
- [15] D. Olsen. First generation ISOL radioactive ion beam facilities. pages 312–316, 2002. doi: 10.1109/pac.1995.504646.
- [16] N. Warr, J. Van de Walle, M. Albers, et al. The miniball spectrometer. *European Physical Journal A*, 49(3):1–32, 2013. ISSN 1434601X. doi: 10.1140/epja/i2013-13040-9.
- [17] C. Lefèvre. The CERN accelerator complex. Complexe des accélérateurs du CERN. Dec 2008. URL <https://cds.cern.ch/record/1260465>.
- [18] R. Catherall, W. Andreadza, M. Breitenfeldt, et al. The ISOLDE facility. 2, 2017. ISSN 13616471. doi: 10.1088/1361-6471/aa7eba.
- [19] M. J. Borge. The ISOLDE facility: Recent highlights and the HIE-ISOLDE project. *Proceedings of Science*, 11005:1–8, 2013. ISSN 18248039.
- [20] The ISOLDE RILIS web page. URL <http://rilis.web.cern.ch>. Accessed: July 2019.
- [21] B. A. Marsh, B. Andel, A. N. Andreyev, et al. New developments of the in-source spectroscopy method at RILIS/ISOLDE. *Nuclear Instruments and Methods in Physics Research, Section B: Beam Interactions with Materials and Atoms*, 317(PART B):550–556, 2013. ISSN 0168583X. doi: 10.1016/j.nimb.2013.07.070. URL <http://dx.doi.org/10.1016/j.nimb.2013.07.070>.
- [22] T. D. Goodacre, V. Fedossev, S. Rothe, et al. Ion beam production and study of radioactive isotopes with the laser ion source at ISOLDE. *Journal of Physics G: Nuclear and Particle Physics*, 44(8):084006, 2017. ISSN 0954-3899. doi: 10.1088/1361-6471/aa78e0.

- [23] E. Kugler, D. Fiander, B. Johnson, et al. The new CERN-ISOLDE on-line mass-separator facility at the PS-Booster. *Nuclear Inst. and Methods in Physics Research, B*, 70(1-4):41–49, 1992. ISSN 0168583X. doi: 10.1016/0168-583X(92)95907-9.
- [24] P. Schmidt, F. Ames, G. Bollen, et al. Bunching and cooling of radioactive ions with REXTRAP. *Nuclear Physics A*, 701(1-4):550–556, 2002. ISSN 03759474. doi: 10.1016/S0375-9474(01)01642-6.
- [25] F. Ames, G. Bollen, P. Delahaye, et al. Cooling of radioactive ions with the Penning trap REXTRAP. *Nuclear Instruments and Methods in Physics Research, Section A: Accelerators, Spectrometers, Detectors and Associated Equipment*, 538(1-3):17–32, 2005. ISSN 01689002. doi: 10.1016/j.nima.2004.08.119.
- [26] B. H. Wolf, J. Cederkäll, O. Forstner, et al. First radioactive ions charge bred in REXEBIS at the REX-ISOLDE accelerator. *Nuclear Instruments and Methods in Physics Research, Section B: Beam Interactions with Materials and Atoms*, 204:428–432, 2003. ISSN 0168583X. doi: 10.1016/S0168-583X(02)02108-0.
- [27] Y. Kadi, Y. Blumenfeld, W. V. Delsolaro, et al. Post-accelerated beams at ISOLDE. *Journal of Physics G: Nuclear and Particle Physics*, 44(8), 2017. ISSN 13616471. doi: 10.1088/1361-6471/aa78ca.
- [28] The REX-ISOLDE web page. URL <http://rex-isolde.web.cern.ch>. Accessed: July 2019.
- [29] The HIE-ISOLDE web page. URL <http://hie-isolde-project.web.cern.ch>. Accessed: July 2019.
- [30] F. Wenander. EBIS as charge breeder for radioactive ion beam accelerators. *Nuclear Physics A*, 701(1-4):528–536, 2002. ISSN 03759474. doi: 10.1016/S0375-9474(01)01640-2.
- [31] F. Wenander. Charge breeding of radioactive ions with EBIS and EBIT. *Journal of Instrumentation*, 5(10), 2010. ISSN 17480221. doi: 10.1088/1748-0221/5/10/C10004.
- [32] F. L. Bello Garrote, A. Görgen, J. Mierzejewski, et al. Lifetime measurement for the 21+ state in Sm 140 and the onset of collectivity in neutron-deficient Sm isotopes. *Physical Review C - Nuclear Physics*, 92(2):1–8, 2015. ISSN 1089490X. doi: 10.1103/PhysRevC.92.024317.

- [33] N. Warr. *The Miniball double-sided silicon strip detector (CD)*, October 2015. URL <https://www.ikp.uni-koeln.de/~warr/doc/cd.pdf>. Accessed: April 2019.
- [34] A. N. Ostrowski, S. Cherubini, T. Davinson, et al. CD: A double sided silicon strip detector for radioactive nuclear beam experiments. *Nuclear Instruments and Methods in Physics Research, Section A: Accelerators, Spectrometers, Detectors and Associated Equipment*, 480(2-3):448–455, 2002. ISSN 01689002. doi: 10.1016/S0168-9002(01)00954-8.
- [35] N. Warr. *The Miniball Cluster*, March 2005. URL [https://www.ikp.uni-koeln.de/~warr/doc/miniball\\_detectors.pdf](https://www.ikp.uni-koeln.de/~warr/doc/miniball_detectors.pdf). Accessed: July 2019.
- [36] P. A. Butler, J. Cederkall, and P. Reiter. Nuclear-structure studies of exotic nuclei with MINIBALL. *Journal of Physics G: Nuclear and Particle Physics*, 44(4), 2017. ISSN 1361-6471. doi: 10.1088/1361-6471/aa5c4e.
- [37] D. P. Rosiak. *Coulomb excitation of doubly-magic  $^{132}\text{Sn}$  at HIE-ISOLDE and development of escape-suppression shields for the MINIBALL spectrometer*. PhD thesis, University of Cologne, 2018. URL <https://kups.ub.uni-koeln.de/8469/>.
- [38] R. Lutter, O. Schaile, K. Schöffel, et al. MARaBOOU-A MBS and ROOT based online/offline utility. *SANTA FE 1999 - 11th IEEE NPSS Real Time Conference, Conference Record, RT 1999*, (May):363–366, 1999. doi: 10.1109/RTCON.1999.842643.
- [39] H. G. Essel and N. Kurz. The general purpose data acquisition system MBS. *SANTA FE 1999 - 11th IEEE NPSS Real Time Conference, Conference Record, RT 1999*, 41(2):475–478, 1999. doi: 10.1109/RTCON.1999.842672.
- [40] R. Brun and F. Rademakers. ROOT - An Object Oriented Data Analysis Framework. Proceedings AIHENP'96 Workshop, Lausanne, Sep. 1996, Nucl. Inst. & Meth. in Phys. Res. A 389 (1997) 81-86, . URL <https://github.com/root-project/root>. doi: 10.5281/zenodo.2557526. Download: December 2018.
- [41] N. Warr. *Miniball electronics for 2015*, October 2015. URL [https://www.ikp.uni-koeln.de/~warr/doc/electronics\\_201507.pdf](https://www.ikp.uni-koeln.de/~warr/doc/electronics_201507.pdf). Accessed: August 2019.
- [42] HIE-ISOLDE: Technical Design Report for the Energy Upgrade, edited by Y. Kadi, M. A. Fraser and A. Papageorgiou-Koufidou, CERN Yellow Reports: Monographs, Vol. 1/2018, CERN-2018-002-M (CERN, Geneva, 2018). <https://doi.org/10.23731/CYRM-2018-001>.

- [43] Analysis code for MINIBALL experiments at ISOLDE. URL <https://github.com/Miniball/MiniballCoulexSort>. doi: 10.5281/zenodo.2593370. Download: March 2019.
- [44] W. R. Leo. *Techniques for Nuclear and Particle Physics Experiments*. Springer, Berlin, Heidelberg, second revised edition, 1994. doi: 10.1007/978-3-642-57920-2.
- [45] L. Gaffney. Kinematics simulations for Coulomb-excitation experiments at Miniball. URL <https://github.com/lpgaff/kinsim>. Download: May 2018.
- [46] J. F. Ziegler, J. P. Biersack, and M. D. Ziegler. SRIM - The Stopping and Range of Ions in Matter, 2013. URL <http://www.srim.org>. Download: February 2018.
- [47] B. Bruyneel, P. Reiter, and G. Pascovici. Characterization of large volume HPGe detectors. Part I: Electron and hole mobility parameterization. *Nuclear Instruments and Methods in Physics Research, Section A: Accelerators, Spectrometers, Detectors and Associated Equipment*, 569(3):764–773, 2006. ISSN 01689002. doi: 10.1016/j.nima.2006.08.130.
- [48] B. Bruyneel, P. Reiter, and G. Pascovici. Characterization of large volume HPGe detectors. Part II: Experimental results. *Nuclear Instruments and Methods in Physics Research, Section A: Accelerators, Spectrometers, Detectors and Associated Equipment*, 569(3):774–789, 2006. ISSN 01689002. doi: 10.1016/j.nima.2006.08.129.
- [49] B. Bruyneel. *Characterization of Segmented Large Volume, High Purity Germanium Detectors*. PhD thesis, University of Cologne, 2006. URL <https://kups.ub.uni-koeln.de/1858/>.
- [50] M. Descovich, I. Y. Lee, P. N. Luke, et al. Effects of neutron damage on the performance of large volume segmented germanium detectors. *Nuclear Instruments and Methods in Physics Research, Section A: Accelerators, Spectrometers, Detectors and Associated Equipment*, 545(1-2):199–209, 2005. ISSN 01689002. doi: 10.1016/j.nima.2005.01.308.
- [51] I. Abt, L. Garbini, C. Gooch, et al. Alpha-event and surface characterisation in segmented true-coaxial HPGe detectors. *Nuclear Instruments and Methods in Physics Research, Section A: Accelerators, Spectrometers, Detectors and Associated Equipment*, 858(June 2017):80–89, 2017. ISSN 01689002. doi: 10.1016/j.nima.2017.03.057. URL <http://dx.doi.org/10.1016/j.nima.2017.03.057>.

- [52] G. L. Miller, W. M. Gibson, and P. F. Donovan. Semiconductor Particle Detectors. *Annual Review of Nuclear Science*, 12(1):189–220, 1962. ISSN 0066-4243. doi: 10.1146/annurev.ns.12.120162.001201.
- [53] B. Wilkins, M. Fluss, S. Kaufman, C. Gross, and E. Steinberg. Pulse-height defects for heavy ions in a silicon surface-barrier detector. *Nuclear Instruments and Methods*, 92:381–391, 1971. doi: [https://doi.org/10.1016/0029-554X\(71\)90414-9](https://doi.org/10.1016/0029-554X(71)90414-9).
- [54] L. Grassi, J. Forneris, D. Torresi, et al. Study of the inter-strip gap effects on the response of Double Sided Silicon Strip Detectors using proton micro-beams. *Nuclear Instruments and Methods in Physics Research, Section A: Accelerators, Spectrometers, Detectors and Associated Equipment*, 767:99–111, 2014. ISSN 01689002. doi: 10.1016/j.nima.2014.08.009.
- [55] G. Kramberger, V. Cindro, I. Mandi, M. Mikuž, and M. Zavrtanik. Effective trapping time of electrons and holes in different silicon materials irradiated with neutrons, protons and pions. *Nuclear Instruments and Methods in Physics Research, Section A: Accelerators, Spectrometers, Detectors and Associated Equipment*, 481(1-3):297–305, 2002. ISSN 01689002. doi: 10.1016/S0168-9002(01)01263-3.
- [56] N. Warr. *Miniball Flexible Frame*, March 2015. URL <https://www.ikp.uni-koeln.de/~warr/doc/frame.pdf>. Accessed: July 2019.
- [57] P. Doornenbal. In-beam gamma-ray spectroscopy at the RIBF. *Progress of Theoretical and Experimental Physics*, 2012(1):1–18, 2012. ISSN 20503911. doi: 10.1093/ptep/pts076.
- [58] R. Brun and F. Rademakers. ROOT - User's Guide, . URL <https://root.cern.ch/root/html/doc/guides/users-guide/ROOTUsersGuide.html#file-system.rootrc>. Accessed: August 2019.